

NPS-OC-97-005

NAVAL POSTGRADUATE SCHOOL MONTEREY, CALIFORNIA



THESIS

**MODELING STUDIES OF WIND AND
THERMOHALINE FORCING ON THE
CALIFORNIA CURRENT SYSTEM**

by

Philip W. Vance

June 1997

Thesis Advisor:

Mary L. Batteen

Approved for public release; distribution is unlimited.

Prepared for:
National Science Foundation
4201 Wilson Boulevard
Arlington, VA 22230

DTIC QUALITY INSPECTED 4

19980102 114

**NAVAL POSTGRADUATE SCHOOL
MONTEREY, CALIFORNIA 93943**

Rear Admiral Marsha J. Evans
Superintendent

This thesis was prepared in conjunction with research sponsored in part by the National Science Foundation, 4201 Wilson Boulevard, Arlington, VA 22230.

Reproduction of all or part of this report is authorized.

Released by:

A handwritten signature in black ink, appearing to read "David W. Netzer". The signature is fluid and cursive, with a long horizontal stroke extending to the right.

David W. Netzer, Associate Provost and Dean of Research

REPORT DOCUMENTATION PAGE

Form Approved OMB No. 0704-0188

Public reporting burden for this collection of information is estimated to average 1 hour per response, including the time for reviewing instruction, searching existing data sources, gathering and maintaining the data needed, and completing and reviewing the collection of information. Send comments regarding this burden estimate or any other aspect of this collection of information, including suggestions for reducing this burden, to Washington Headquarters Services, Directorate for Information Operations and Reports, 1215 Jefferson Davis Highway, Suite 1204, Arlington, VA 22202-4302, and to the Office of Management and Budget, Paperwork Reduction Project (0704-0188) Washington DC 20503.

1. AGENCY USE ONLY (Leave blank)	2. REPORT DATE June 1997	3. REPORT TYPE AND DATES COVERED Master's Thesis	
4. TITLE AND SUBTITLE MODELING STUDIES OF WIND AND THERMOHALINE FORCING ON THE CALIFORNIA CURRENT SYSTEM		5. FUNDING NUMBERS	
6. AUTHOR(S) Philip W. Vance, in conjunction with Mary L. Batteen			
7. PERFORMING ORGANIZATION NAME(S) AND ADDRESS(ES) Naval Postgraduate School Monterey, CA 93943-5000		8. PERFORMING ORGANIZATION REPORT NUMBER NPS-OC-97-005	
9. SPONSORING/MONITORING AGENCY NAME(S) AND ADDRESS(ES) National Science Foundation 4201 Wilson Boulevard Arlington, VA. 22230		10. SPONSORING/MONITORING AGENCY REPORT NUMBER	
11. SUPPLEMENTARY NOTES The views expressed in this thesis are those of the author and do not reflect the official policy or position of the Department of Defense or the U.S. Government.			
12a. DISTRIBUTION/AVAILABILITY STATEMENT Approved for public release; distribution is unlimited.		12b. DISTRIBUTION CODE	
13. ABSTRACT (maximum 200 words) A high-resolution, multi-level, primitive equation model is initialized with climatological data to study the combined effects of wind and thermohaline forcing on the ocean circulation of the California Current System (CCS). The ocean circulation is generated by the model using a combination of climatological wind stress and thermohaline forcing. In the first experiment, the effects of thermohaline forcing alone are evaluated, in the second experiment, previously conducted, the effects of wind forcing are isolated, while in the third experiment, the combined effects of wind and thermohaline forcing are looked at. The results from the combined experiment show that even though the effects of wind forcing dominate the CCS, the additional effects of the thermohaline forcing results in the following: the seasonal development of a poleward surface current and an equatorward undercurrent in the poleward end of the model region; an onshore geostrophic component, which results in a temperature front and stronger surface and subsurface currents between Cape Mendocino and Point Arena; and a region of maximum eddy kinetic energy inshore of ~125°W between Cape Mendocino and Point Arena, associated with the temperature front. These model simulations are qualitatively similar to recent hydrographic, altimetric, drifter, and moored observations of the CCS.			
SUBJECT TERMS Primitive equation model, California Current System, salinity, density, eddies, currents		15. NUMBER OF PAGES 89	
		16. PRICE CODE	
17. SECURITY CLASSIFICATION OF REPORT Unclassified	18. SECURITY CLASSIFICATION OF THIS PAGE Unclassified	19. SECURITY CLASSIFICATION OF ABSTRACT Unclassified	20. LIMITATION OF ABSTRACT UL

NSN 7540-01-280-5500

Standard Form 298 (Rev. 2-89)
Prescribed by ANSI Std. Z39-18 298-102

Approved for public release; distribution is unlimited.

**MODELING STUDIES OF WIND AND THERMOHALINE FORCING ON THE
CALIFORNIA CURRENT SYSTEM**

Philip W. Vance
Lieutenant Commander, United States Navy
B.S., United States Naval Academy – 1986

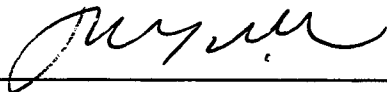
Submitted in partial fulfillment
of the requirements for the degree of

MASTER OF SCIENCE IN PHYSICAL OCEANOGRAPHY

from the

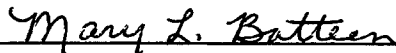
**NAVAL POSTGRADUATE SCHOOL
June 1997**

Author:



Philip W. Vance

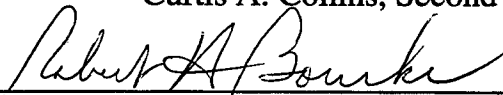
Approved by:



Mary L. Batteen, Thesis Advisor



Curtis A. Collins, Second Reader



Robert H. Bourke, Chairman
Department of Oceanography

ABSTRACT

A high-resolution, multi-level, primitive equation model is initialized with climatological data to study the combined effects of wind and thermohaline forcing on the ocean circulation of the California Current System (CCS). The ocean circulation is generated by the model using a combination of climatological wind stress and thermohaline forcing. In the first experiment, the effects of thermohaline forcing alone are evaluated, in the second experiment, previously conducted, the effects of wind forcing are isolated, while in the third experiment, the combined effects of wind and thermohaline forcing are looked at. The results from the combined experiment show that even though the effects of wind forcing dominate the CCS, the additional effects of the thermohaline forcing results in the following: the seasonal development of a poleward surface current and an equatorward undercurrent in the poleward end of the model region; an onshore geostrophic component, which results in a temperature front and stronger surface and subsurface currents between Cape Mendocino and Point Arena; and a region of maximum eddy kinetic energy inshore of $\sim 125^{\circ}\text{W}$ between Cape Mendocino and Point Arena, associated with the temperature front. These model simulations are qualitatively similar to recent hydrographic, altimetric, drifter, and moored observations of the CCS.

TABLE OF CONTENTS

I. INTRODUCTION.....	1
II. MODEL DESCRIPTION	3
A. MODEL EQUATIONS.....	3
B. METHOD OF SOLUTION	5
C. FORCING CONDITIONS	7
D. EXPERIMENTAL DESIGN	8
III. RESULTS FROM MODEL SIMULATIONS.....	11
A. EXPERIMENT 1 - SEASONAL TEMPERATURE AND SALINITY FORCING.....	11
1. Spin-up Phase.....	11
2. Quasi-equilibrium Phase	12
B. EXPERIMENT 2 - SEASONAL WIND FORCING.....	13
1. Spin-up Phase.....	13
2. Quasi-equilibrium Phase	14
C. EXPERIMENT 3 - SEASONAL WIND AND THERMOHALINE FORCING.....	15
1. Spin-up Phase.....	15
2. Quasi-equilibrium Phase	16
LIST OF REFERENCES	69
INITIAL DISTRIBUTION LIST.....	73

LIST OF FIGURES

1. Generalized circulation schematic of the classical climatological California Current System (CCS). The broad, slow surface equatorward California Current (CC) overlies the poleward California Undercurrent (CUC) along with the Inshore Countercurrent (IC), known as the Davidson Current (DC) north of Point Conception and as the Southern California Eddy (SCE) south of Point Conception. 20
2. Domain and climatological winds of the model for the California Current System (CCS) off the Western United States. The domain is bounded by 35°N to 47.5°N, 120°W to 132.5°W. The climatological (1980-1989) ECMWF winds used in Experiments 2 and 3 in m/s are shown here for (a) January, (b) April, (c) July, and (d) October. Maximum wind vector is 20 m/s. 21
3. Time series plot of monthly temperature and salinity fields used as seasonal forcing in Experiments 1 and 3. The '*' symbol represents data at 35°N, 132.5°W, while the '+' plot represents data at 47.5°N, 132.5°W for levels: (a) 13 m, (b) 46 m, (c) 98 m, (d) 182 m, (e) 316 m, (f) 529 m, and (g) 870 m depth. 25
4. Density contours and velocity vectors at 46 m depth for Experiment 1 at days (a) 3, (b) 45, (c) 180, and (d) 255. In all the velocity fields presented, to avoid clutter, velocity vectors are plotted every third (fourth) grid point in the cross-shore (alongshore) direction. Contour interval is 0.2 gm/cm³; maximum velocity vector is 50 cm/s..... 32
5. Density contours and velocity vectors at 529 m depth for Experiment 1, day 63. Contour interval is 0.2 gm/cm³; maximum velocity vector is 10 cm/s..... 36
6. Cross-shore section of meridional velocity (v) at 46°N for Experiment 1 during the third year of model simulation, time-averaged for days (a) 1-363 and (b) 270-363. Contour interval is 1 cm/s..... 37
7. Density contour and velocity vectors at 46 m depth for Experiment 1, time-averaged for year 3. Contour interval is 0.2 gm/cm³; maximum velocity vector is 25 cm/s..... 39
8. Cross-shore section at 41.3°N of v in the coastal region for Experiment 2 at days (a) 180 and (b) 195. The contour interval is 2 cm/s (5 cm/s) for poleward (equatorward) flow. 40
9. Temperature contours and velocity vectors at 46 m depth for Experiment 2 at days (a) 225, (b) 255, (c) 270, and (d) 315. Here and in the following figures, CB refers to Cape Blanco, CM to Cape Mendocino, and PA to Point Arena. Contour interval is 1°C, maximum velocity vector is 100 cm/s..... 42
10. Temperature and velocity vectors at 46 m depth for Experiment 2 in the third year of model simulation, time-averaged over the months of (a) April, (b) July, (c) October, and (d) December. Contour interval is 1°C; maximum velocity vector is 100 cm/s.... 46

11. Time-averaged plots for the upwelling season for Experiment 2 of (a) temperature contours and velocity vectors at 46 m depth, (b) cross-section of v at 41.3°N, and (c) velocity vectors at 316 m depth. Contour interval is 1°C in Figure 11a and 5 cm/s in Figure 11b. Maximum velocity vector is 100 cm/s in Figure 11a and 80 cm/s in Figure 11c.....	50
12. Density contours and velocity vectors at 46 m depth for Experiment 3 at days (a) 45, (b) 87, (c) 180, and (d) 255. Contour interval is 0.2 gm/cm ³ ; maximum velocity vector is 50 cm/s.....	53
13. Cross-shore of v in the coastal region for Experiment 3, days (a) 180 at 39°N, and (b) 360 at 46°N. Contour interval is 5 cm/s for Figure 13a and 1 cm/s for velocities -5 to 0 cm/s in Figure 13b.	57
14. Temperature contours and velocity vectors at 46 m depth for Experiment 3 in the third year of model simulation for days 90-270. Contour interval is .5°C; maximum velocity vector is 50 cm/s.	59
15. Cross-shore sections for Experiment 3 in the third year of model simulation, time-averaged for days 90-270 at (a) 41°N, and (b) 40.2°N. Contour interval is 5 cm/s....	60
16. Horizontal maps at 13 m depth of (a) mean kinetic energy (MKE), and (b) eddy kinetic energy (EKE) for Experiment 3 in the third year of model simulation, time-averaged for days 90-270.....	62
17. Cross-shore sections for Experiment 3 in the third year of model simulation, time-averaged for days 270-363 at (a) 37°N, (b) 43°N, and (c) 46°N. Contour interval is 5 cm/s.....	64

LIST OF TABLES

1. Values of Constants Used in the Model	67
--	----

ACKNOWLEDGEMENT

The professional guidance, patience, and support provided by my advisor, Dr. Mary Batteen, was an essential and invaluable part of this thesis without whose expertise, this could not have been accomplished. There is also the technical expertise and computer service requirements provided by Mr. Pete Braccio, whose professionalism and on the spot availability helped me to overcome stumbling blocks while using FORTRAN, MATLAB, and FERRET.

Finally, the time needed to be dedicated on this project was fully supported by my wife and family. Without their support, time, patience and flexibility I would not have been able to finish this thesis.

Thank you to all!

I. INTRODUCTION

Three types of water masses are found in the California Current System (CCS): Pacific sub-Arctic, North Pacific Central, and Southern waters (Hickey, 1997). The Pacific sub-Arctic water, characterized by low salinity and temperature and high oxygen and nutrients, is advected equatorward in the CCS. North Pacific Central water, characterized by high salinity and temperature and low oxygen and nutrients, enters the CCS from the west. Southern water characterized by high salinity, temperature and nutrients, and low oxygen, enters the CCS from the south with the poleward undercurrent (Lynn and Simpson, 1987).

The climatological mean CCS is a classical eastern boundary current (EBC) system, which consists of several large-scale currents (see Figure 1). The predominant flow is the California Current (CC), which, in the mean, is a broad (~1000 km), relatively slow (~10-30 cm/s), equatorward surface flow. It flows year-round, and extends to ~500 m depth. The second basic flow is the California Undercurrent (CUC), which is a narrower (~10-40 km), relatively weak (~2-10 cm/s), poleward subsurface flow. It can vary seasonally and is strongest at ~300 m depth. The third flow component is the Inshore Countercurrent (IC), which is known as the Davidson Current (DC) north of Point Conception. This is also a relatively weak (~5 cm/s) poleward flow, found during the fall and winter at the surface and near the coast. There are other ICs known as the Southern California Countercurrent (SCC) to the south, and the Southern California Eddy (SCE) inshore of the Channel Islands within the California Bight (Hickey, 1979, 1997).

Recent observational studies have shown that the CCS is not the quiescent, stable system of currents with a well-defined, unchanging structure suggested by Figure 1. Rather, the flow fluctuates greatly in both time and space (Chelton, 1984). There exist mesoscale meanders, eddies, filaments and jet-like surface currents, which are superimposed on the large-scale flow (e.g. Bernstein *et al.*, 1977; Strub *et al.*, 1991). The combination of these features has led to a new conceptualization of the CCS as a system

of currents with filamented jets and mesoscale eddies modifying the mean flow (Mooers and Robinson, 1984).

Recent numerical modeling results from Batteen (1997) have shown that both wind forcing and coastline irregularities are important mechanisms for the generation of many of the observed features of the CCS. In particular, the alongshore component of the wind stress has been shown to be a key ingredient for generating realistic vertical and horizontal structures for the surface equatorward and subsurface poleward currents. With such structures the currents are baroclinically and barotropically unstable, resulting in the generation of meanders, filaments, and eddies. Irregularities in the coastline geometry have also been shown to be important for "anchoring" upwelling and filaments as well as enhancing the growth of meanders and eddy.

Recent dynamic height analyses by Batteen *et al.* (1995) have shown that the distribution of both temperature and salinity in the CCS can be important in defining the large-scale circulation. In particular, while temperature is, as expected, the major source of density variations, the mean variability of salinity has been shown to be responsible for a significant equatorward component along the coast of California and a strong offshore component adjacent to Baja. Based on this analysis, Batteen *et al.* (1995) concluded that, descriptively and dynamically, both temperature and salinity are essential to accurately characterize the large-scale structure of the CCS.

Here we ask the question what the combined wind and thermohaline variability effects are on the large-scale CCS circulation. To address this question three model experiments, one with climatological thermohaline forcing, one with climatological wind forcing, and one with both climatological wind and thermohaline forcing, are run and compared with each other. This study is organized as follows: The model and the experimental conditions used in the basic study are presented in section 2, while results of the three model experiments are described in section 3.

II. MODEL DESCRIPTION

A. MODEL EQUATIONS

The numerical model in this study was originally used for a coarse resolution, closed basin by Haney (1974), and later adapted for eddy-resolving, limited EBC regions with open borders on the northern, western, and southern boundaries by Batteen *et al.* (1989, 1996) and Batteen (1997). The limited area EBC model is multi-level, uses non-adiabatic primitive equations on a beta-plane, and has both baroclinic and barotropic velocity components. The model is based on the hydrostatic, Boussinesq, and rigid lid approximations. The governing equations are as follows:

$$\frac{du}{dt} = \frac{-1}{\rho_0} \frac{\partial p}{\partial x} + fv - A_M \nabla^4 u + K_M \frac{\partial^2 u}{\partial z^2} \quad (1)$$

$$\frac{dv}{dt} = \frac{-1}{\rho_0} \frac{\partial p}{\partial y} - fu - A_M \nabla^4 v + K_M \frac{\partial^2 v}{\partial z^2} \quad (2)$$

$$\frac{\partial u}{\partial x} + \frac{\partial v}{\partial y} + \frac{\partial w}{\partial z} = 0 \quad (3)$$

$$\frac{\partial p}{\partial z} = -\rho g \quad (4)$$

$$\rho = \rho_0 [1 - \alpha(T - T_0) + \beta(S - S_0)] \quad (5)$$

$$\frac{dT}{dt} = -A_H \nabla^4 T + K_H \frac{\partial^2 T}{\partial z^2} \quad (6)$$

$$\frac{dS}{dt} = -A_H \nabla^4 S + K_H \frac{\partial^2 S}{\partial z^2} \quad (7)$$

In the above equations, t is time, (x, y, z) is a right-handed Cartesian coordinate system with x pointing toward shore, y alongshore, and z upward. The corresponding velocity components are (u, v, w) , T is temperature, S is salinity, ρ is density, and p is pressure. Table 1 provides a list of other symbols found in the model equations, as well as values of constants used throughout the study.

For the finite differencing, a space-staggered B-scheme (Arakawa and Lamb, 1977) is used in the horizontal. Batteen and Han (1981) have shown that this scheme is appropriate when the grid spacing is approximately on the same order as, or less than, the Rossby radius of deformation, which meets the criteria of this study. The horizontal grid spacing is 11 km in the alongshore direction and 8 km in the cross-shore direction, while the internal Rossby radius of deformation is ~ 30 km. In the vertical, the 10 layers are separated by constant z-levels of 13, 46, 98, 182, 316, 529, 870, 1416, 2283, and 3656 m. This spacing scheme concentrates more on the upper, dynamically active part of the ocean, above the thermocline.

The model domain (Figure 2) is a rectangular region encompassing the west coast of the United States, from $\sim 35^\circ\text{N}$ to 47.5°N (1408 km alongshore), and from $\sim 120^\circ\text{W}$ to 132.5°W (1024 km cross-shore). The coastal boundaries of the model domain are closed, and have both the tangential and normal components of velocity set to zero. Bottom topography has been omitted to focus on the roles played by wind and thermohaline forcing. The constant depth used in the model is 4500 m. A modified version of the radiation boundary conditions of Camerlengo and O'Brien (1980) is used for the open ocean domain boundaries to the north, south, and west. Some spatial smoothing is applied in the vicinity of the open boundaries.

The model uses biharmonic lateral heat and momentum diffusion with the same choice of coefficients (i.e., $2.0 \times 10^{17} \text{cm}^4 \text{s}^{-1}$) as in Batteen *et al.* (1989). Holland (1978) showed that the highly scale-selective biharmonic diffusion acts predominantly on submesoscales, while Holland and Batteen (1986) found that baroclinic mesoscale processes can be damped by Laplacian lateral heat diffusion. As a result, the use of biharmonic lateral diffusion should allow mesoscale eddy generation via barotropic (horizontal shear) and/or baroclinic (vertical shear) instability mechanisms. As in Batteen *et al.* (1989), weak ($0.5 \text{cm}^2 \text{s}^{-1}$) vertical eddy viscosities and conductivity are used. Bottom stress is parameterized by a simplified quadratic drag law (Weatherly, 1972), as in Batteen *et al.* (1989).

B. METHOD OF SOLUTION

Equations (1) through (7) comprise a closed system of seven scalar equations and seven unknowns, u , v , w , p , ρ , T , and S . The variables, u , v , T , and S are prognostic variables whose time rates of change are predicted from (1), (3), (6) and (7), respectively. Although the diagnostic variables w , p , and ρ can be determined from (3), (4), and (5), respectively, there are additional constraints imposed on p and w by the choice of the rigid lid boundary conditions. The vertically integrated pressure can no longer be obtained by integrating the hydrostatic equation (4) for the free surface. Further, the vertically integrated horizontal velocity is constrained to be non-divergent, i.e.,

$$\int_{-H}^0 \left(\frac{\partial u}{\partial x} + \frac{\partial v}{\partial y} \right) d\epsilon = 0, \quad (8)$$

which is obtained by integrating (3) and applying the vertical boundary conditions.

For any quantity q , let its vertical average be denoted by \bar{q} and its departure (vertical shear) by q' . From (8) the vertical mean flow can then be described by a streamfunction ψ , such that:

$$\bar{u} = -\frac{1}{H} \frac{\partial \psi}{\partial y}, \quad (9)$$

$$\bar{v} = \frac{1}{H} \frac{\partial \psi}{\partial x}. \quad (10)$$

The streamfunction ψ is predicted from the vorticity equation, which is derived from the vertical average of (1) and (2). Applying the curl operator to the vertical average (1) and (2), and using (9) and (10), the vorticity equation is

$$\begin{aligned}
\frac{\partial \zeta}{\partial t} &= \frac{\partial}{\partial t} \left[\frac{1}{H} \left(\frac{\partial^2 \psi}{\partial x^2} \right) + \frac{1}{H} \left(\frac{\partial^2 \psi}{\partial y^2} \right) + \frac{\partial \psi}{\partial x} \frac{\partial H^{-1}}{\partial x} + \frac{\partial \psi}{\partial y} \frac{\partial H^{-1}}{\partial y} \right] \\
&= - \left[\frac{\partial}{\partial x} \left(\frac{f}{H} \frac{\partial \psi}{\partial y} \right) - \frac{\partial}{\partial y} \left(\frac{f}{H} \frac{\partial \psi}{\partial x} \right) \right] \\
&\quad - \left[\frac{\partial}{\partial x} \left(\frac{g}{H \rho_0} \int_{-H}^0 \int_z^0 \frac{\partial \rho}{\partial y} d\epsilon dz \right) - \frac{\partial}{\partial y} \left(\frac{g}{H \rho_0} \int_{-H}^0 \int_z^0 \frac{\partial \rho}{\partial x} d\epsilon dz \right) \right] \\
&\quad + \frac{\partial}{\partial x} \left(\frac{1}{H} \int_{-H}^0 G dz \right) - \frac{\partial}{\partial y} \left(\frac{1}{H} \int_{-H}^0 F dz \right),
\end{aligned} \tag{11}$$

where G and F represent the collected contributions of the nonlinear and viscous terms in equations (1) and (2).

The vorticity equation (11) is solved by obtaining an updated value of ζ by application of the leapfrog (or every 11 time steps, the Euler-backward) time-differencing scheme. The associated value of ψ can then be obtained from:

$$\zeta = \frac{1}{H} \left(\frac{\partial^2 \psi}{\partial x^2} \right) + \frac{1}{H} \left(\frac{\partial^2 \psi}{\partial y^2} \right) + \frac{\partial \psi}{\partial x} \frac{\partial H^{-1}}{\partial x} + \frac{\partial \psi}{\partial y} \frac{\partial H^{-1}}{\partial y}, \tag{12}$$

which is an elliptic equation. A solution to (12) is fully prescribed by specifying the values of ψ on the open and closed boundaries of the model domain. Currently, to solve (12), the model uses an elliptic solver when there are no variations in coastline geometry and/or topography, and successive over-relaxation techniques when there are variations in coastline geometry and/or topography.

The vertical shear current (u' , v') is predicted from (1) and (2) after subtracting the vertical mean. The results are:

$$\frac{\partial u'}{\partial t} = \frac{-1}{\rho_0} \frac{\partial p'}{\partial x} + f v' - A_M \nabla^4 u' + K_M \frac{\partial^2 u'}{\partial z^2} + F - \bar{F} - \frac{\tau^y}{\rho_0 H}, \tag{13}$$

$$\frac{\partial v'}{\partial t} = \frac{-1}{\rho_0} \frac{\partial p'}{\partial y} - f u' - A_M \nabla^4 v' + K_M \frac{\partial^2 v'}{\partial z^2} + G - \bar{G} - \frac{\tau^x}{\rho_0 H}. \tag{14}$$

In (13) and (14), p' , which represents the departure of the pressure from the vertical average, is, using (4), expressed in terms of ρ as:

$$p' = \int_z^0 \rho g d\varepsilon - \frac{1}{H} \int_{-H}^0 \left(\int_z^0 \rho g d\varepsilon \right) dz, \quad (15)$$

where ε is a dummy variable representing the vertical coordinate.

The method of solution consists of predicting $\nabla^2\psi, \psi, u', v', T$, and S from (11), (12), (13), (14), (6) and (7), respectively. The total current is then obtained by adding the vertical shear part to the vertical average part, after the latter is obtained from ψ using (9) and (10). The diagnostics ρ , w , and p' are obtained from (5), (8), and (15), respectively.

C. FORCING CONDITIONS

In this study, to explore the effects of thermohaline forcing on the CCS, seasonal temperature and salinity climatological conditions from Levitus *et al.* (1994) and Levitus and Boyer (1994) are used to initialize the model, and, once a day, to force the model at the western boundary. The seasonal temperature and salinity forcing conditions for the upper seven levels, which are initially assumed to be zonally homogeneous, are shown in Figure 3, for the northern (47.5 °N) and southern (35 °N) boundaries of the model domain. Since the lower three levels do not exhibit much horizontal variation, they are assumed to be constant for each level. The temperature values used for levels 8 to 10 are 2.56°C, 2.08°C, and 2.00°C. The salinity constant used for the lower three levels is 34.7.

While the temperatures to the south are warmer than those to the north at all seven levels, only the upper level temperature conditions (Figure 3a and 3b) show significant seasonal variability with a temperature maximum in September and a temperature minimum in February throughout the whole region. Below these depths, (Figures 3c-3g), both the seasonal temperature fluctuations and the temperature gradient weaken, as expected. In contrast the salinity conditions at all seven levels (Figure 3), which show less (more) saline water to the north (south), have no significant seasonal cycle.

To explore the effects of wind forcing, the model is forced with wind fields on a 2.5° by 2.5° grid from the European Center for Medium-Range Weather Forecasts (ECMWF) near-surface wind analyses (Trenberth *et al.*, 1990). The monthly mean stresses based on twice daily wind analyses from 1980-1989 have been interpolated spatially to the 8 by 11 km model resolution and temporally to daily wind values.

The wind forcing employed is displayed in Figure 2, which depicts the seasonal winds starting with January 15 (day 15). The atmospheric pressure pattern for January (Figure 2a) has a low (i.e., the Aleutian Low) to the north and a high (i.e., the North Pacific High) to the south, which results in a wind divergence near 40°N . This pattern of poleward winds north of 40°N and equatorward winds to the south continues through February and March. During April (Figure 2b) and May the divergence in the wind field migrates poleward. By June an equatorward component in the wind field is observed along the entire domain. The strongest equatorward winds are discernible from July (Figure 2c) through August. By October (Figure 2d) the winds start to weaken throughout the domain, and divergence in the wind field is observed in the north. This divergent wind pattern continues through November. By December the wind divergence has returned to $\sim 40^\circ\text{N}$.

D. EXPERIMENTAL DESIGN

The design of the model experiments is as follows. Experiment 1 examines the model response to seasonal temperature and salinity forcing using the seasonal thermohaline forcing conditions shown in Figure 3. The model integrations start from a state of rest and, once a day, the model is updated for temperature and salinity at the western boundary.

In Experiment 2 the model is forced from rest with seasonal ECMWF winds. The initial mean stratification used is an exponential temperature profile with a vertical length scale of $h=450$ m. The exact form is

$$T(z) = T_B + \Delta T e^{z/h} \quad (16)$$

The approximation assumes $T_B = 2^\circ\text{C}$ to be the temperature at great depth. $\Delta T = 13^\circ\text{C}$ is the increase in temperature between the bottom of the ocean and the surface. This temperature profile is the same profile used by Batteen (1989, 1997) and Batteen *et al.* (1989) and was derived by Blumberg and Mellor (1987) from available CCS observations of the long-term, mean climatological temperature stratification for the CCS region as a whole.

To isolate the effects of wind forcing in Experiment 2, the net heat flux at the sea surface is zero. In this way, any heat flux that is discernible will have been generated by an increase or decrease of sea surface temperature resulting from wind-forcing effects (Batteen *et al.*, 1989). To accomplish this, an initial air temperature is chosen that forces the net flux of longwave radiation, sensible heat, and latent heat to balance the heating due to solar radiation. This air temperature is then used in the model for all wind forcing experiments. Any subsequent surface heat flux forcing is therefore a secondary effect of the changes to the sea surface temperature due to the wind forcing.

Experiment 3 combines the thermohaline forcing along the western boundary (Figure 3) with the seasonal ECMWF wind forcing to study the model response to both types of forcing on the CCS. The model integrations start from a state of rest and, once a day, the model is updated with ECMWF winds and, at the western boundary, with temperature and salinity.

III. RESULTS FROM MODEL SIMULATIONS

A. EXPERIMENT 1 - SEASONAL TEMPERATURE AND SALINITY FORCING

1. Spin-up Phase

As expected, when the temperature decreases poleward (Figure 3), the pressure gradient due to the temperature gradient establishes an onshore geostrophic inflow in the interior ocean (Figure 4). Because the initialized alongshore temperature field is not constant, the onshore flow varies between ~ 2 and 5 cm/s. On approaching the eastern boundary, the onshore flow turns and forms a poleward boundary current (e.g., Figure 4a), which advects warm water from the equatorial end of the model domain. Because it is continually augmented downstream by additional onshore flow, the poleward current increases in magnitude towards the pole, so that by day 45 maximum velocities on the order of ~ 30 cm/s are observed near the poleward end of the model domain (Figure 4b). As time progresses, the onshore geostrophic flow weakens in the southern region to ~ 1 and 2 cm/s. The poleward boundary current also weakens so that by day 180 (Figure 4c) maximum speeds have decreased from ~ 30 cm/s at day 45 to ~ 20 cm/s. A minimum speed of ~ 10 cm/s is reached by day 255 (Figure 4d), and is maintained throughout.

The onshore pressure gradient due to the thermohaline gradient is sufficient to establish an unstable equatorward flow (e.g., see day 63 in Figure 5). The strongest equatorward flow (~ 5 cm/s) is in the coastal, poleward end of the domain and is maintained throughout.

Baroclinic/barotropic instabilities in the poleward surface current and equatorward undercurrent result in the generation of meanders near the coast. By day 180 (Figure 4c) an anticyclonic eddy develops at $\sim 43^\circ\text{N}$, subsequently intensifies and propagates westward. From days 180 to 255 (Figures 4c and 4d), other eddies develop equatorward of this eddy, and in time intensify and propagate westward.

The surface (e.g., Figure 4c) and subsurface (e.g., Figure 5) velocity fields superimposed on the density fields illustrate that away from the eddy generation region, the flow is predominantly parallel to the isopycnals, as expected for geostrophic flow. In the eddy generation region, i.e., in the poleward end of the model domain, there is significant advection of less dense water offshore by the anticyclonic eddies.

2. Quasi-equilibrium Phase

Longer experimental runs show that the system has reached a quasi-steady state and that these features continue to be generated and maintained. Using the results of the longer experimental runs (i.e., year 3 of model simulation time), the model output is time-averaged every 3 days to see the structure of features in the CCS. As a result of geostrophic inflow due to the pressure gradient, both a poleward surface current and an equatorward undercurrent are generated. Figure 6 shows the vertical structure of a coastal poleward surface current with velocities of ~8-10 cm/s overlying a coastal equatorward undercurrent with velocities of ~1-6 cm/s below ~150-300m depth in the poleward part of the model domain.

The presence of both a poleward surface current and an equatorward undercurrent has been observed by Hickey (1979, 1997) off the coast of Washington. During the fall, the coastal poleward surface current has been observed to have speeds of ~5-20 cm/s and to occur above ~150-300 m depth. The equatorward undercurrent has also been observed to have speeds of less than 10 cm/s, and to occur below ~150-300 m depth. These observations are consistent with the results of the fall model simulations near the coast of Washington (e.g., Figure 6b).

Due to vertical and horizontal shear instabilities between the poleward surface current and the equatorward undercurrent, anticyclonic eddies are generated in the coastal poleward end of the model domain. In time they intensify and propagate westward (e.g., Figure 7). The eddies tend to be $O(100)$ km in size and extend to depths of ~300 m or deeper (not shown).

B. EXPERIMENT 2 - SEASONAL WIND FORCING

1. Spin-up Phase

Initially, the oceanic response to the climatological wind pattern (Figure 2) that is used to force the model from rest, spins up linearly. In response to the prevailing poleward winds in the northern part of the model domain, a surface poleward coastal current of ~ 3 cm/s develops in the poleward end of the model domain within ~ 100 km of the coast. After being present for ~ 45 days, it retreats farther poleward following the migration of the Aleutian Low. As expected, equatorward wind forcing in the south results in an equatorward surface current (the CC) in the equatorward end of the model domain. By spring, with the arrival of the North Pacific High along the west coast of North America, the current extends all along the coast. A coastal, poleward undercurrent (the CUC) develops below the surface equatorward current, initially in the equatorward end of the model domain, and, during the upwelling season, along the entire coast.

As the core of the CUC intensifies, it shoals and displaces the core of the CC farther offshore (e.g., compare Figures 8a and 8b). As a result, there are strong vertical and horizontal shears in the upper layers between the CC and the CUC. Because this current is baroclinically and barotropically unstable, meanders, filaments, and eddies subsequently develop.

The equatorward CC develops fairly uniformly along the coast, while the upwelling, observed as isolated, closed temperature contours, is relatively patchy (Figure 9). In particular, the coldest, upwelling water is often found at or equatorward of large promontories (e.g., Cape Mendocino in Figures 9c and 9d). Since promontories are areas of the irregular coastline where the alongshore component of the wind stress is at a local maximum, the CC, upwelling, and growth of filaments should be enhanced in these regions during the upwelling season (Batteen, 1997).

The filaments that develop are “anchored” off of Cape Blanco, Cape Mendocino, and Point Arena (e.g., Figure 9b and 9c). The equatorward CC also form meanders in the vicinity of capes, which intensify and develop into predominantly cyclonic eddies. In time, these eddies coalesce with other cyclonic eddies to form relatively large (~100-300 km diameter) eddies. After the upwelling season, the equatorward CC takes the form of a meandering jet embedded with several cyclonic eddies (e.g., Figure 9d).

2. Quasi-equilibrium Phase

Using year 3 of the results of the longer experimental runs, we time average the model output every 3 days for the months of January, April, July, and October to see the seasonal structure of features in the CCS. The results show that in spring (Figure 10a) and summer (Figure 10b), and throughout the upwelling season (Figure 11a), there is a coastal, equatorward flow with speeds of ~30-80 cm/s that leaves the coast between ~42°N and 43°N, in the vicinity of Cape Blanco, and meanders downstream. The current then takes the form of a meandering jet. The jet has alongshore wavelengths of several hundred kilometers and cross-shore excursions of several hundred kilometers, and it can extend to depths of ~700 m (e.g., Figure 11b). South of ~43°N, inshore of the jet, there are both cyclonic and anticyclonic eddies. The cyclonic eddies tend to form in the vicinity of the capes. A comparison of the spring (Figure 10a) and summer (Figure 10b) velocity and temperature fields shows that as the eddies move westward, they become embedded in the meandering jet. The results of the lower layer velocity fields, averaged over the upwelling season (Figure 11c) show that there is a coastal poleward undercurrent, with speeds of ~10-20 cm/s, within ~100 km of the coast.

After the upwelling season, i.e., in fall (e.g., Figure 10c), a poleward flow, with speeds of ~10-20 cm/s, develops within ~100 km of the coast and subsequently replaces the coastal, equatorward flow. Offshore of the poleward flow are several cyclonic eddies. Farther offshore, there is a relatively strong (~50 cm/s) equatorward, meandering jet embedded with both cyclonic and anticyclonic eddies.

In the winter (e.g., Figure 10d), in the poleward region of the model domain, the meandering jet has been displaced farther offshore by the westward propagation of cyclonic eddies. In the equatorward part of the model domain, the jet meanders closer to shore, i.e., from $\sim 128^\circ\text{W}$ at 41°N to $\sim 125^\circ\text{W}$ at 38°N . Offshore and inshore of the jet, both cyclonic and anticyclonic eddies fill much of the model domain. A relatively strong surface poleward flow near the coast is still present north of $\sim 41^\circ\text{N}$.

C. EXPERIMENT 3 - SEASONAL WIND AND THERMOHALINE FORCING

1. Spin-up Phase

Due to the combination of thermohaline and wind forcing, different oceanic responses are expected depending on the season. In the winter, in the poleward end of the model domain, the large high-to-low pressure gradient due to the warm-to-cold temperature gradient establishes an onshore geostrophic flow, while the poleward wind stress results in onshore Ekman flow. On approaching the eastern boundary, the onshore flow turns and forms a poleward boundary current (e.g., Figure 12a). In the equatorial end of the model domain, the smaller pressure gradient and the equatorward wind stress results in weak onshore geostrophic flow, offshore Ekman flow, and a coastal equatorward surface current (e.g., Figure 12a).

During the upwelling season (\sim April to September) (e.g., Figures 12b-12d), the combination of a weakened pressure gradient and increased equatorward winds over the entire model domain lead to a strengthening of equatorward flow all along the coast and a weakening (strengthening) of onshore (offshore) flow. As in Experiment 2, the upwelling is relatively patchy with the coldest water found near coastal promontories (e.g., Cape Blanco in Figure 12d). The subsurface structure of the currents shows that there is a poleward undercurrent (e.g., Figure 13a). The undercurrent is within ~ 150 km of the coast, extends from ~ 150 to greater than 700 m depth, and has a core velocity of ~ 5 cm/s. Typical core velocities for the undercurrent range from ~ 5 to 20 cm/s. The surface coastal

equatorward flow extends to ~ 150 m depth-near shore to ~500 m depth offshore. The core of the surface current is within ~100 km of the coast and has a typical core velocity of ~50-70 cm/s. The upwelling season model simulations are consistent with observed depths and velocities of both the surface equatorward current and the poleward undercurrent (e.g., Huyer *et al.*, 1991).

In the fall, as expected, the surface poleward flow strengthens in the coastal poleward end of the model domain in response to both the strengthening of the pressure gradient and the return of poleward wind stress in the region. The subsurface structure of the currents shows that in the poleward end of the model domain, there is an equatorward undercurrent (e.g., Figure 13b). The undercurrent is within ~30 km of the coast, extends from ~150-700 m depth, and has a core velocity of ~2 cm/s. Typical velocities for the undercurrent range from ~2 to 5 cm/s. As in Experiment 1, the fall model simulation in the poleward end of the model domain is consistent with the observed depths and velocities of both the surface poleward current and the equatorward undercurrent near the coast of Washington (Hickey, 1979, 1997).

2. Quasi-equilibrium phase

Longer run times (~3 years) of the model simulation show that during the upwelling season many of the features simulated in Experiment 2, such as meanders, eddies, a temperature front, and filaments (e.g., Figures 10 and 11) are also, as expected with the dominance of wind forcing, simulated in Experiment 3. A comparison of these features for Experiments 2 and 3 during the upwelling season (Figures 11a and 14, respectively) shows that the results are qualitatively similar except that there is a tighter temperature gradient inshore of ~125°W between Cape Mendocino and Point Arena in Experiment 3. This must be due to the onshore geostrophic flow resulting from the alongshore pressure gradient. An examination of recent CCS observations by Strub and James (1995) shows that during the upwelling season (e.g., see Figure 2a of Strub and

James, 1995) the temperature front between Cape Mendocino and Point Arena is found inshore of $\sim 125^\circ\text{W}$, consistent with the model simulation of Experiment 3.

Due to the thermal wind relationship, stronger surface and subsurface currents inshore of $\sim 125^\circ\text{W}$ in Experiment 3 are also found between Cape Mendocino and Point Arena. For example, Figures 15a and 15b show that the surface coastal jet with velocities of ~ 10 cm/s north of Cape Mendocino (Figure 15a) intensifies to ~ 50 cm/s at Cape Mendocino (Figure 15b), while the undercurrent with velocities of ~ 15 cm/s north of Cape Mendocino intensifies to ~ 25 cm/s at Cape Mendocino.

In the poleward end of the model domain, a comparison of subsurface currents (not shown) for Experiments 2 and 3 shows that the velocities for the undercurrent decrease from ~ 45 cm/s in Experiment 2 to ~ 20 cm/s in Experiment 3. The reduction in the velocities for the poleward undercurrent is likely due to the net result of a poleward undercurrent generated by wind forcing opposing an equatorward undercurrent generated by thermohaline forcing in this region. These lower undercurrent velocities are more consistent with available observations of the undercurrent (e.g., Huyer *et al.*, 1991).

Horizontal maps of the upper layer mean kinetic energy (MKE) and eddy kinetic energy (EKE), averaged over the duration of the upwelling season, are shown in Figures 16a and 16b. Maps of MKE and EKE are suggestive of where the mean and eddy energy sources are to be found (Holland *et al.*, 1983). A comparison of Figures 14 and 16 shows that high values of MKE and EKE are found all along the coastal and offshore axes of the equatorward jet, and in the offshore regions south of $\sim 42^\circ\text{N}$.

A comparison of Figures 16a and 16b shows that maximum values of MKE and EKE occur in the same region, i.e., inshore of $\sim 125^\circ\text{W}$ between Cape Mendocino and Point Arena. Note that the MKE values are larger than the EKE values in the region. This is consistent with the results of Batteen (1997), which showed that the eddies are generated from instabilities of the mean equatorward current and the poleward undercurrent via baroclinic and/or barotropic instability processes.

Maps of EKE for each month during the upwelling season (not shown) show that the maximum EKE always occurs between ~ 37 to 39°N and between 124 and 128°W . The maps also show that high values of EKE are present throughout the upwelling season between Cape Mendocino and Point Arena, while off of Cape Blanco, EKE values steadily increase from small to large values as the upwelling season progresses, with highest values occurring in July and August. These results suggest that the greatest eddy activity off of Cape Blanco occurs after June, while eddy activity between Cape Mendocino and Point Arena occurs regularly throughout the upwelling season.

Since Kelly *et al.* (1997) have most recently used observational results to investigate the variability of near surface EKE in the CCS, we qualitatively compare the EKE results of our model simulation with their observations. Both Kelly *et al.* (1997) and our results show the location of the maximum EKE to be between ~ 36 and 40°N , and at $\sim 125^\circ\text{W}$ during the upwelling season. This region of maximum EKE coincides with increased equatorward flow in both our model simulations and their observations. Both Kelly *et al.* (1997) and our results (not shown) also show that, south of $\sim 40^\circ\text{N}$, on a seasonal time scale the region of monthly maximum EKE migrates westward to $\sim 128^\circ\text{W}$.

After the upwelling season, i.e., in the fall, the combination of wind and thermohaline forcing results in the seasonal changes in the currents in the poleward end of the model domain. In particular, the reversal of winds from equatorward to poleward combined with the intensification of the alongshore pressure gradient results in a shoaling of the poleward undercurrent near the coast of Oregon and Washington, as seen in the latitudinal sequence of Figures 17a-17c. These results are consistent with the hypothesis of Hickey (1989, 1997) that a surface poleward current can result from a shoaling of the undercurrent.

On the basis of these results we can conclude that, even though the effects of wind forcing dominate the CCS, the additional effects of the thermohaline forcing result in the following: the development of a poleward surface current and an equatorward undercurrent in the poleward end of the model region; an onshore geostrophic

component, which results in a temperature front and stronger surface and subsurface currents between Cape Mendocino and Point Arena; and a region of maximum EKE inshore of $\sim 125^{\circ}\text{W}$ between Cape Mendocino and Point Arena, associated with the temperature front. These results seem credible given that the phenomenological behavior of the model simulation has been shown to be qualitatively similar to recent large-scale hydrographic, altimetric, drifter and moored observations of the CCS.

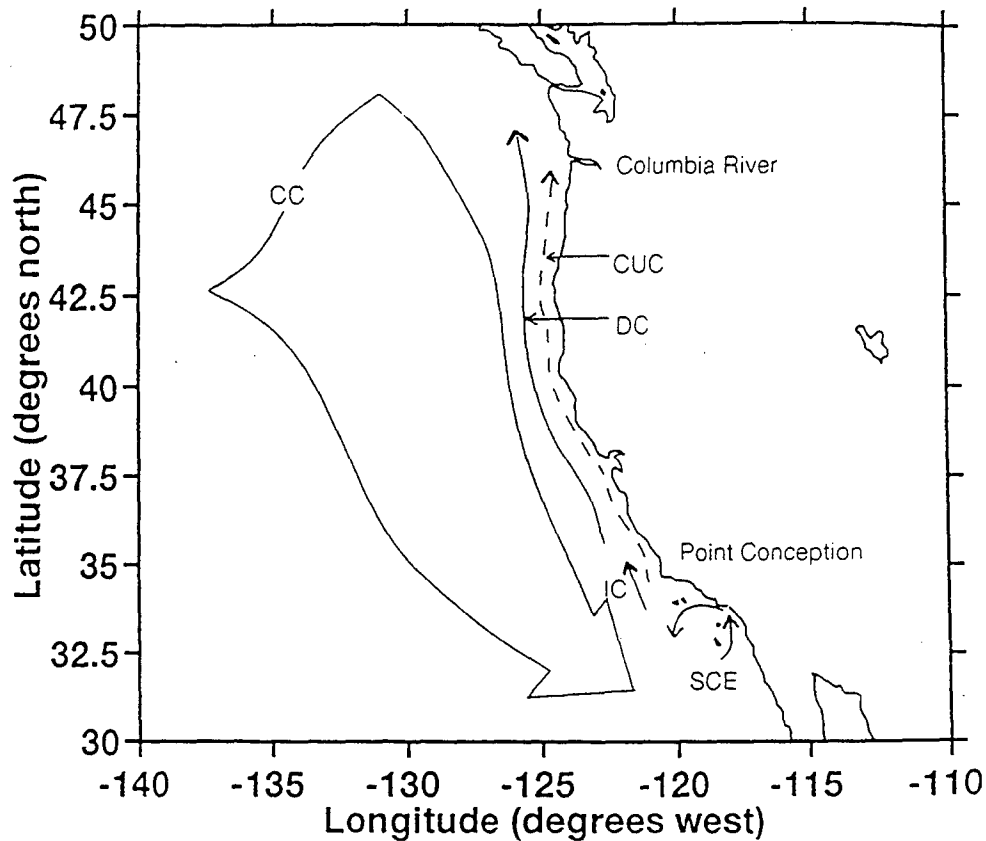


Figure 1. Generalized circulation schematic of the classical climatological California Current System (CCS). The broad, slow surface equatorward California Current (CC) overlies the poleward California Undercurrent (CUC) along with the Inshore Countercurrent (IC), known as the Davidson Current (DC) north of Point Conception and as the Southern California Eddy (SCE) south of Point Conception.

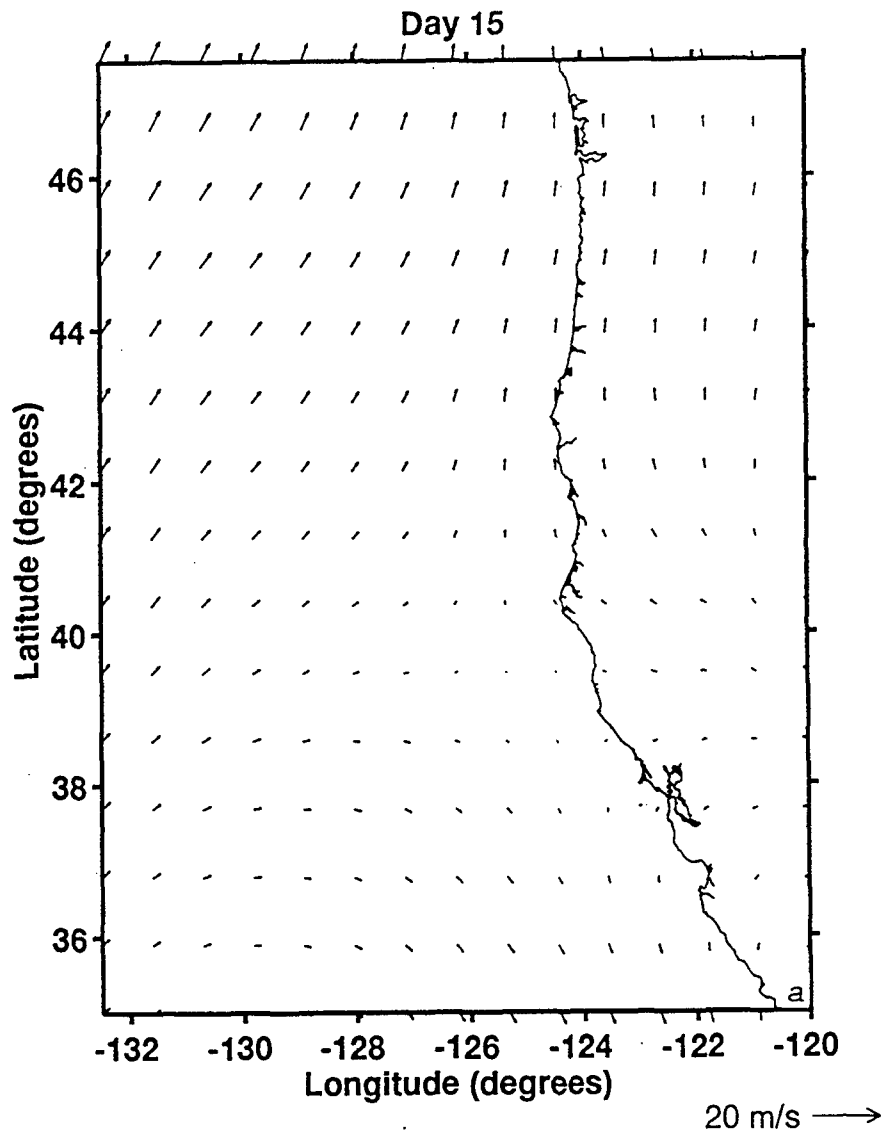
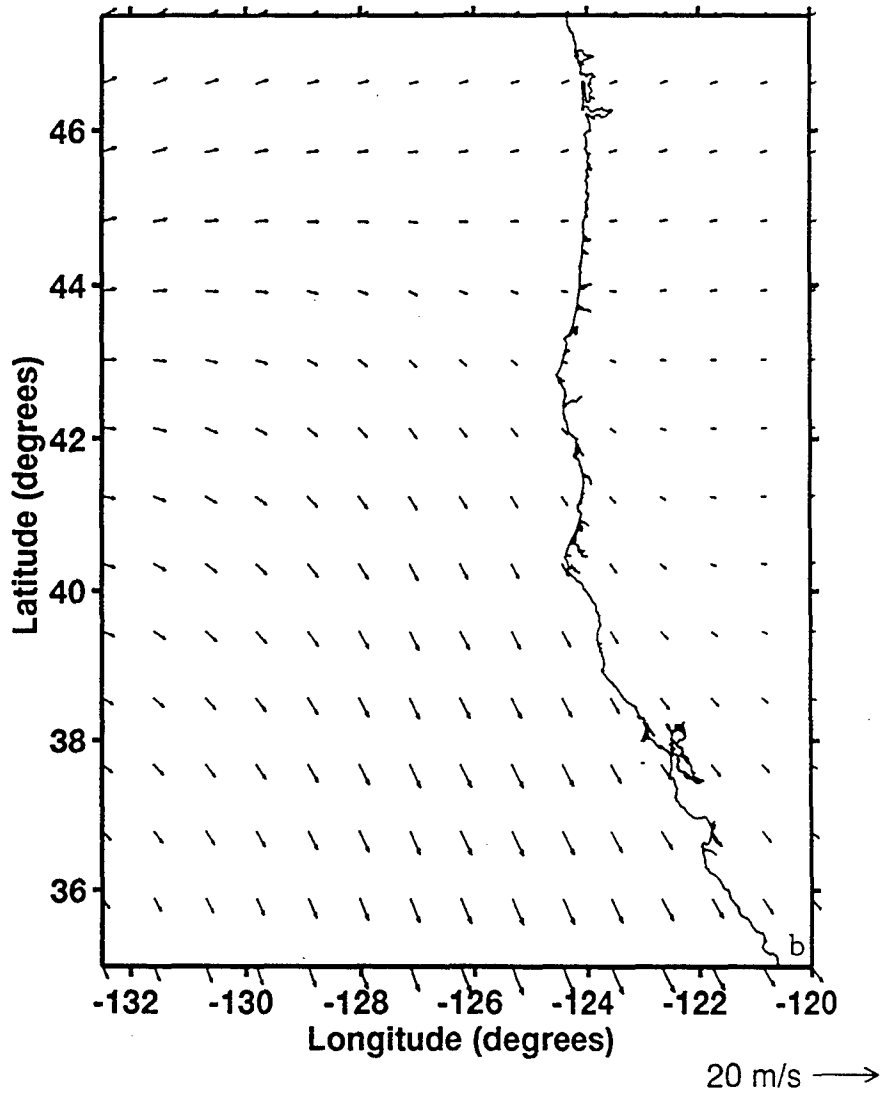
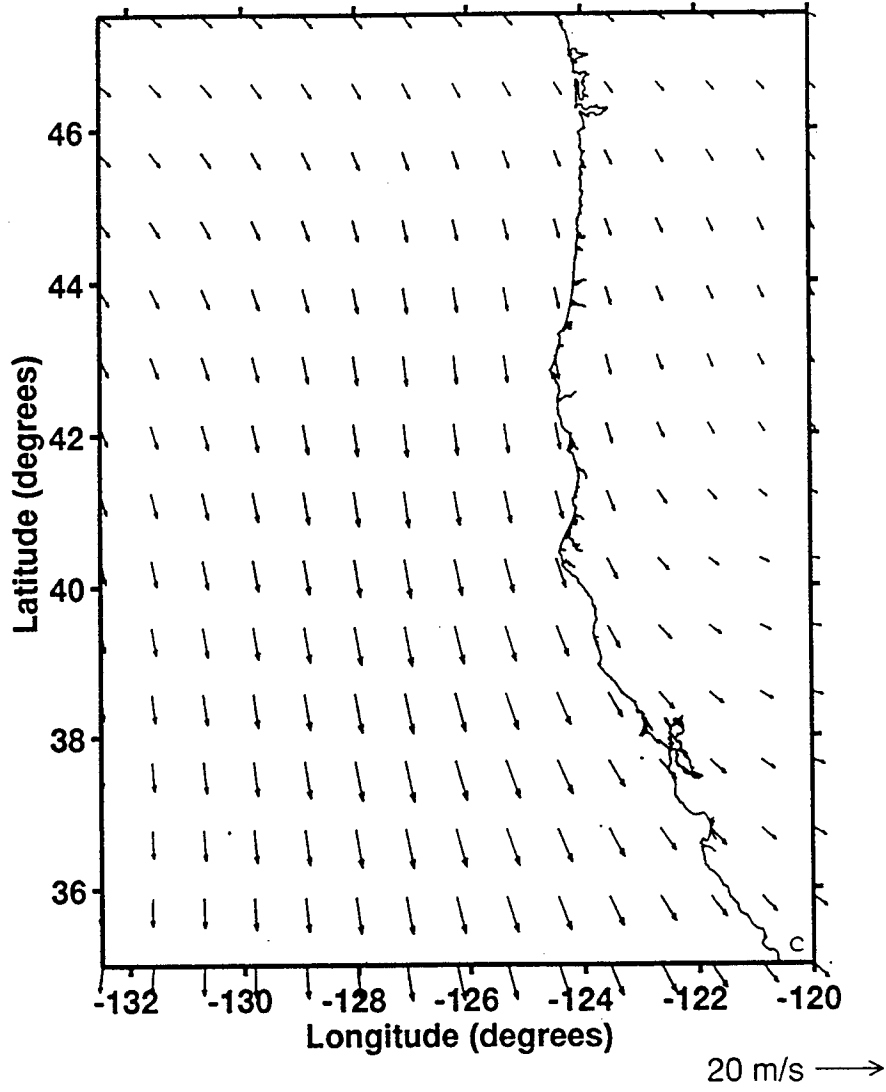


Figure 2. Domain and climatological winds of the model for the California Current System (CCS) off the Western United States. The domain of the model is bounded by 35°N to 47.5°N, 120°W to 132.5°W. The climatological (1980-1989) ECMWF winds used in Experiments 2 and 3 in m/s are shown here for (a) January, (b) April, (c) July, and (d) October. Maximum wind vector is 20 m/s.

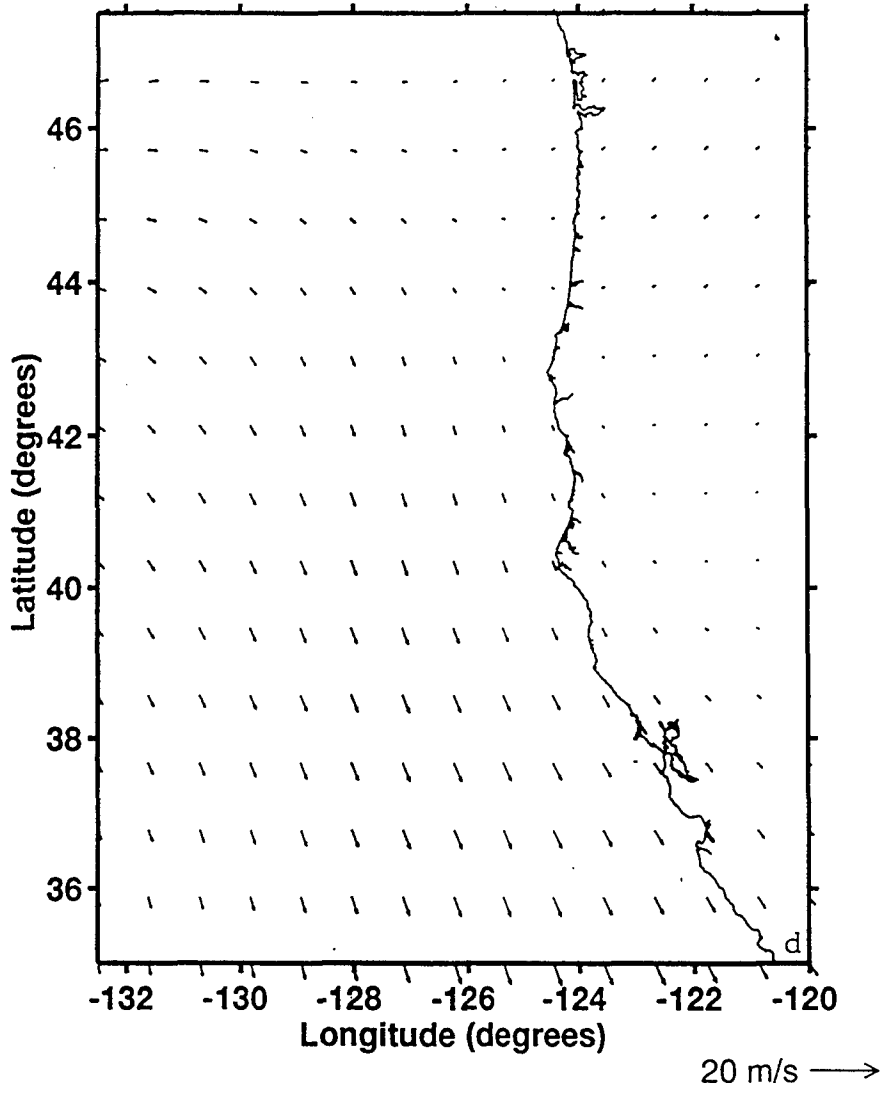
Day 105



Day 195



Day 285



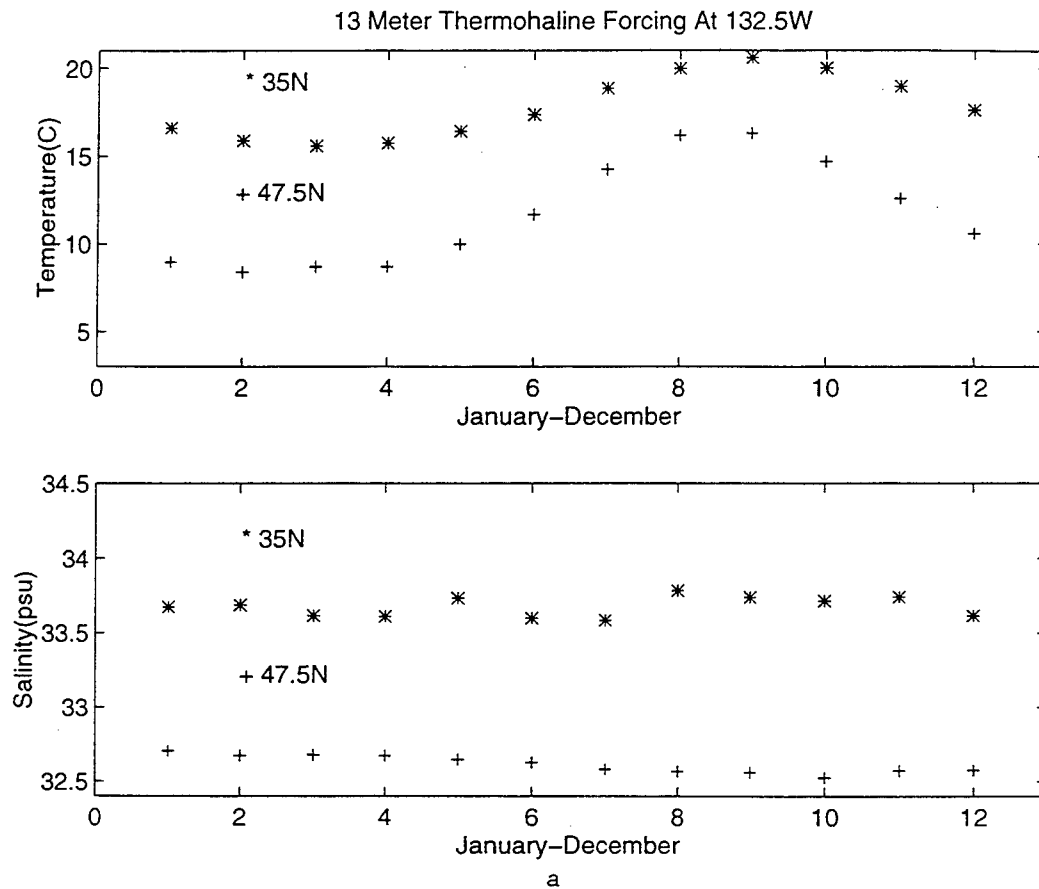
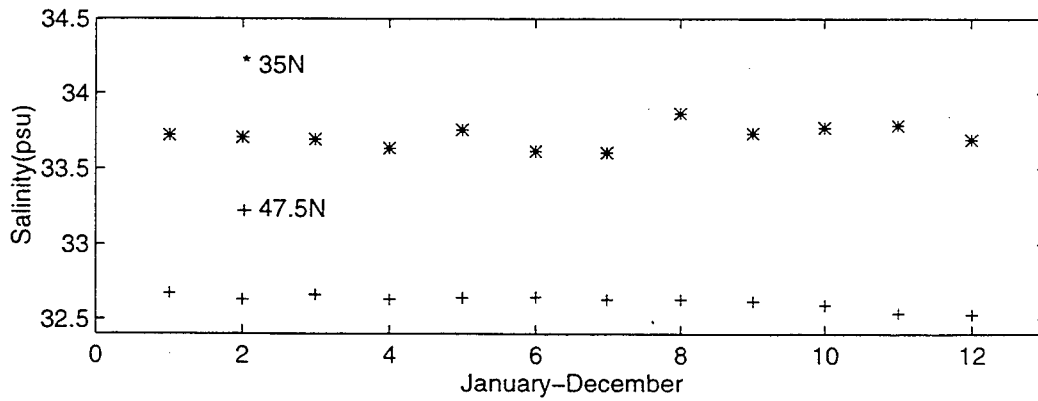
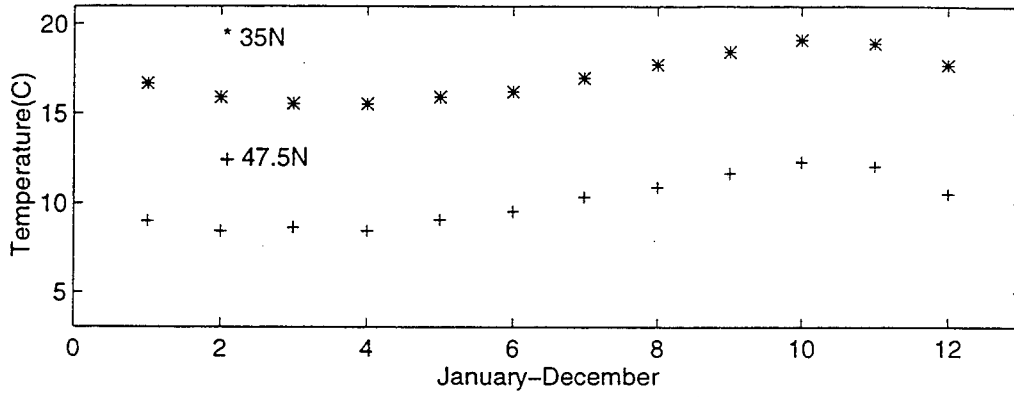


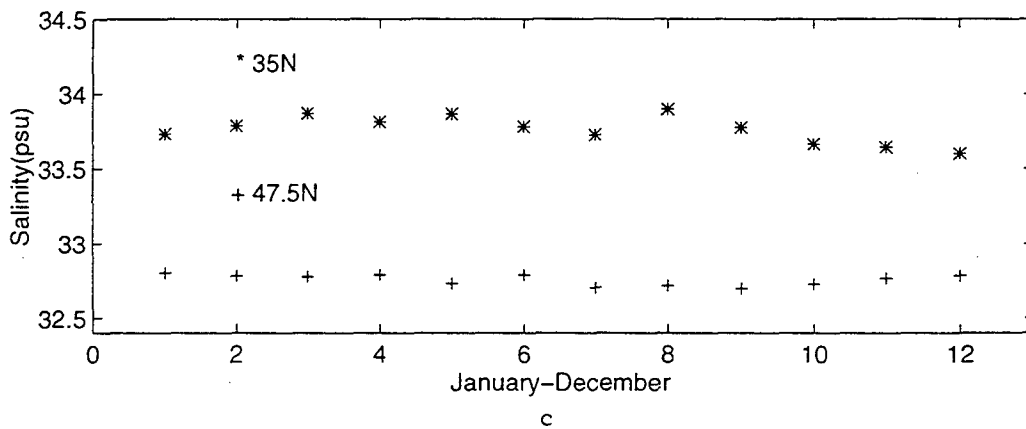
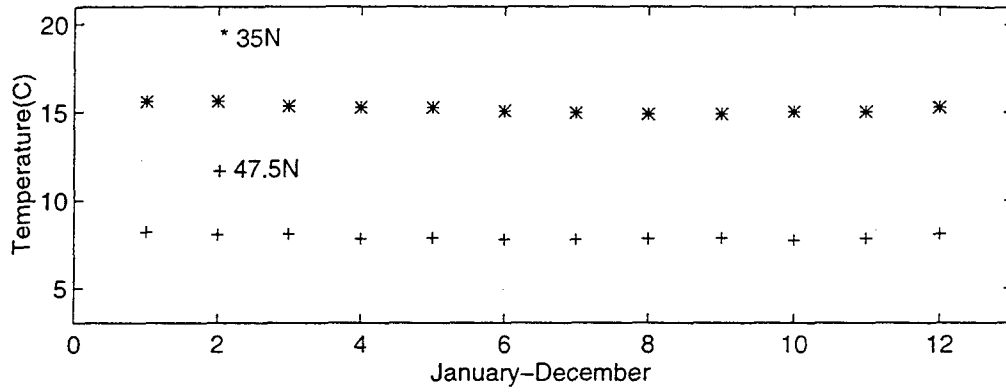
Figure 3. Time series plot of monthly temperature and salinity fields used as seasonal forcing in Experiments 1 and 3. The ‘*’ symbol represents data at 35°N, 132.5W, while the ‘+’ plot represents data at 47.5°N, 132.5W for levels: (a) 13 m, (b) 46 m, (c) 98 m, (d) 182 m, (e) 316 m, (f) 529 m, and (g) 870 m depth.

46 Meter Thermohaline Forcing At 132.5W

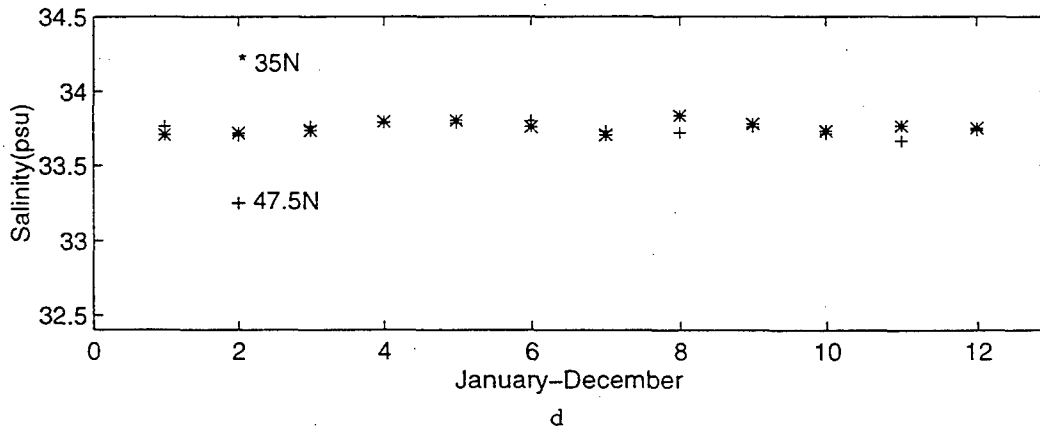
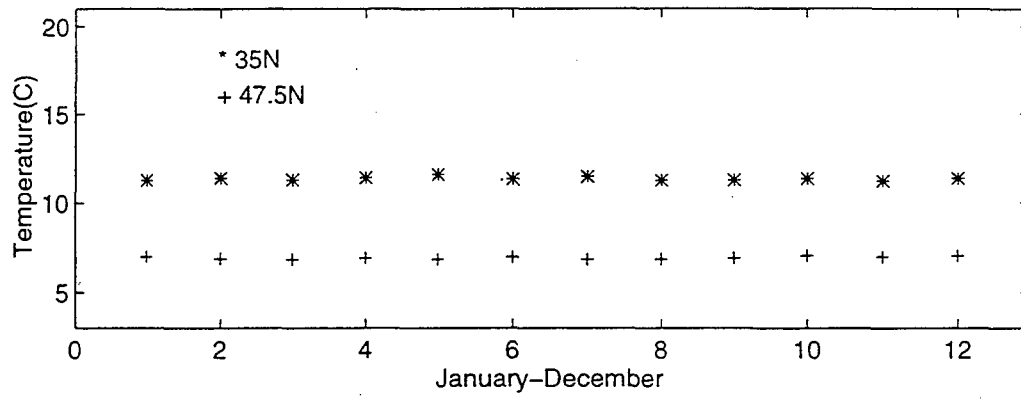


b

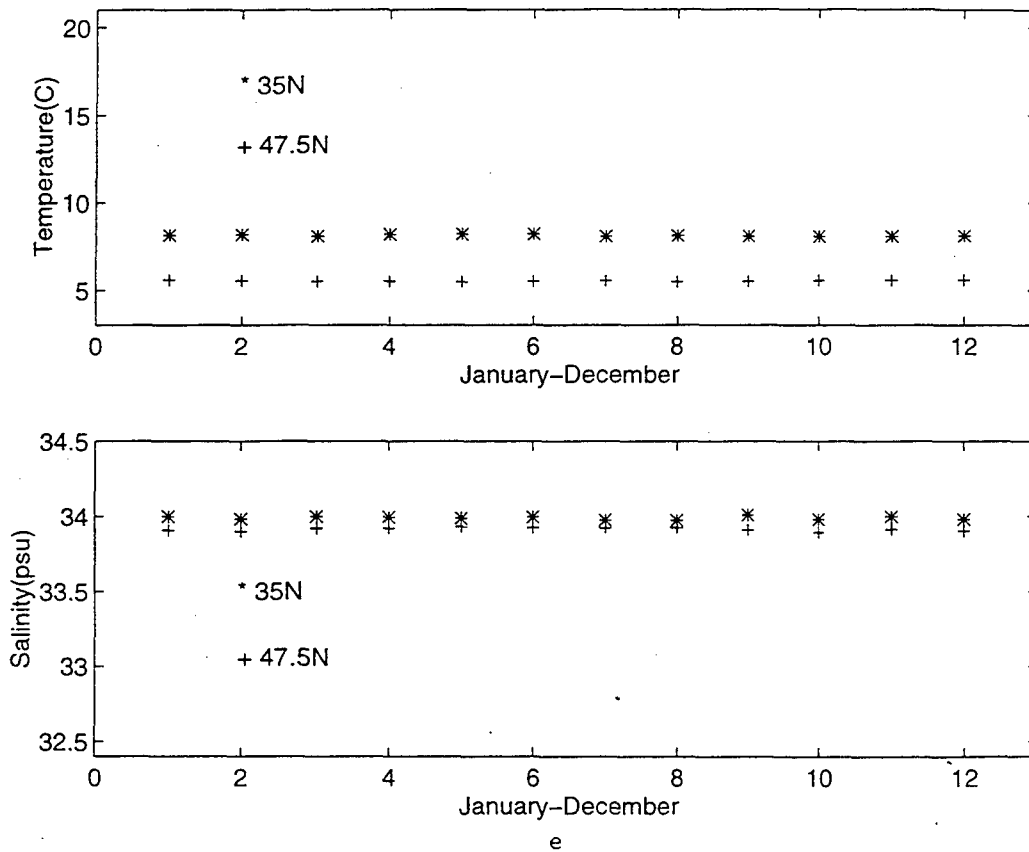
98 Meter Thermohaline Forcing At 132.5W



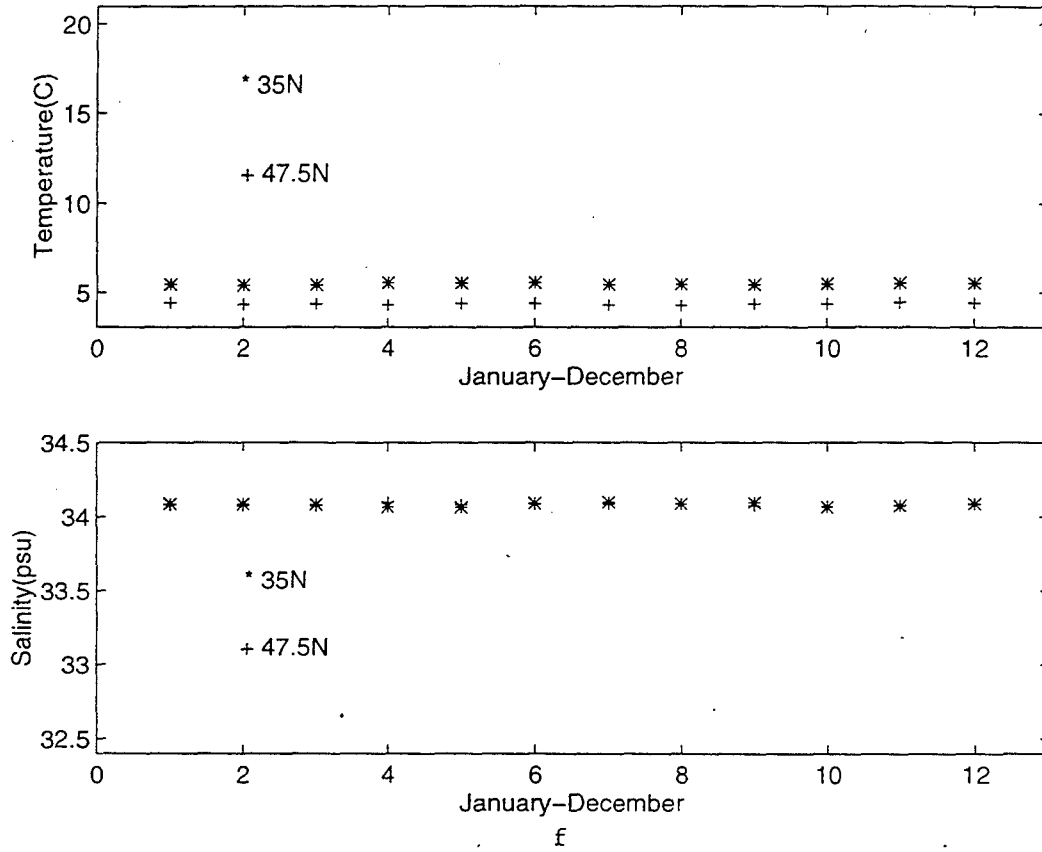
182 Meter Thermohaline Forcing At 132.5W



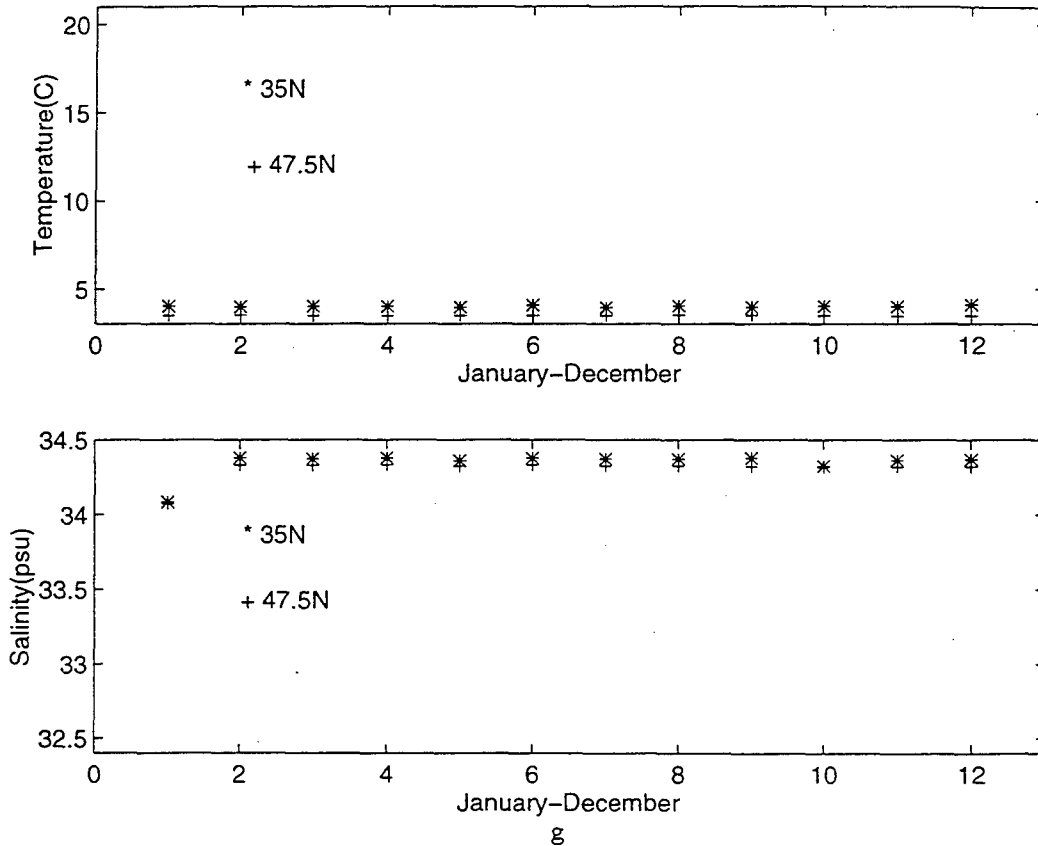
316 Meter Thermohaline Forcing At 132.5W



529 Meter Thermohaline Forcing At 132.5W



870 Meter Thermohaline Forcing At 132.5W



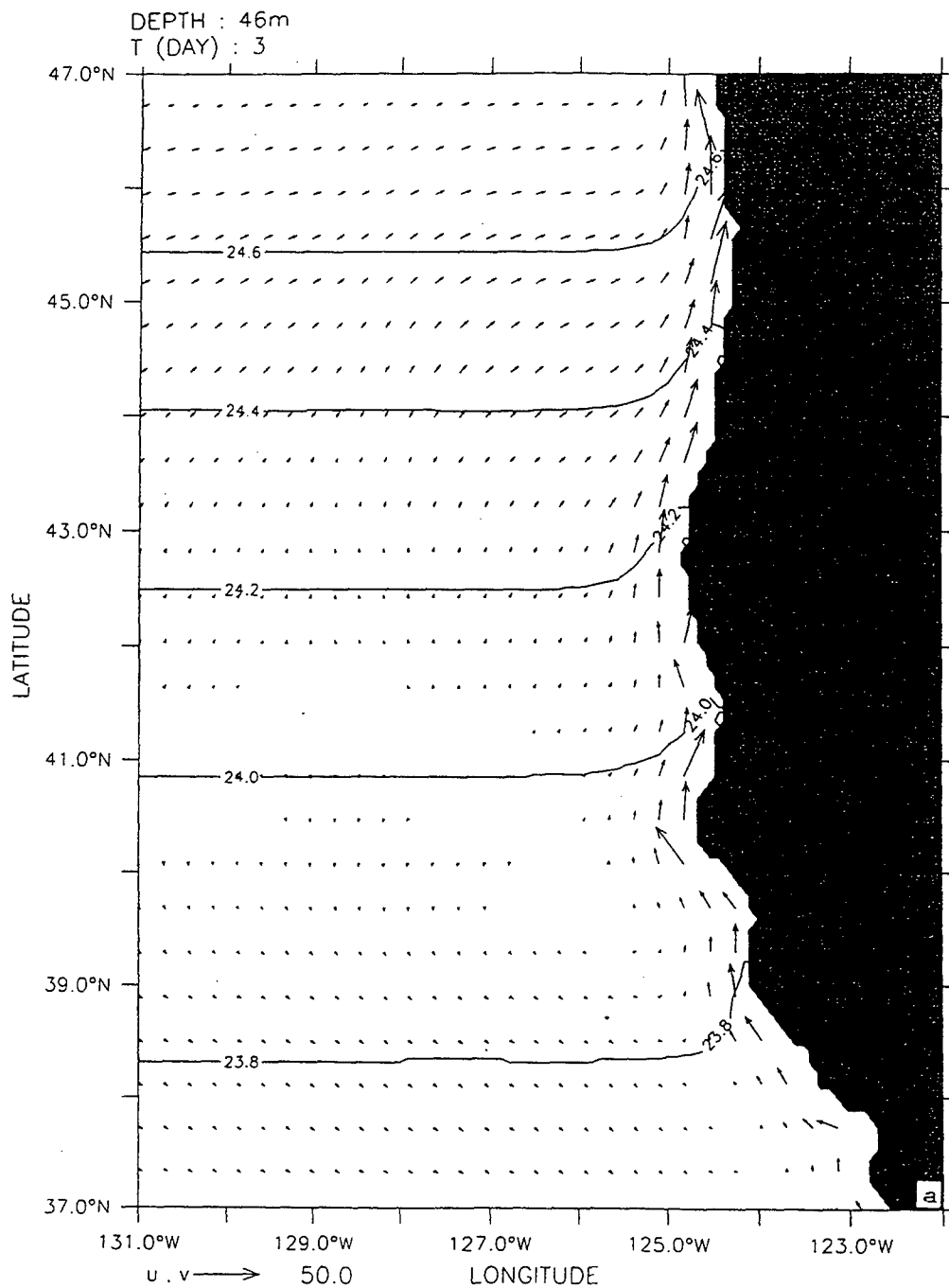
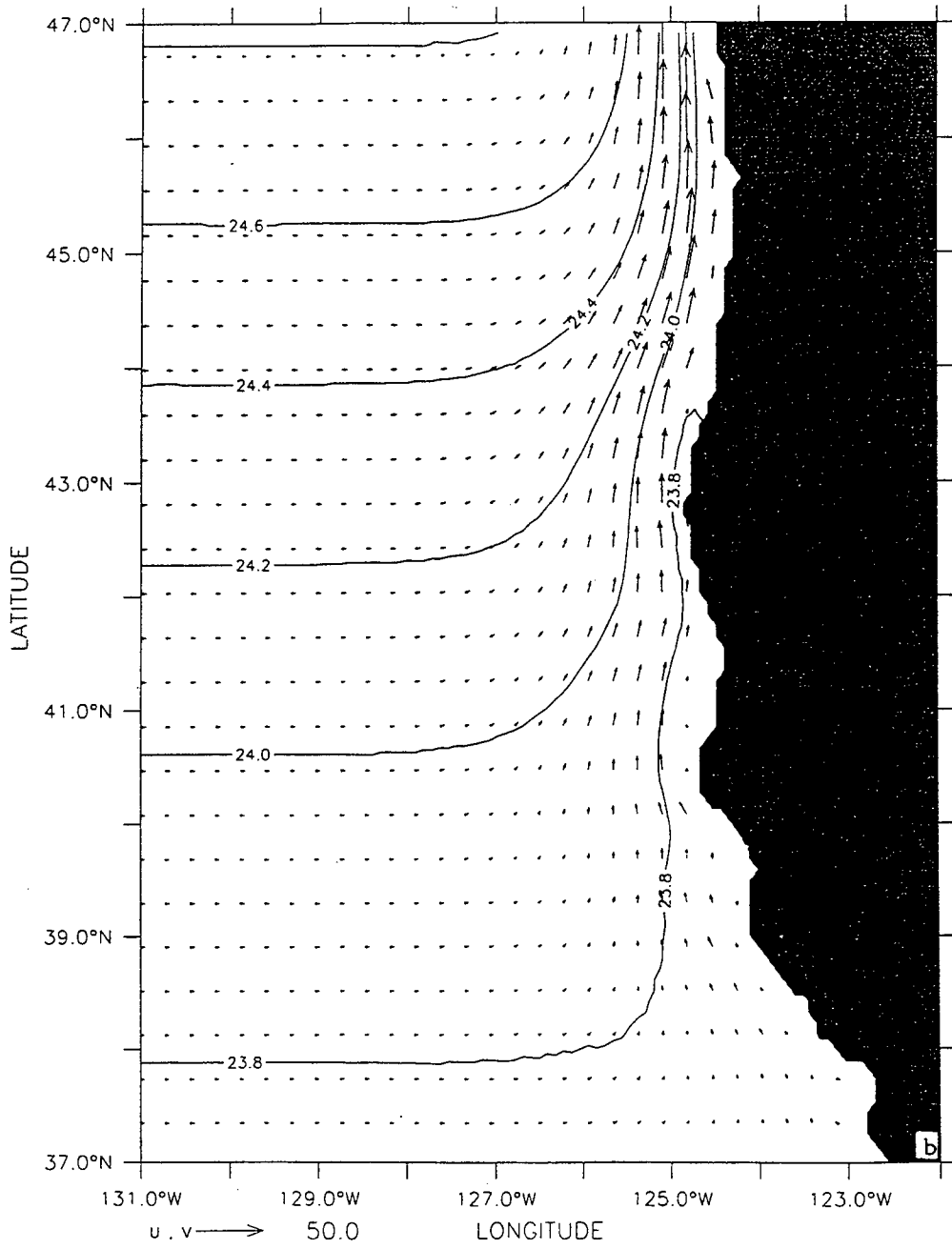
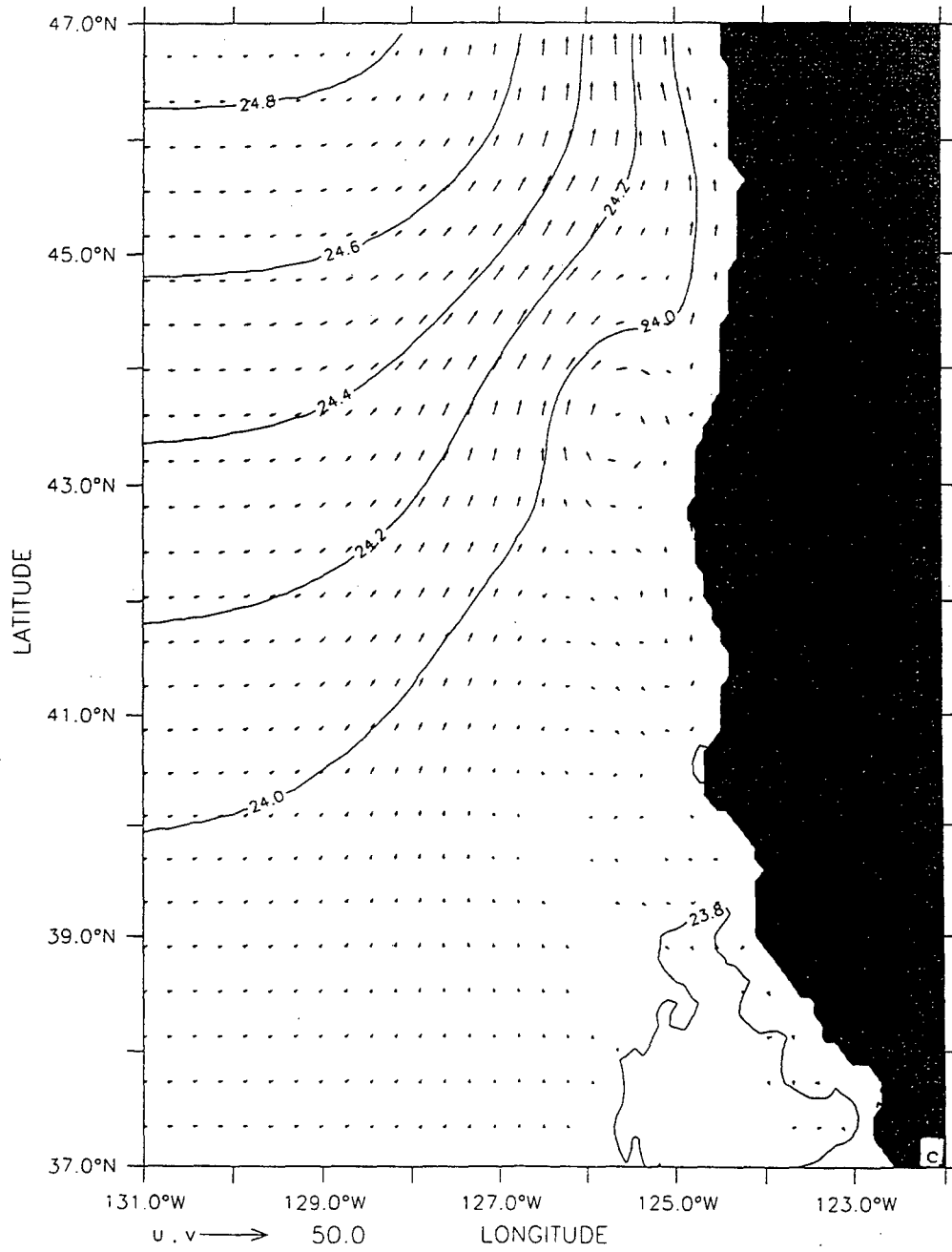


Figure 4. Density contours and velocity vectors at 46 m depth for Experiment 1 at days (a) 3, (b) 45, (c) 180, and (d) 255. In all the velocity fields presented, to avoid clutter, velocity vectors are plotted every third (fourth) grid point in the cross-shore (alongshore) direction. Contour interval is 0.2 gm/cm³; maximum velocity vector is 50 cm/s.

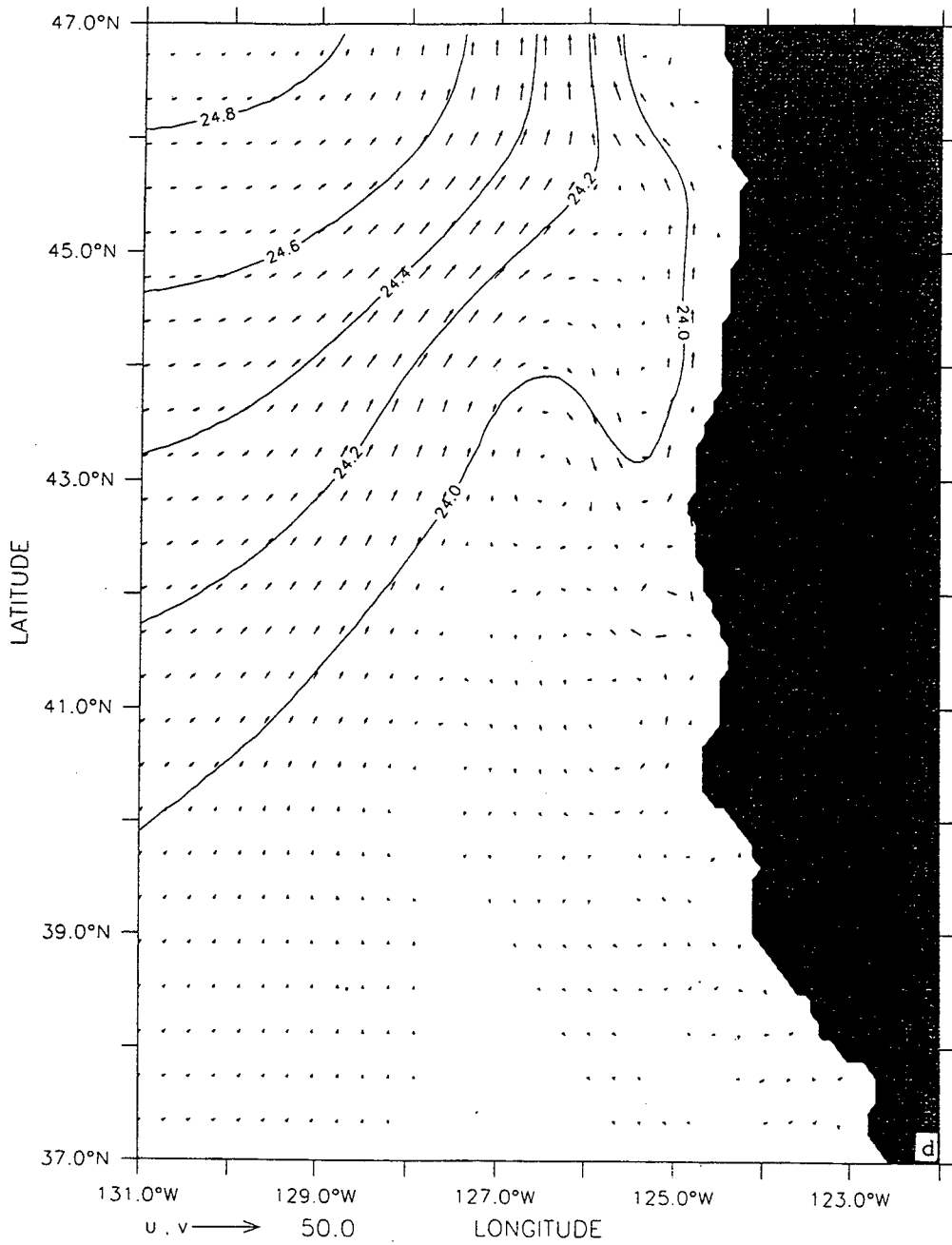
DEPTH : 46m
T (DAY) : 45



DEPTH : 46m
T (DAY) : 180



DEPTH : 46m
T (DAY) : 255



DEPTH : 529m
T (DAY) : 63

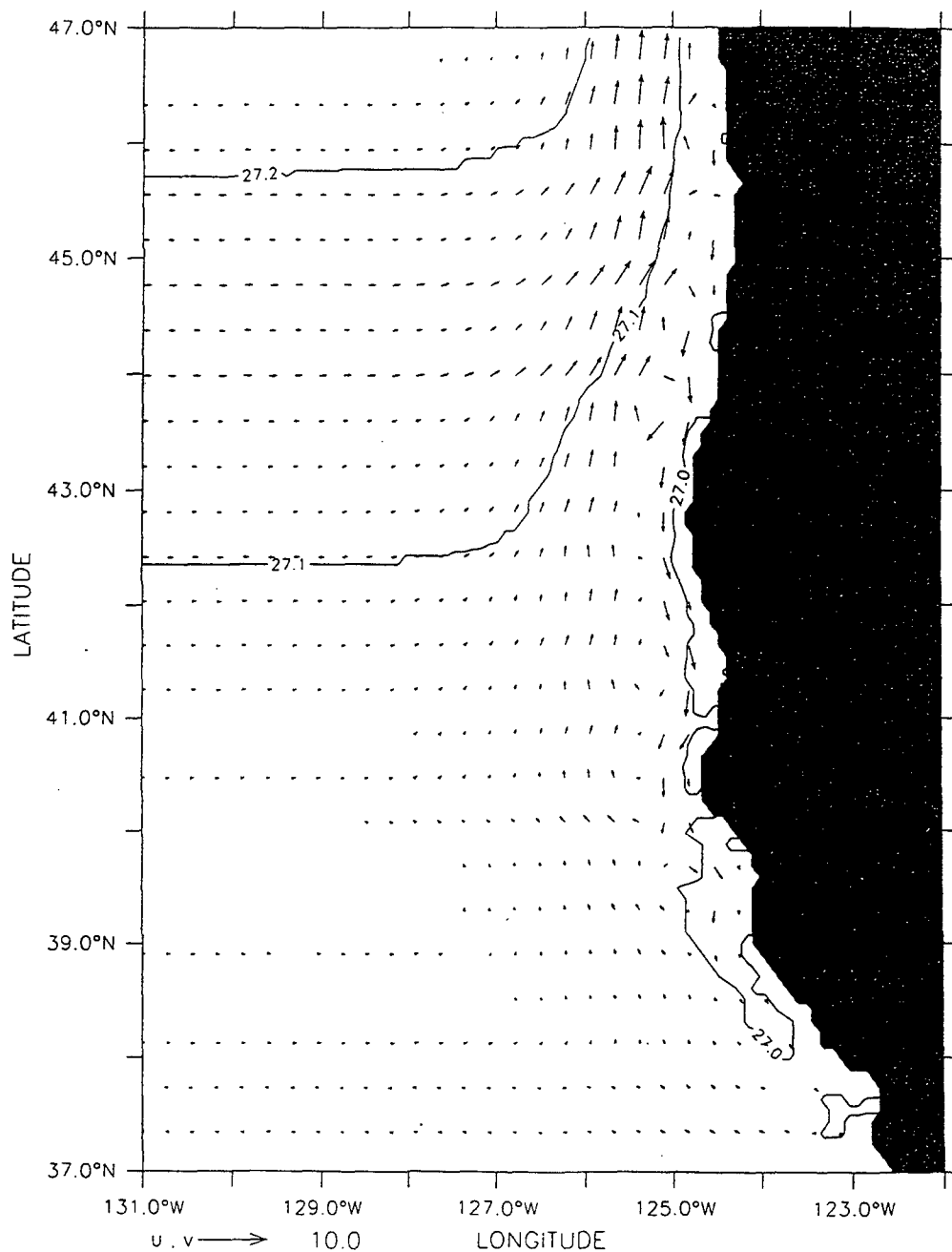


Figure 5. Density contour and velocity vectors at 529 m depth for Experiment 1, day 63. Contour interval is 0.2 gm/cm³; maximum velocity vector is 10 cm/s.

LATITUDE : 46N

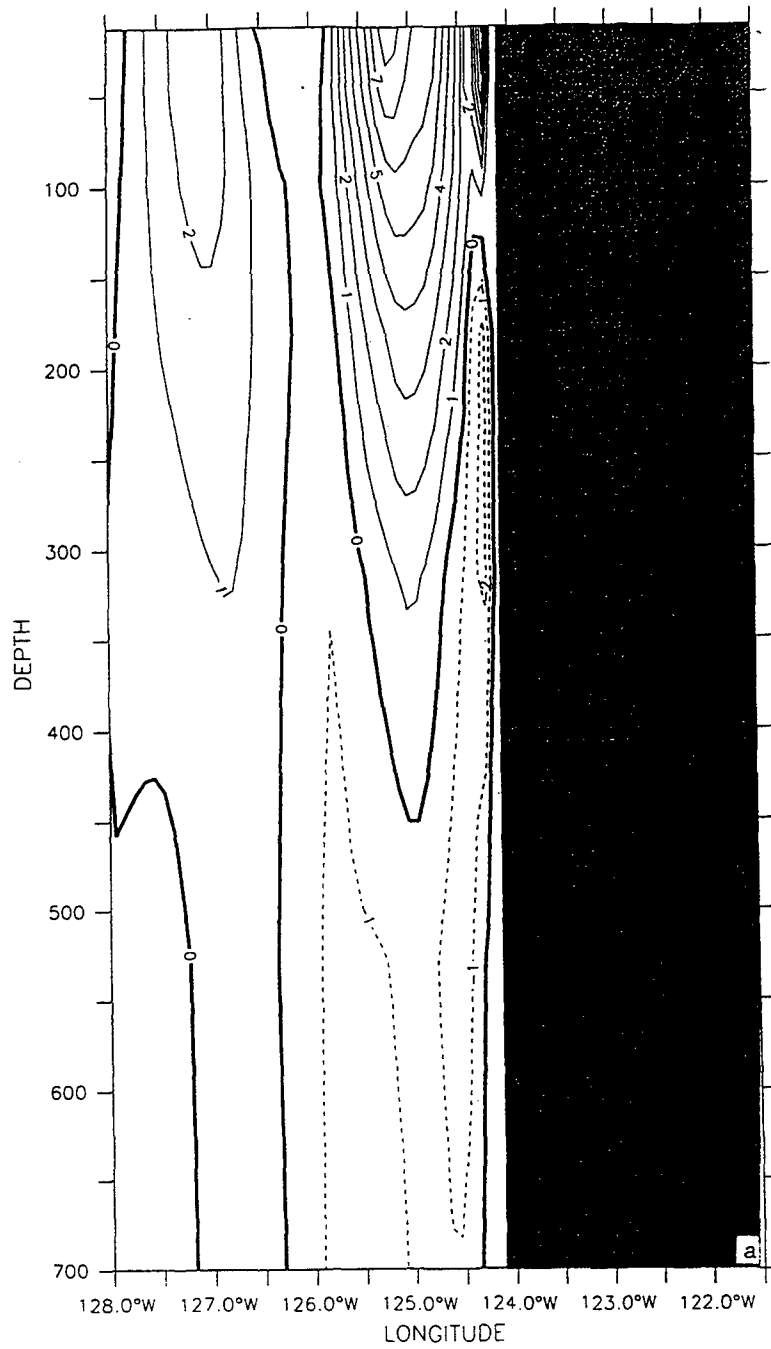
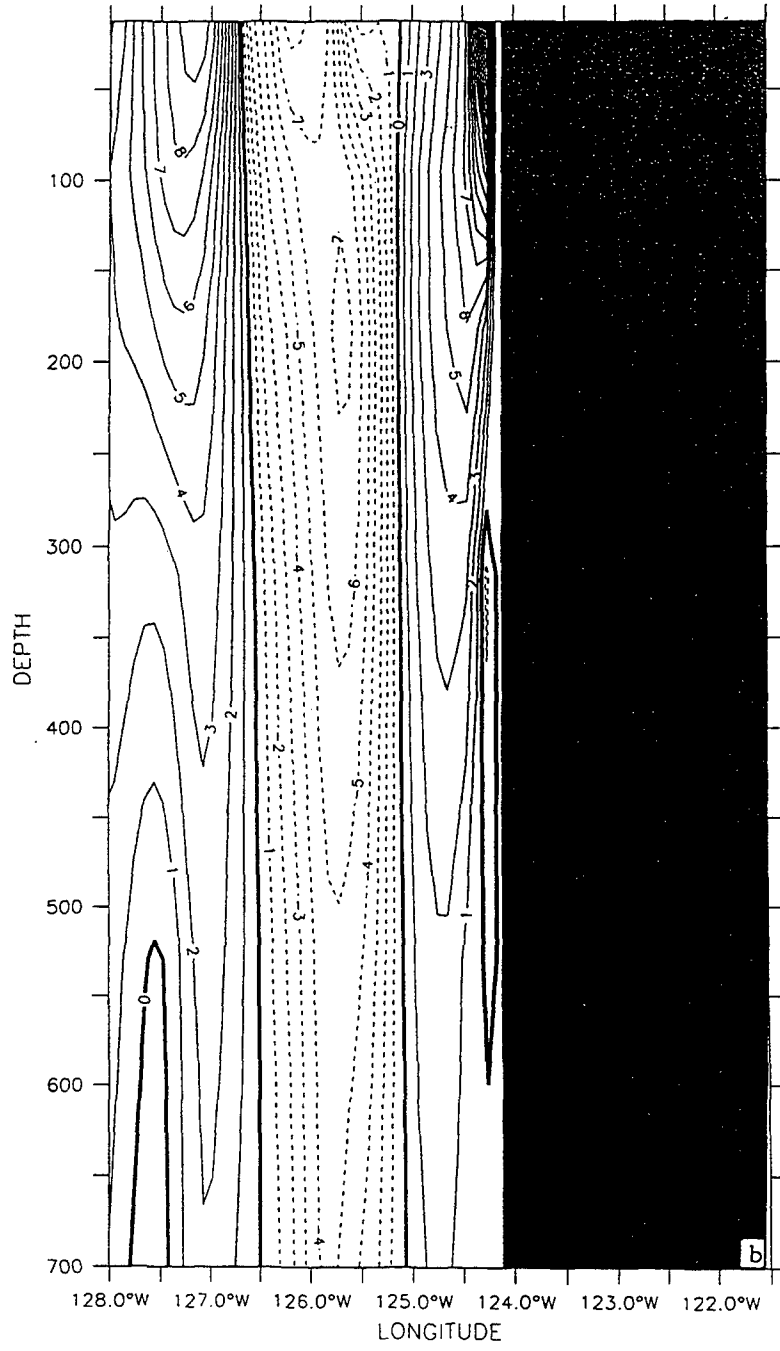


Figure 6. Cross-shore section of meridional velocity (v) at 46°N for Experiment 1 during the third year of model simulation, time-averaged for days (a) 1 - 363 and (b) 270-363. Contour interval is 1 cm/s.

LATITUDE : 46N



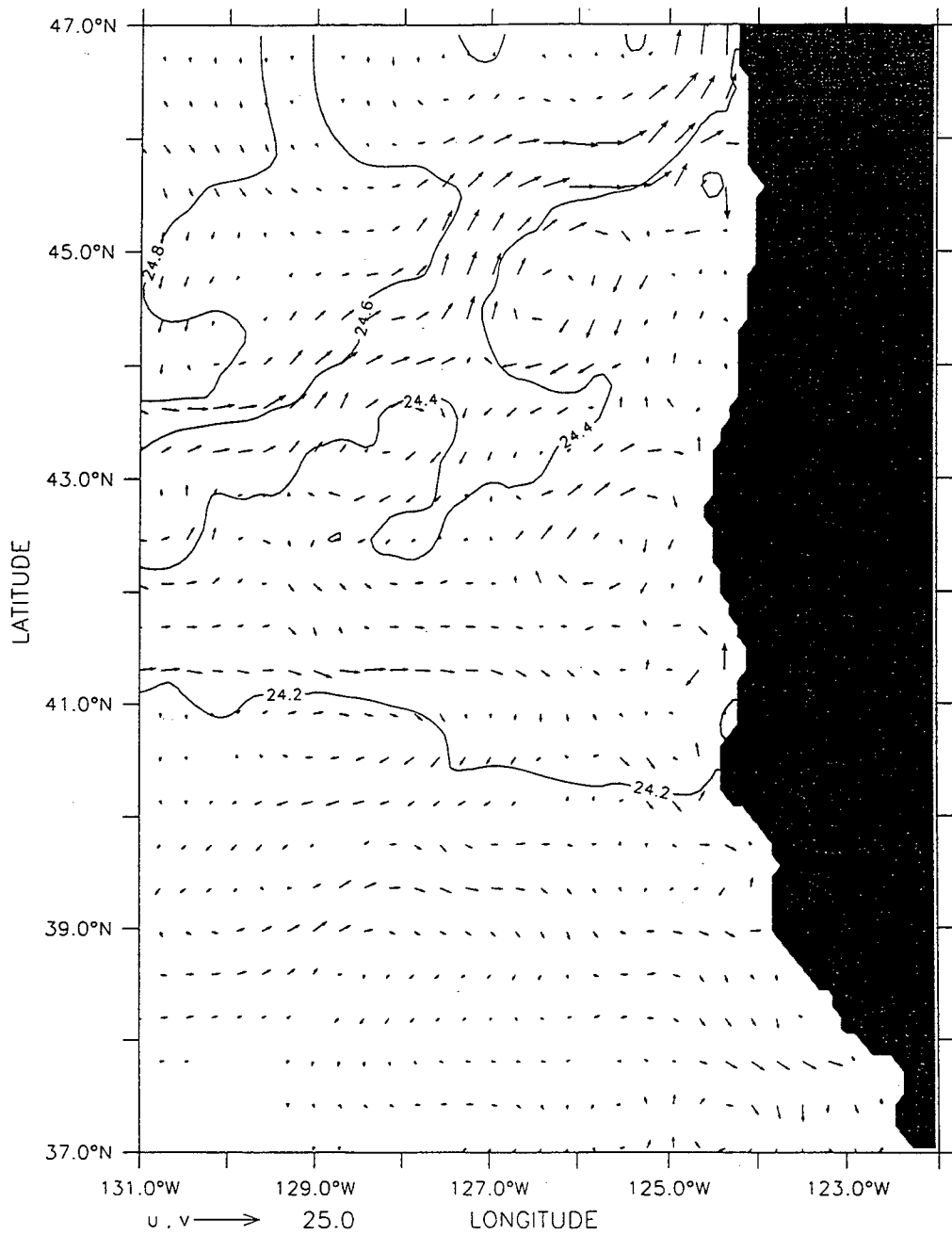


Figure 7. Density contour and velocity vectors at 46 m depth for Experiment 1, time-averaged for year 3. Contour interval is 0.2 gm/cm^3 ; maximum velocity vector is 25 cm/s.

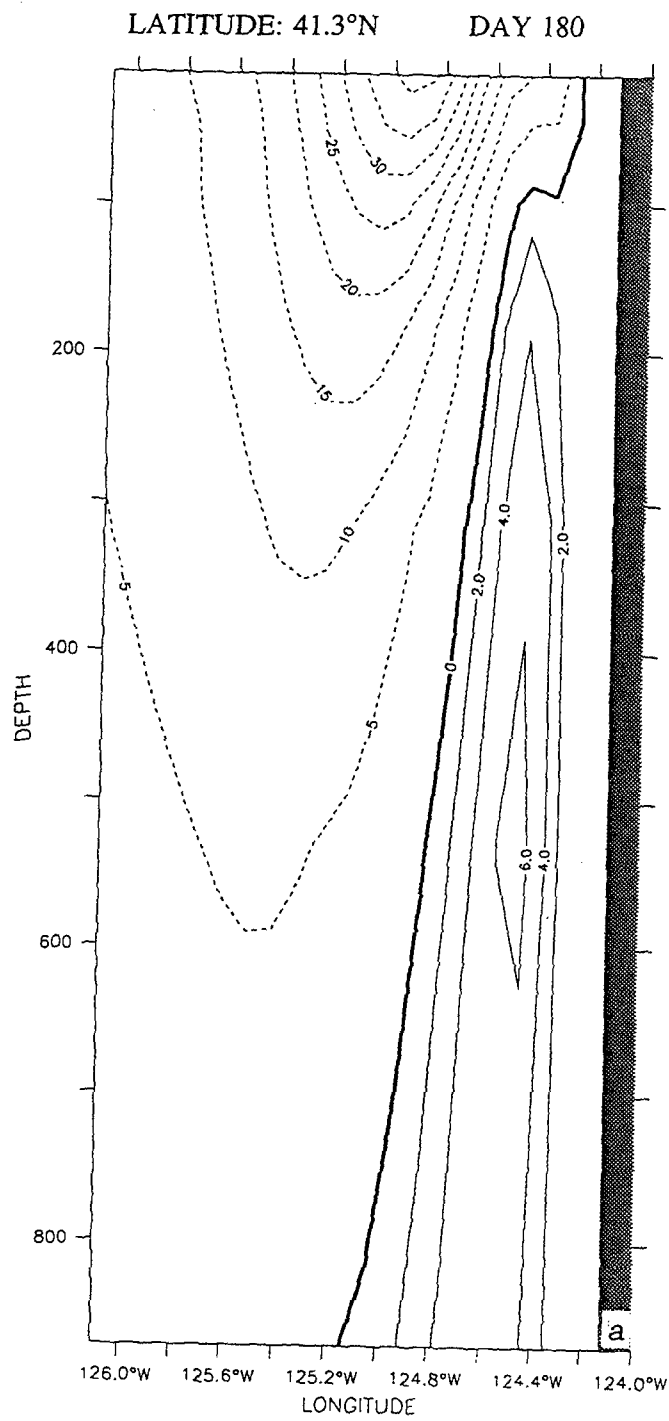
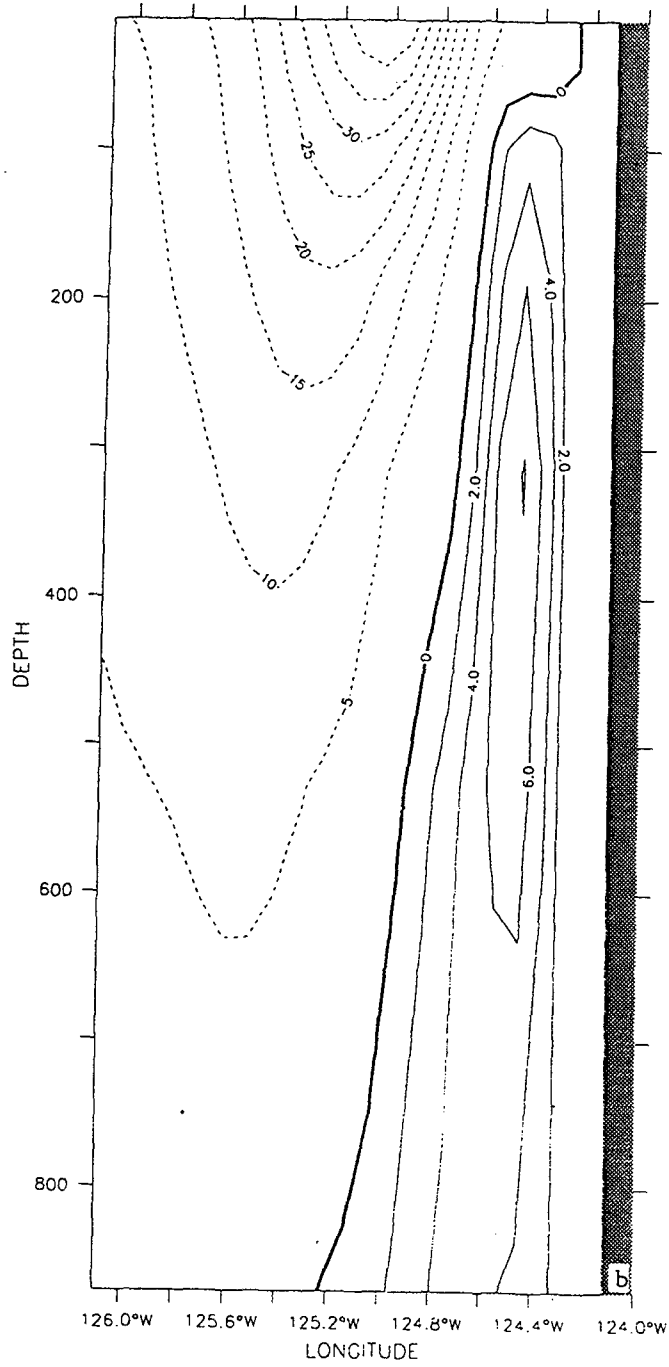


Figure 8. Cross-shore section at 41.3°N of v in the coastal region for Experiment 2 at days (a) 180 and (b) 195. Contour interval is 2 cm/s (5 cm/s) for poleward (equatorward) flow.

LATITUDE: 41.3°N

DAY 195



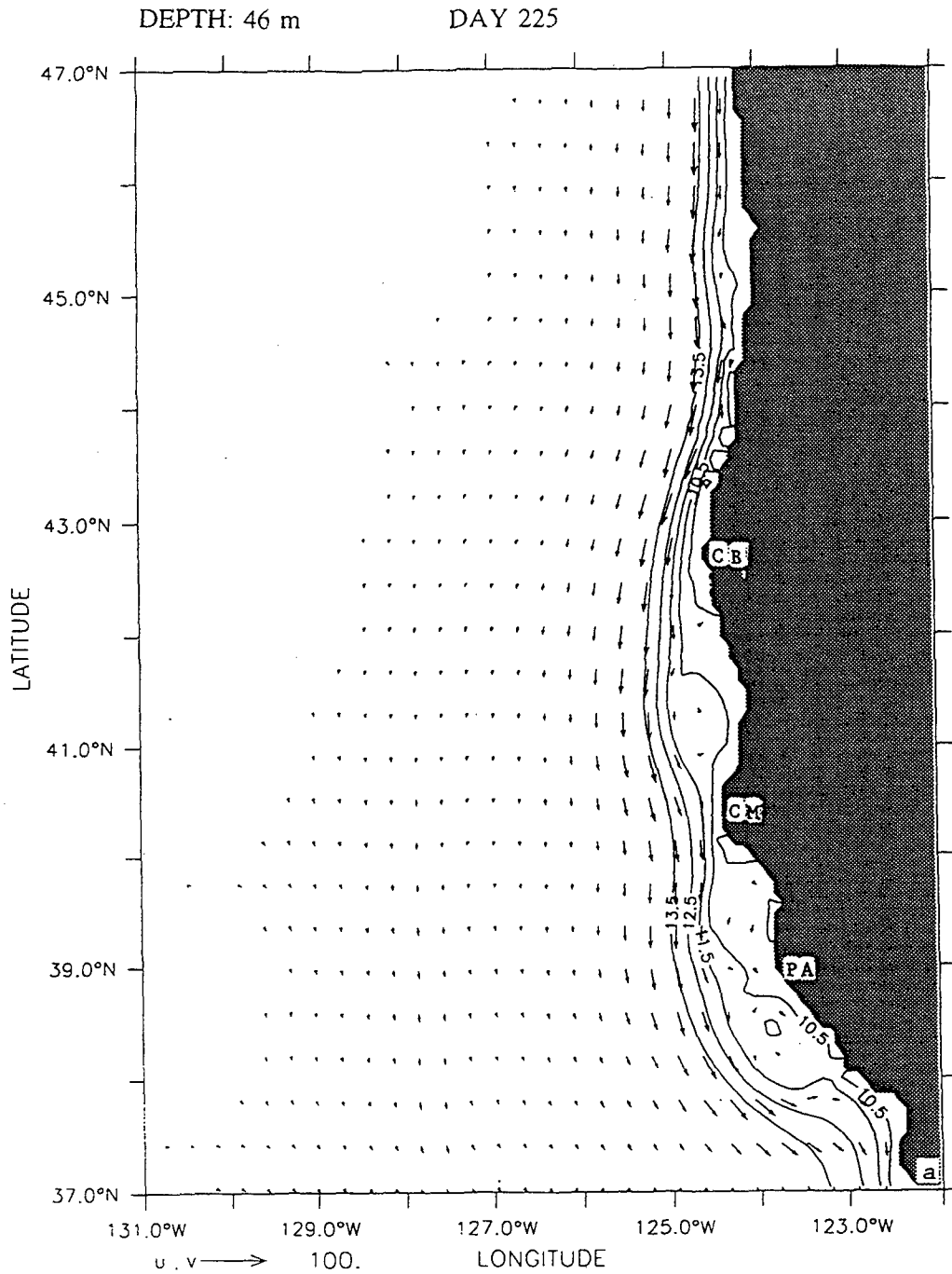
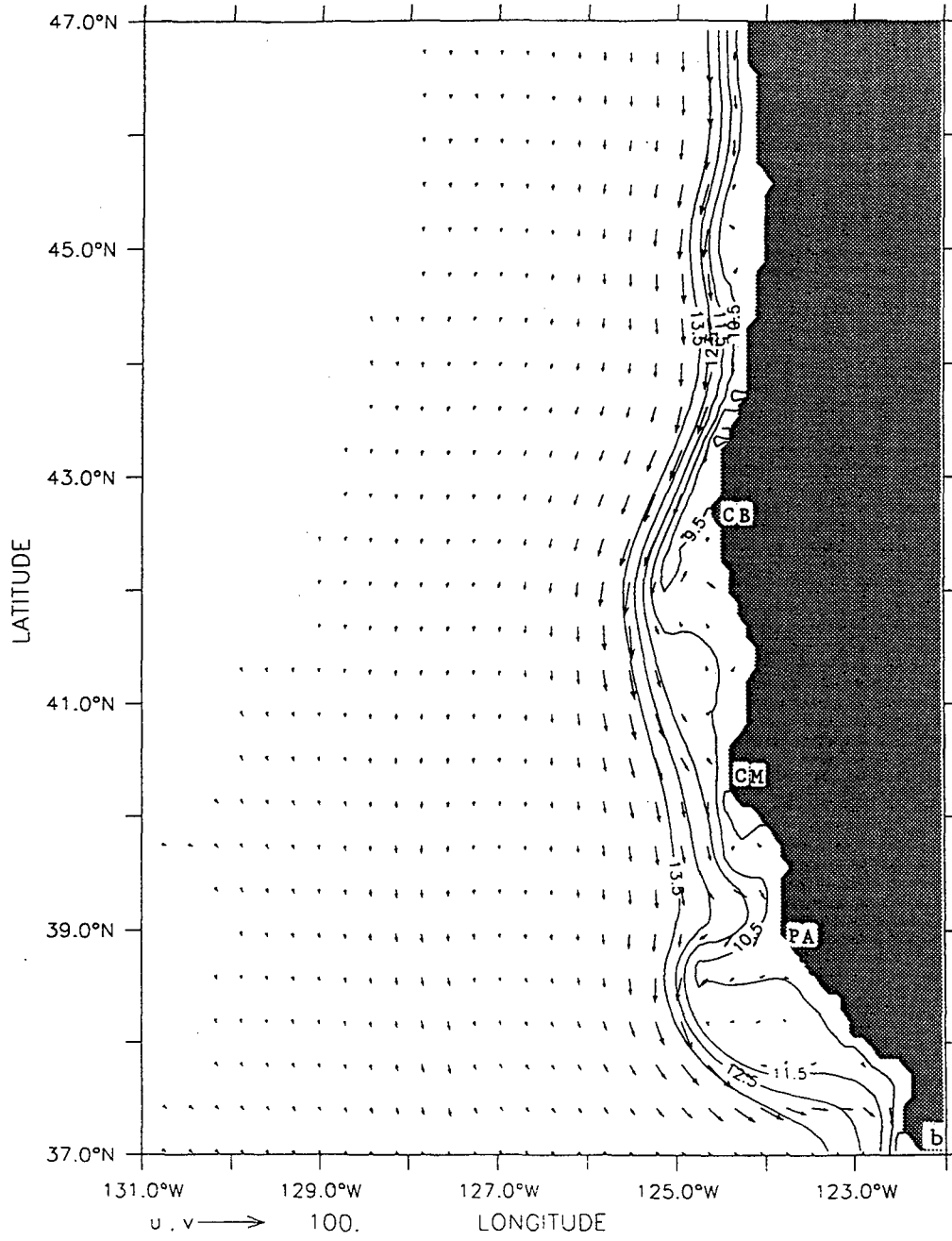


Figure 9. Temperature contours and velocity vectors at 46 m depth for Experiment 2 at days (a) 225, (b) 255, (c) 270, and (d) 315. Here and the following figures, CB refers to Cape Blanco, CM to Cape Mendocino, and PA to Point Arena. Contour interval is 1°C; maximum velocity vector is 100 cm/s.

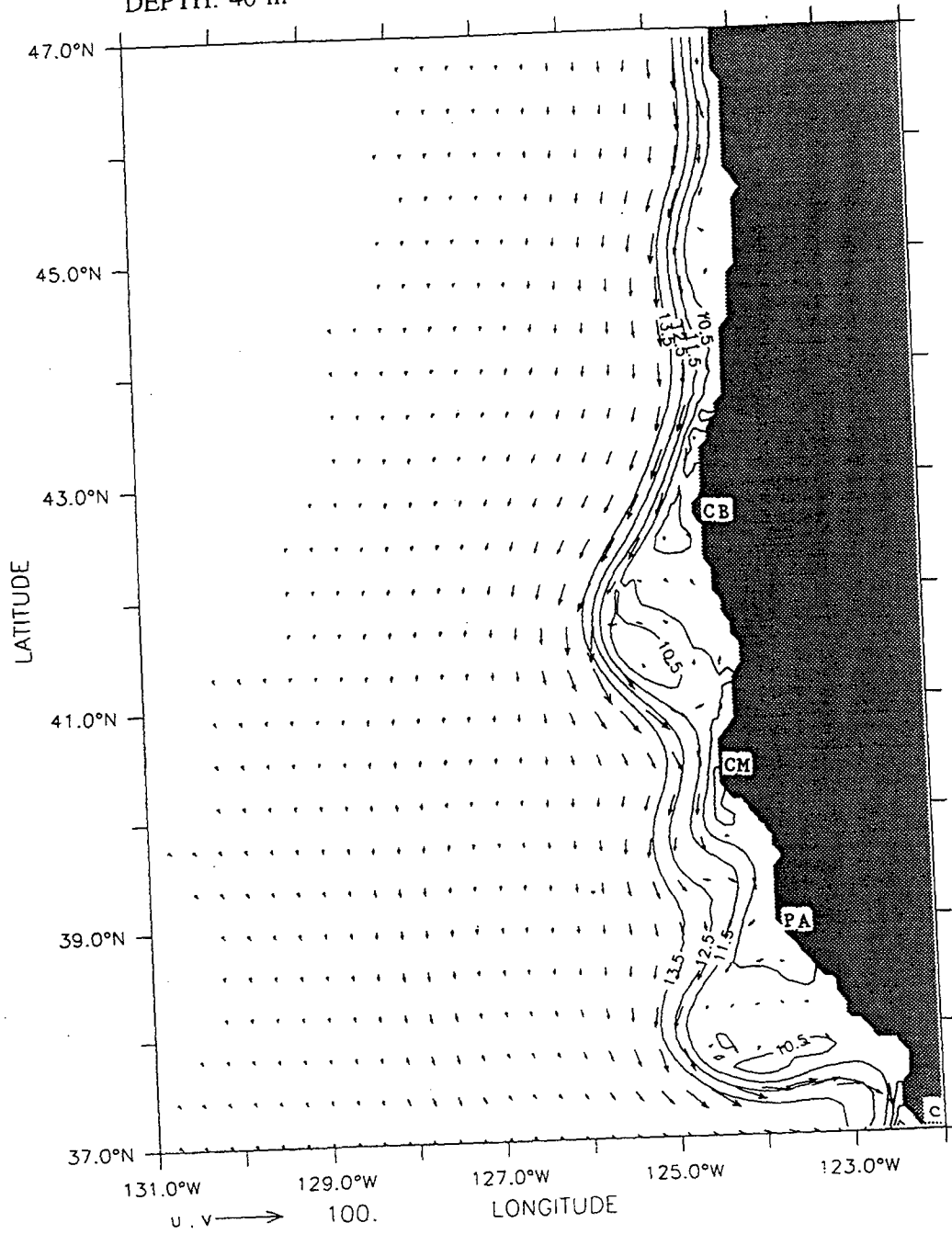
DEPTH: 46 m

DAY 255



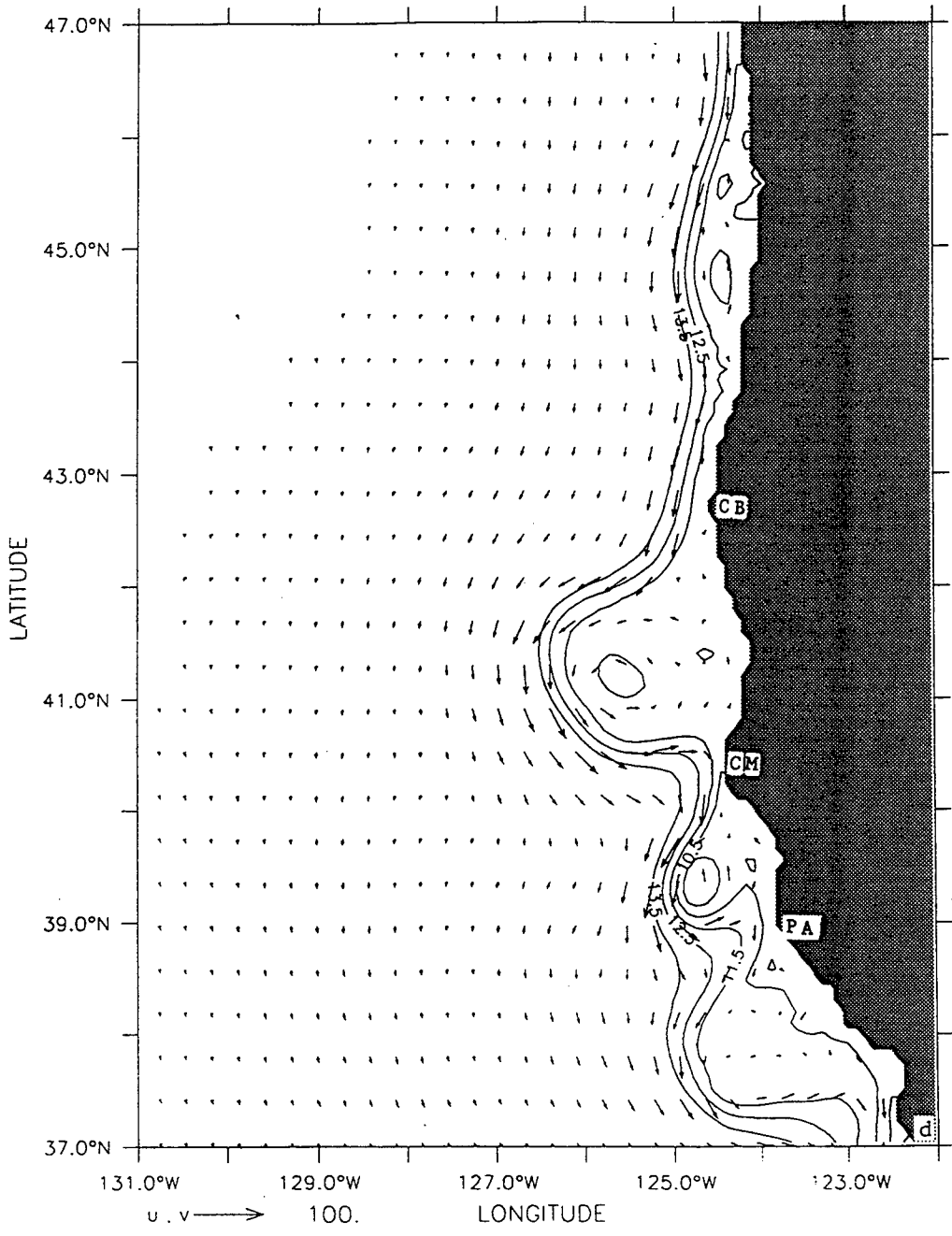
DEPTH: 46 m

DAY 270



DEPTH: 46 m

DAY 315



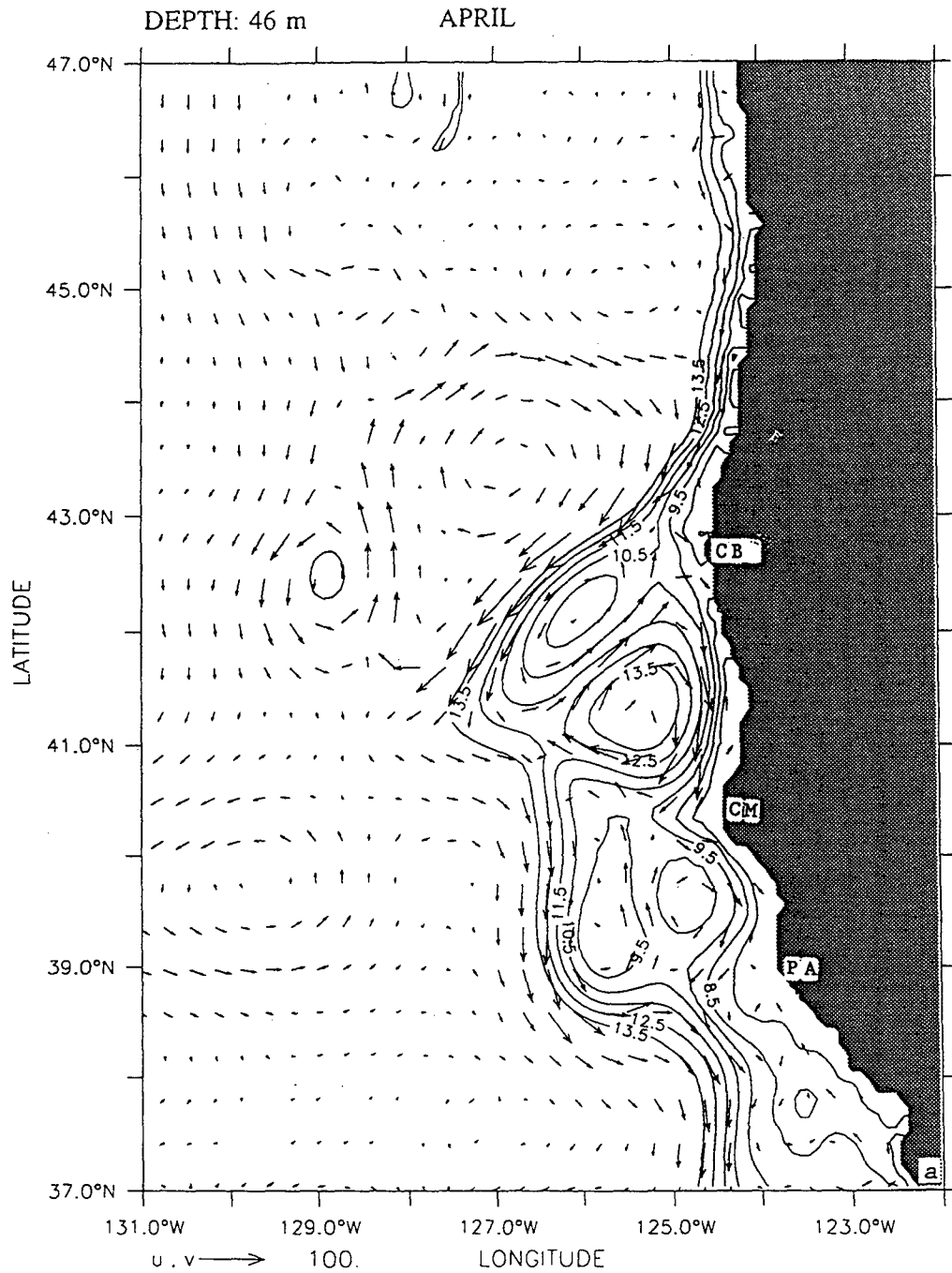
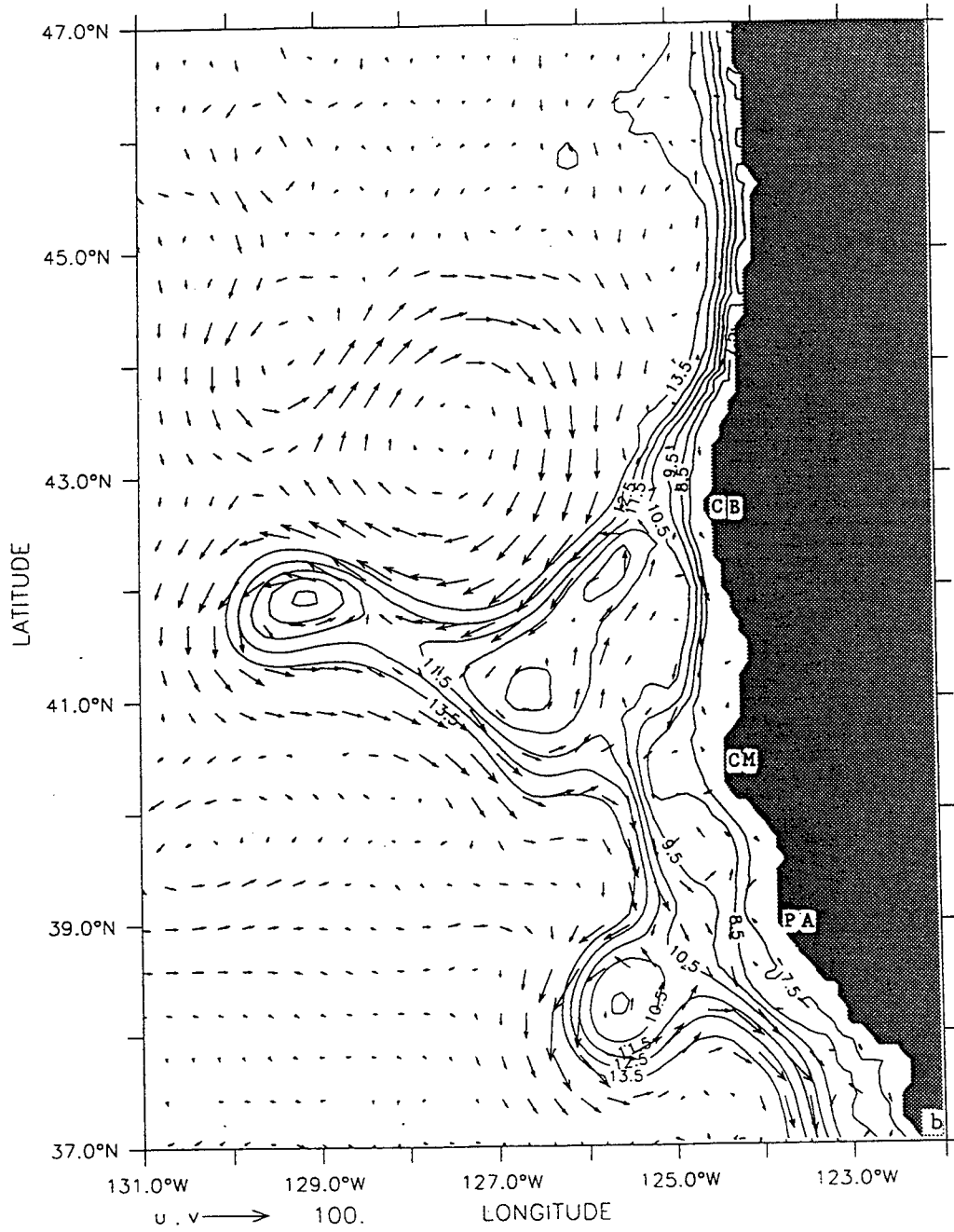


Figure 10. Temperature and velocity vectors at 46 m depth for Experiment 2 in the third year of model simulation, time-averaged over the months of (a) April, (b) July, (c) October, and (d) December. Contour interval is 1°C; maximum velocity vector is 100 cm/s.

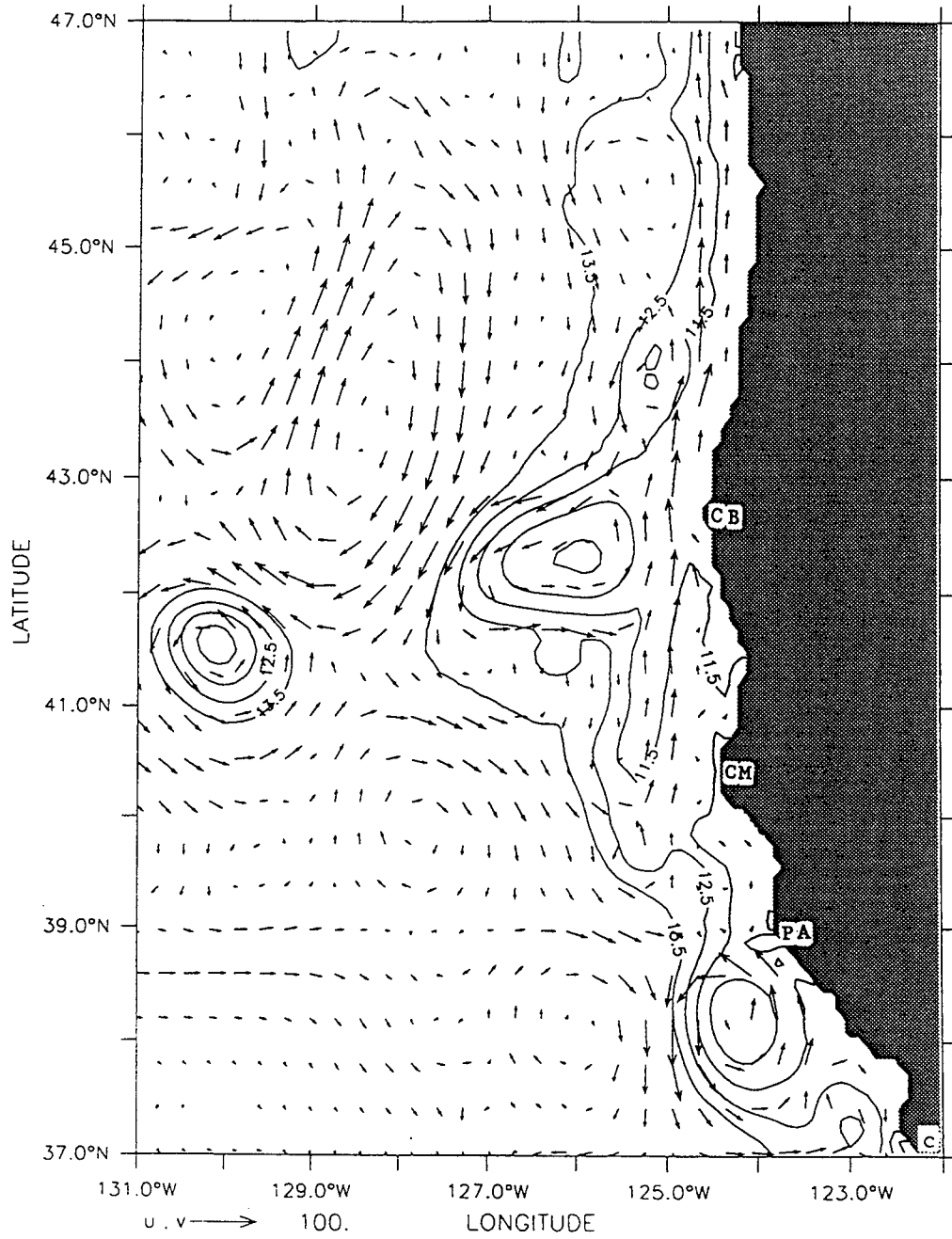
DEPTH: 46 m

JULY



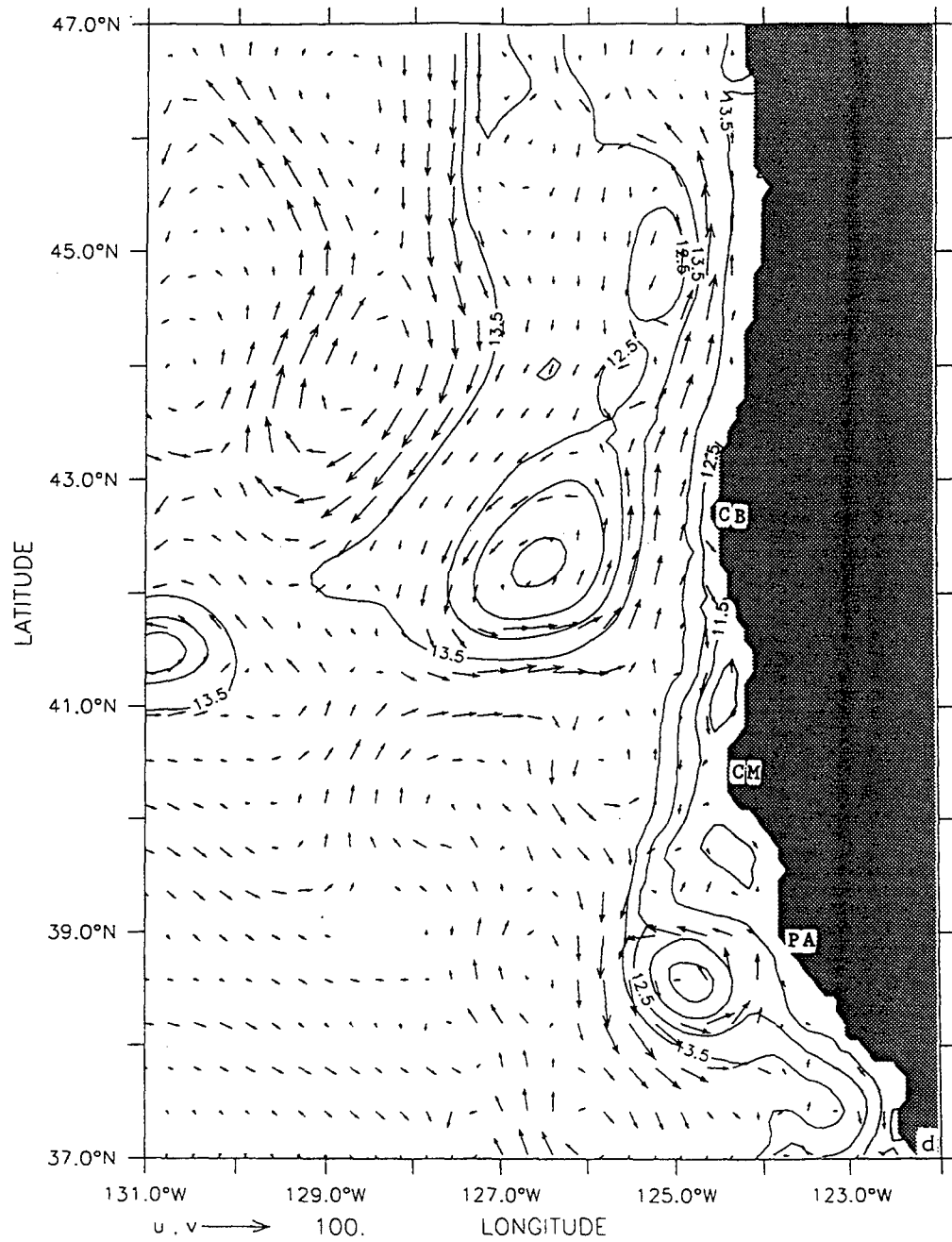
DEPTH: 46 m

OCTOBER



DEPTH: 46 m

DECEMBER



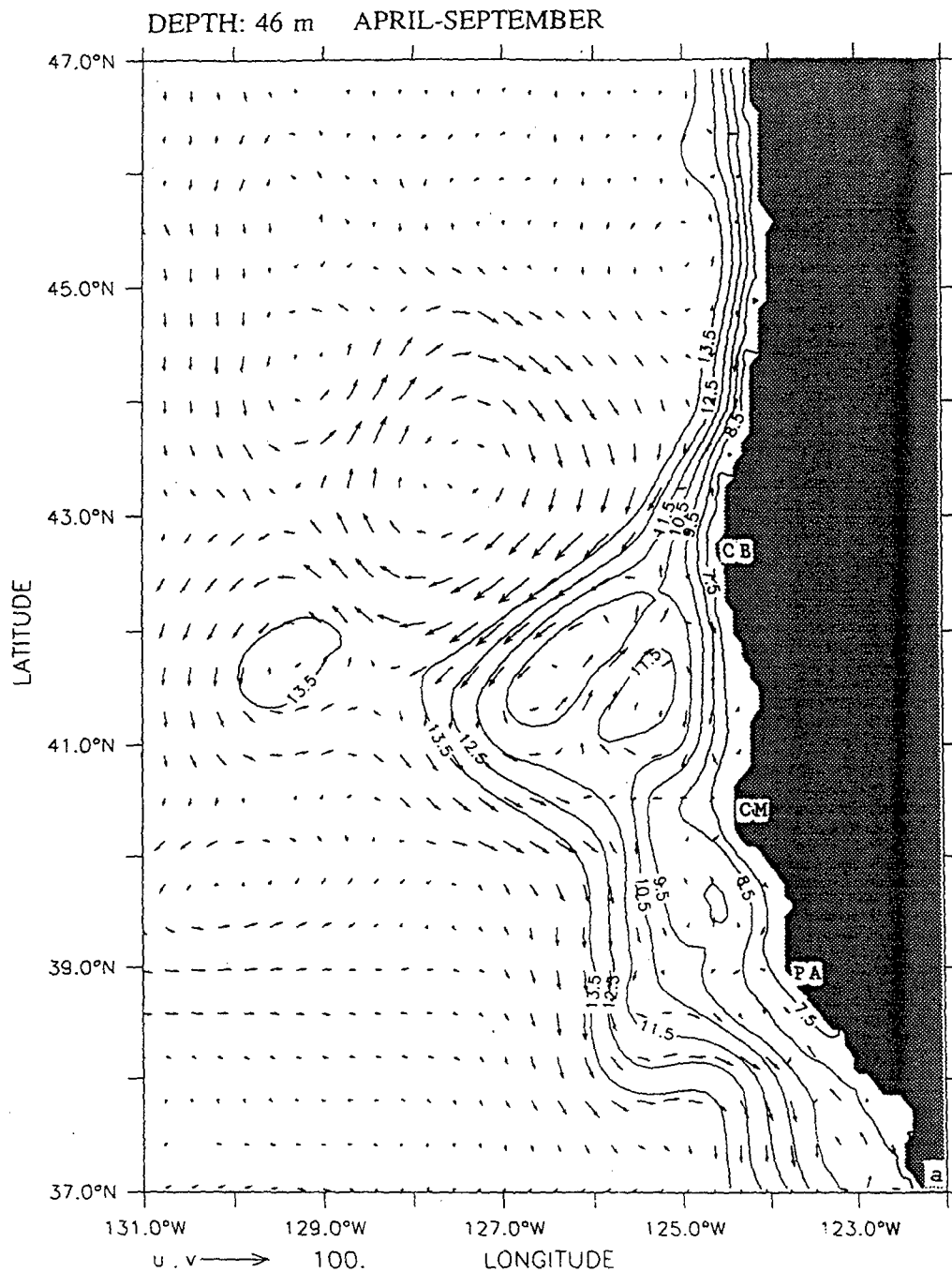
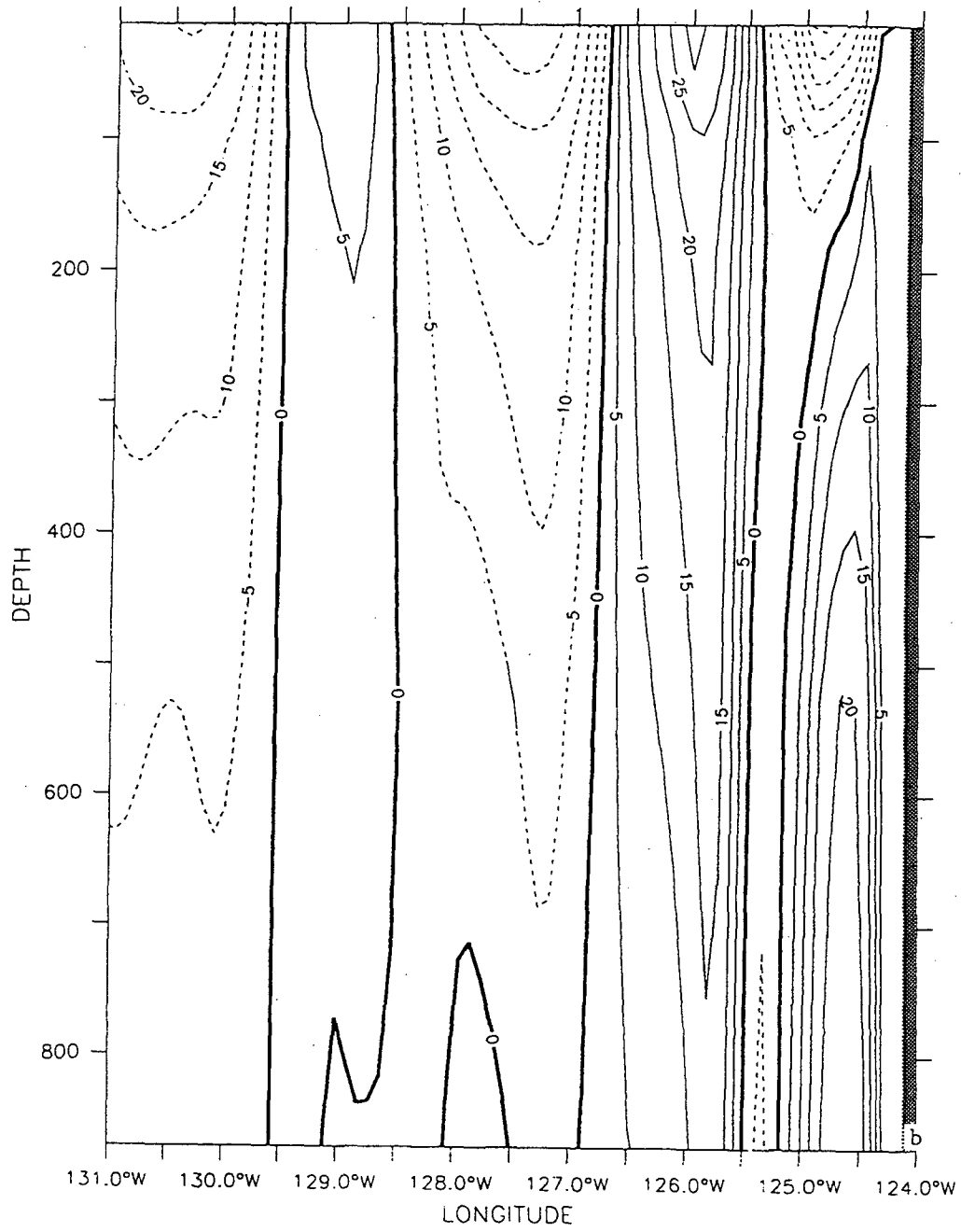
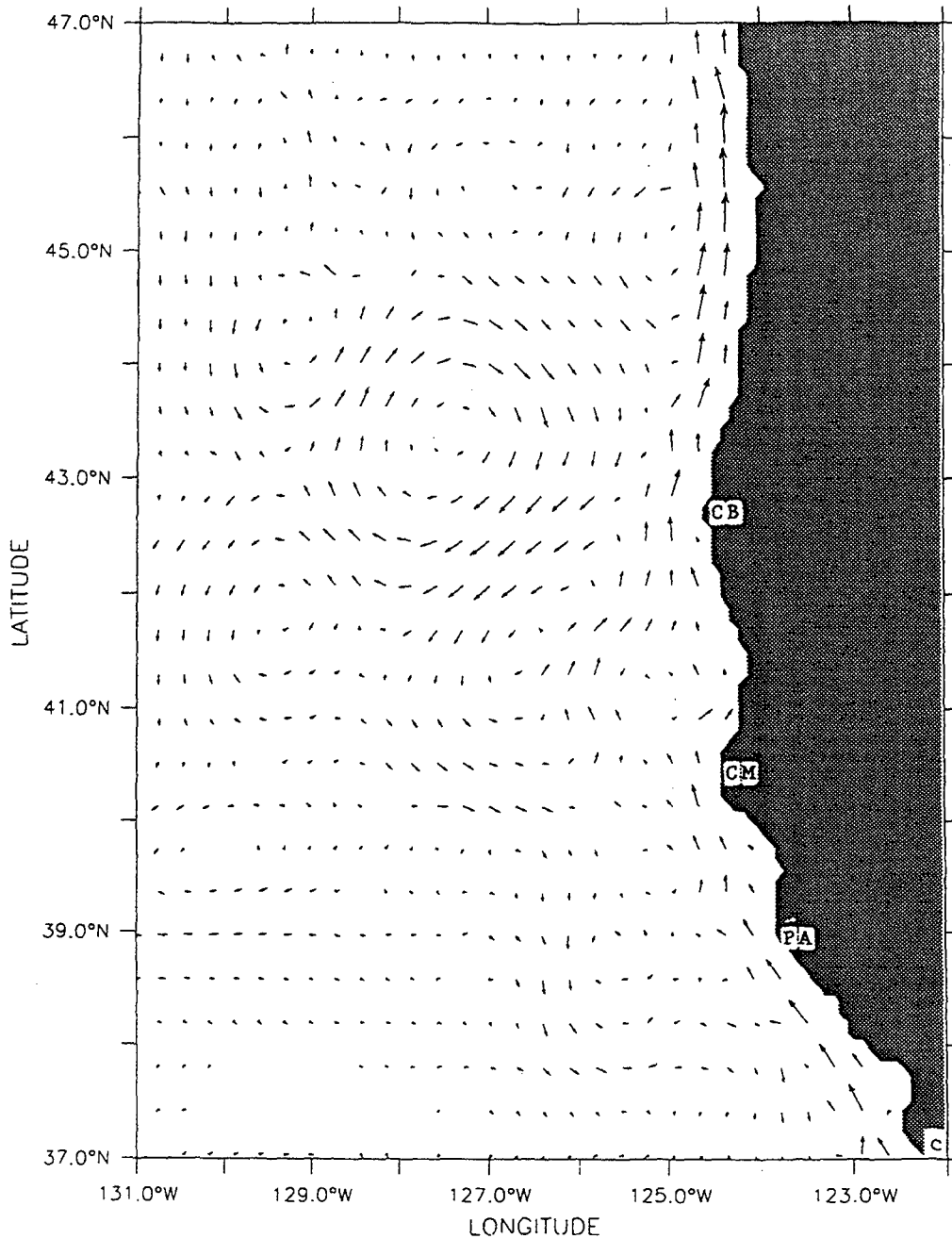


Figure 11. Time-averaged plots for the upwelling season for Experiment 2 of (a) temperature contours and velocity vectors at 46 m depth, (b) cross-section of v at 41.3°N , and (c) velocity vectors at 316 m depth. Contour interval is 1°C in Figure 11a and 5 cm/s in Figure 11b. Maximum velocity vector is 100 cm/s in Figure 11a and 80 cm/s in Figure 11c.

LATITUDE: 41.3°N APRIL-SEPTEMBER



DEPTH: 316 m APRIL-SEPTEMBER



DEPTH : 46m
T (DAY) : 45

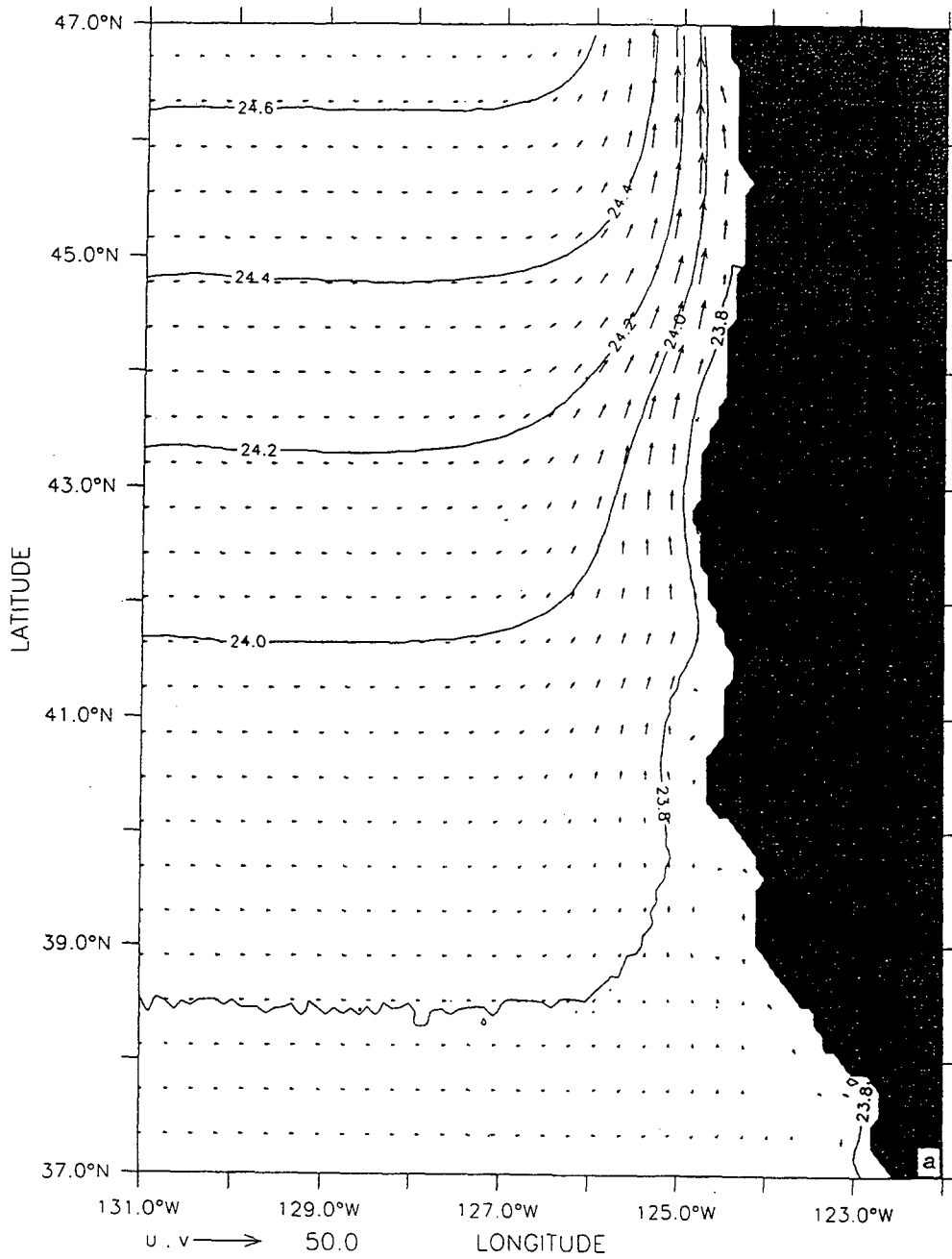
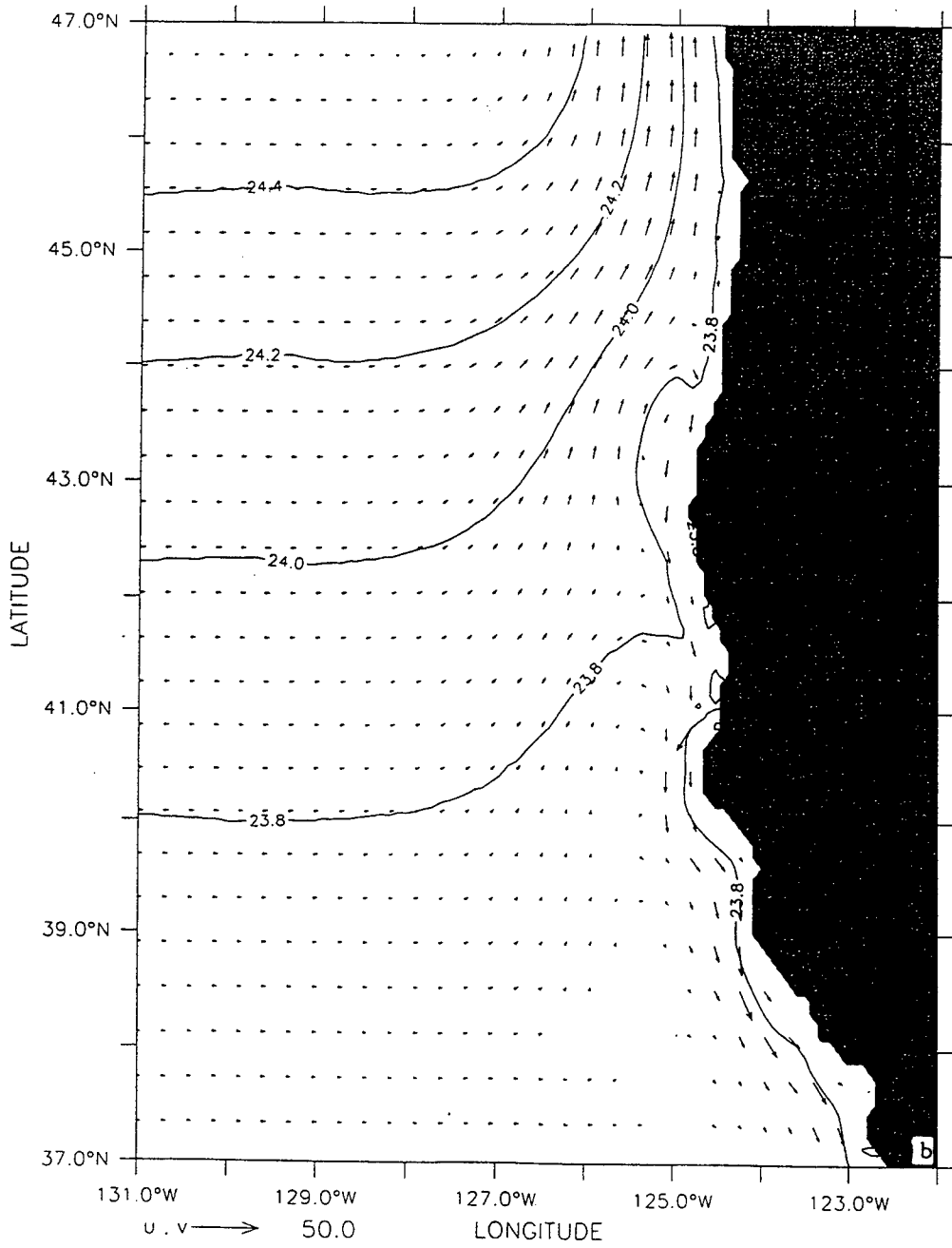
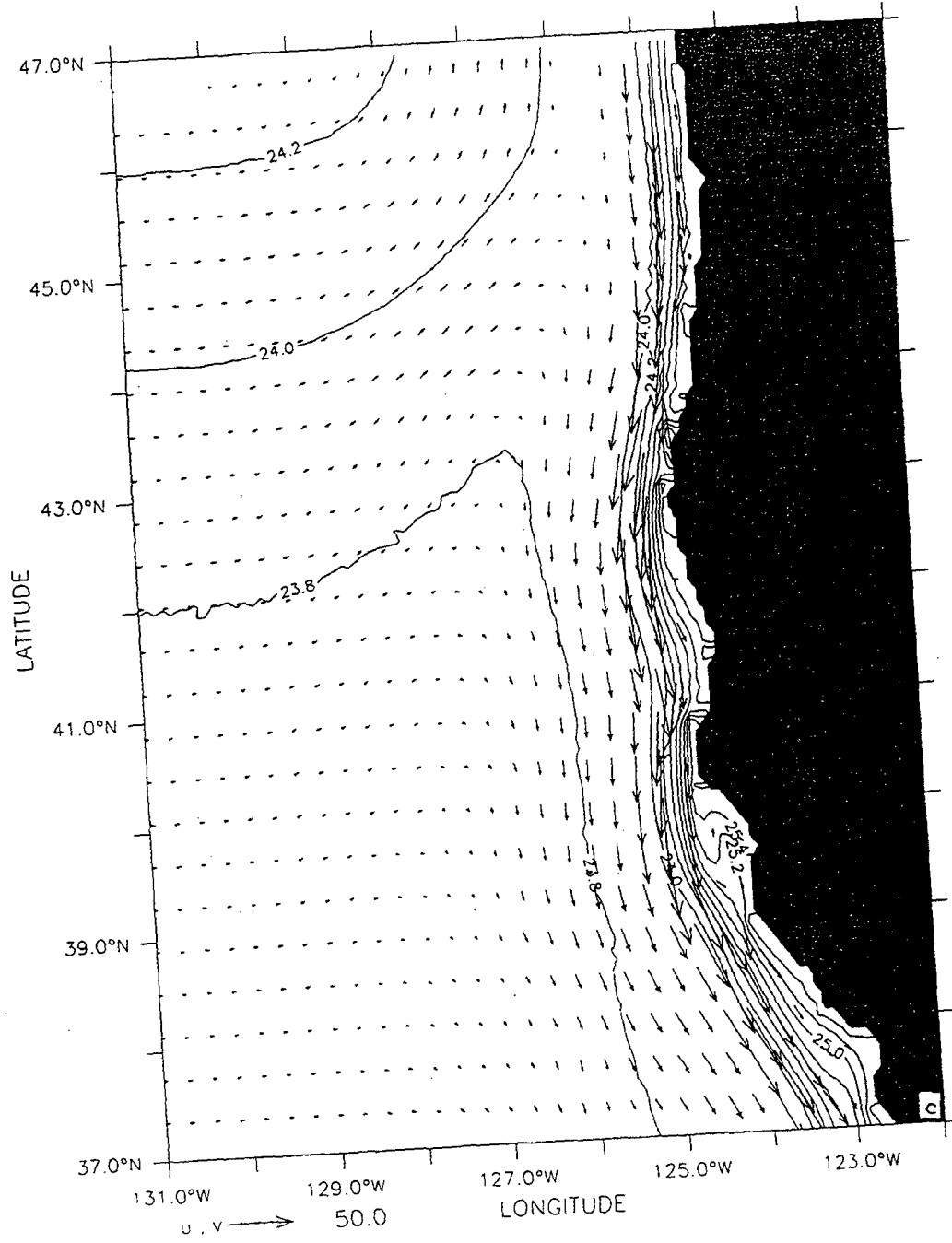


Figure 12. Density contours and velocity vectors at 46 m depth for Experiment 3 at days (a) 45, (b) 87, (c) 180, and (d) 255. Contour interval is 0.2 gm/cm^3 ; maximum velocity vector is 50 cm/s.

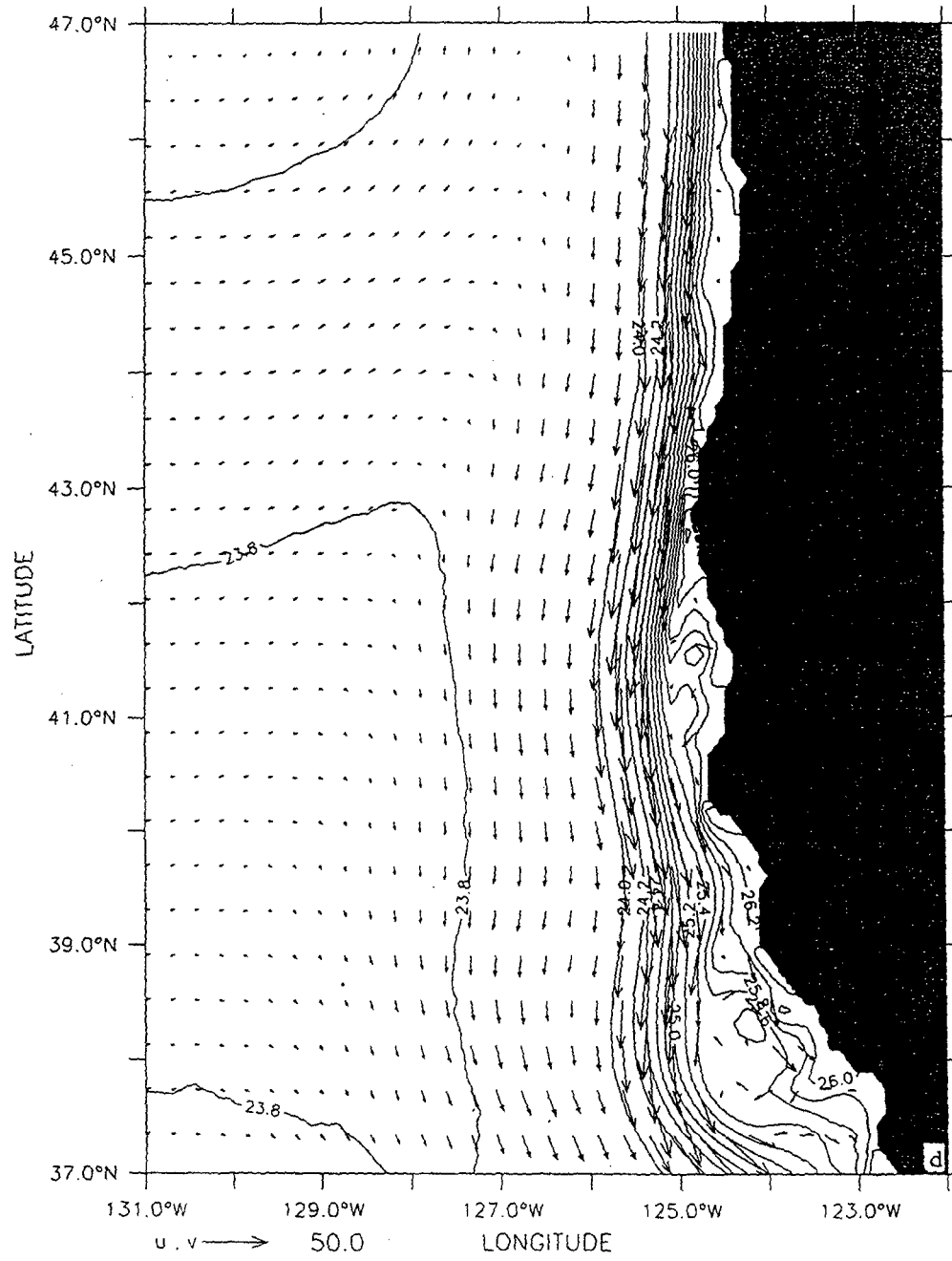
DEPTH : 46m
T (DAY) : 87



DEPTH : 46m
T (DAY) : 180



DEPTH : 46m
T (DAY) : 255



LATITUDE : 39N
T (DAY) : 180

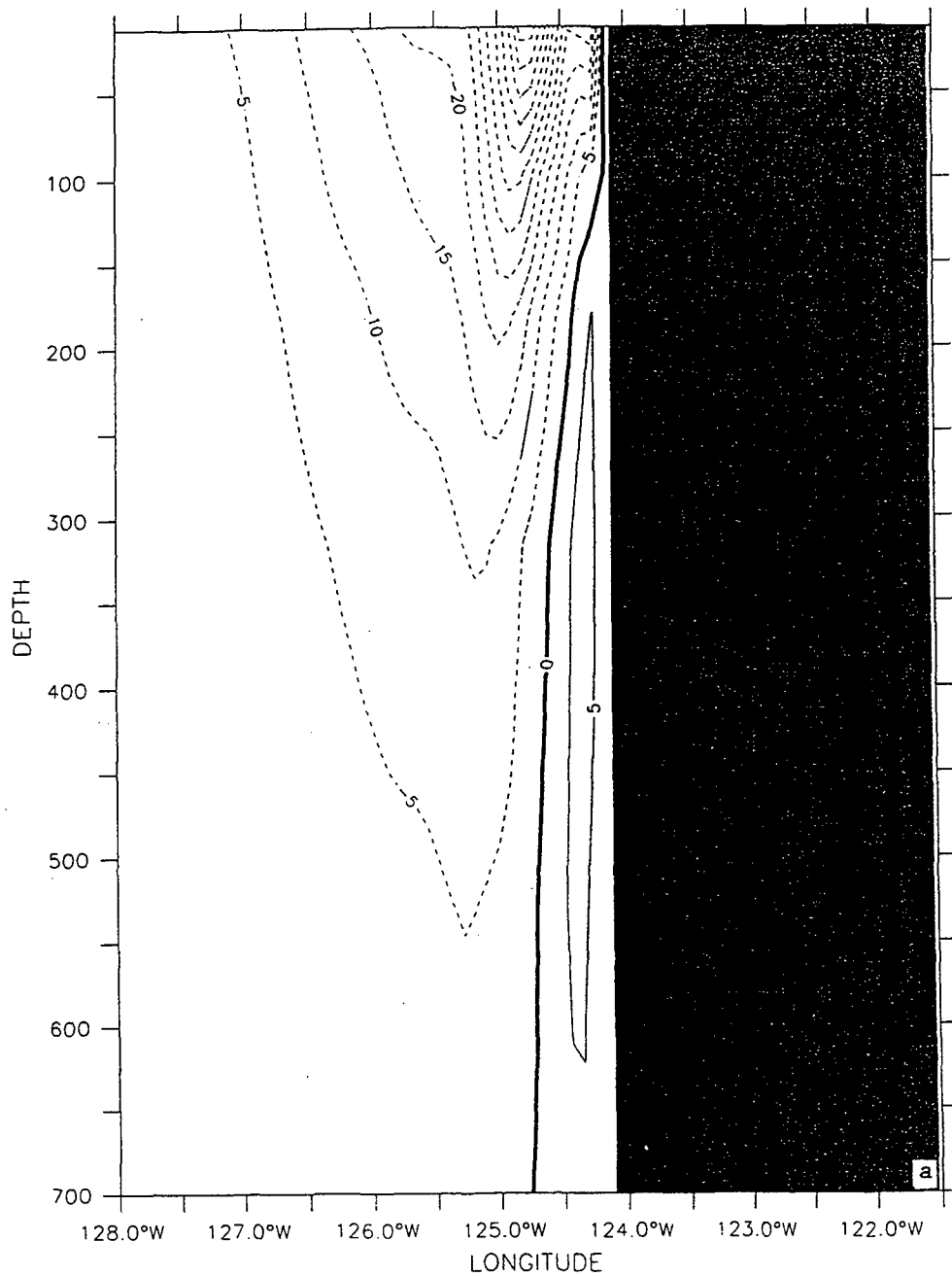
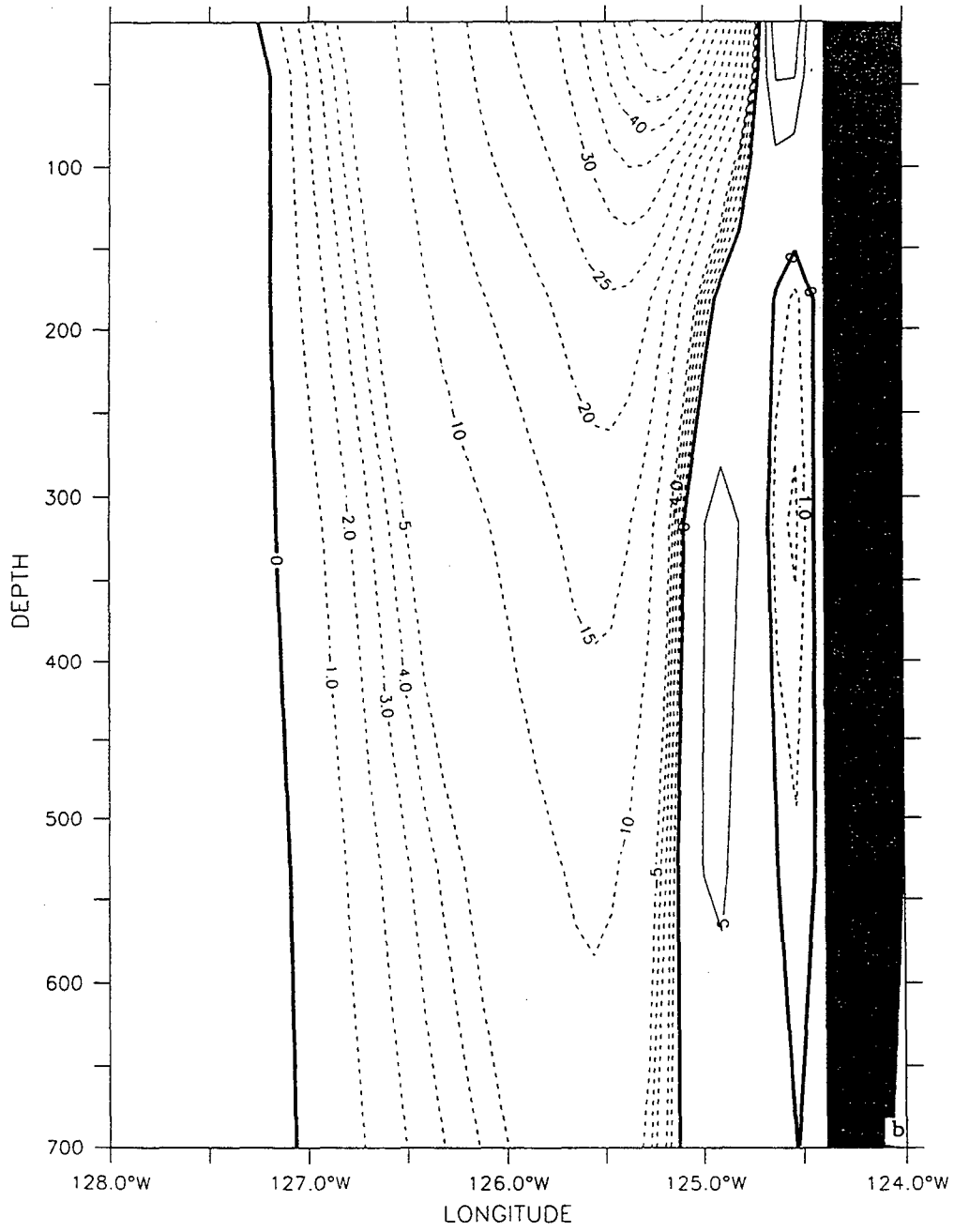


Figure 13. Cross-shore of v in the coastal region for Experiment 3, days (a) 180 at 39°N and (b) 300 at 46°N. To avoid clutter, only velocities up to 10 cm/s are plotted for Figure 13b. Contour interval is 5 cm/s for Figure 13a and 1 cm/s for Figure 13b.

LATITUDE : 46N
T (DAY) : 300



DEPTH : 46m

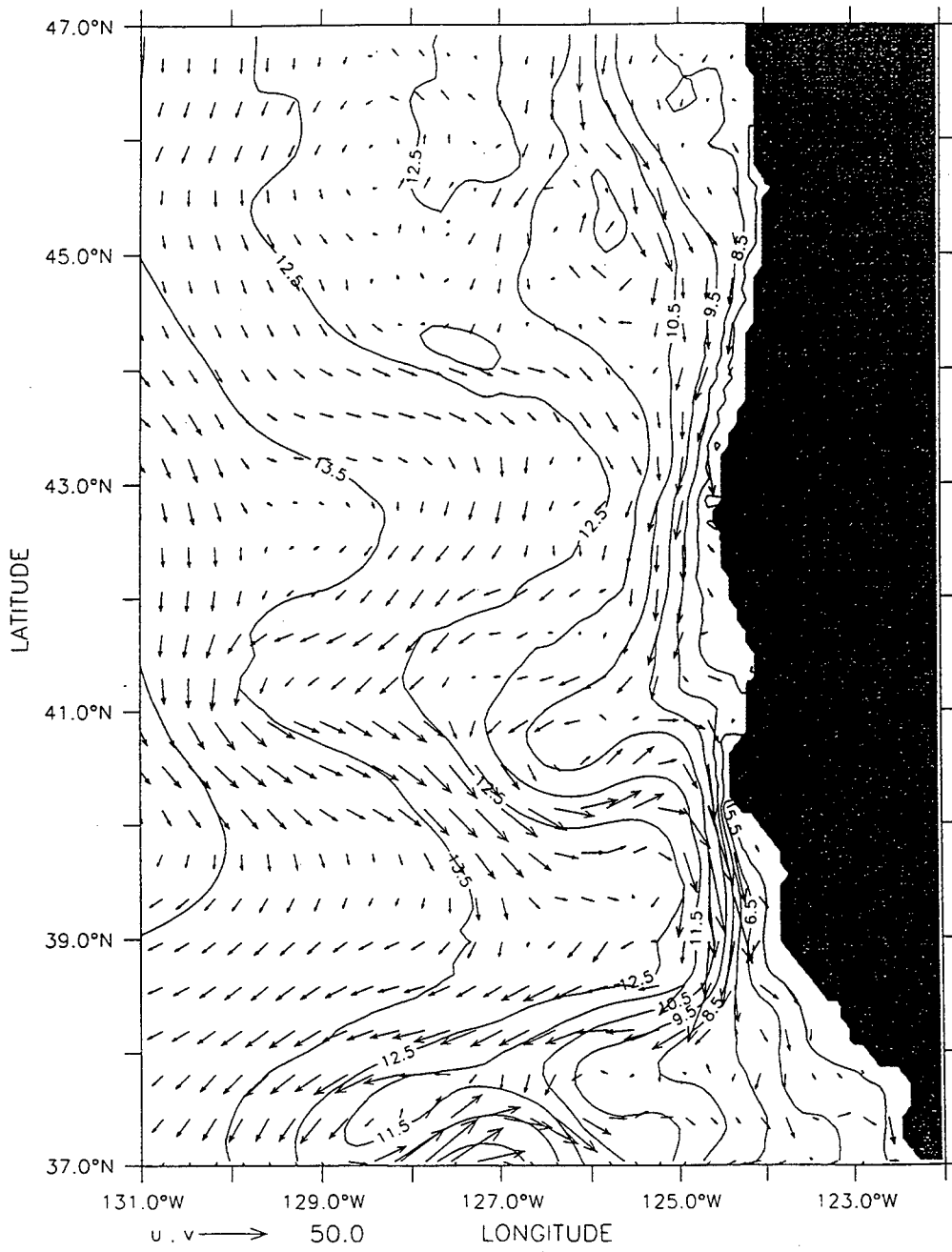


Figure 14. Temperature contours and velocity vectors at 46 m depth for Experiment 3 in the third year of model simulation for days 90-270. Contour interval is 1.0°C; maximum velocity vector is 50 cm/s.

LATITUDE : 41N

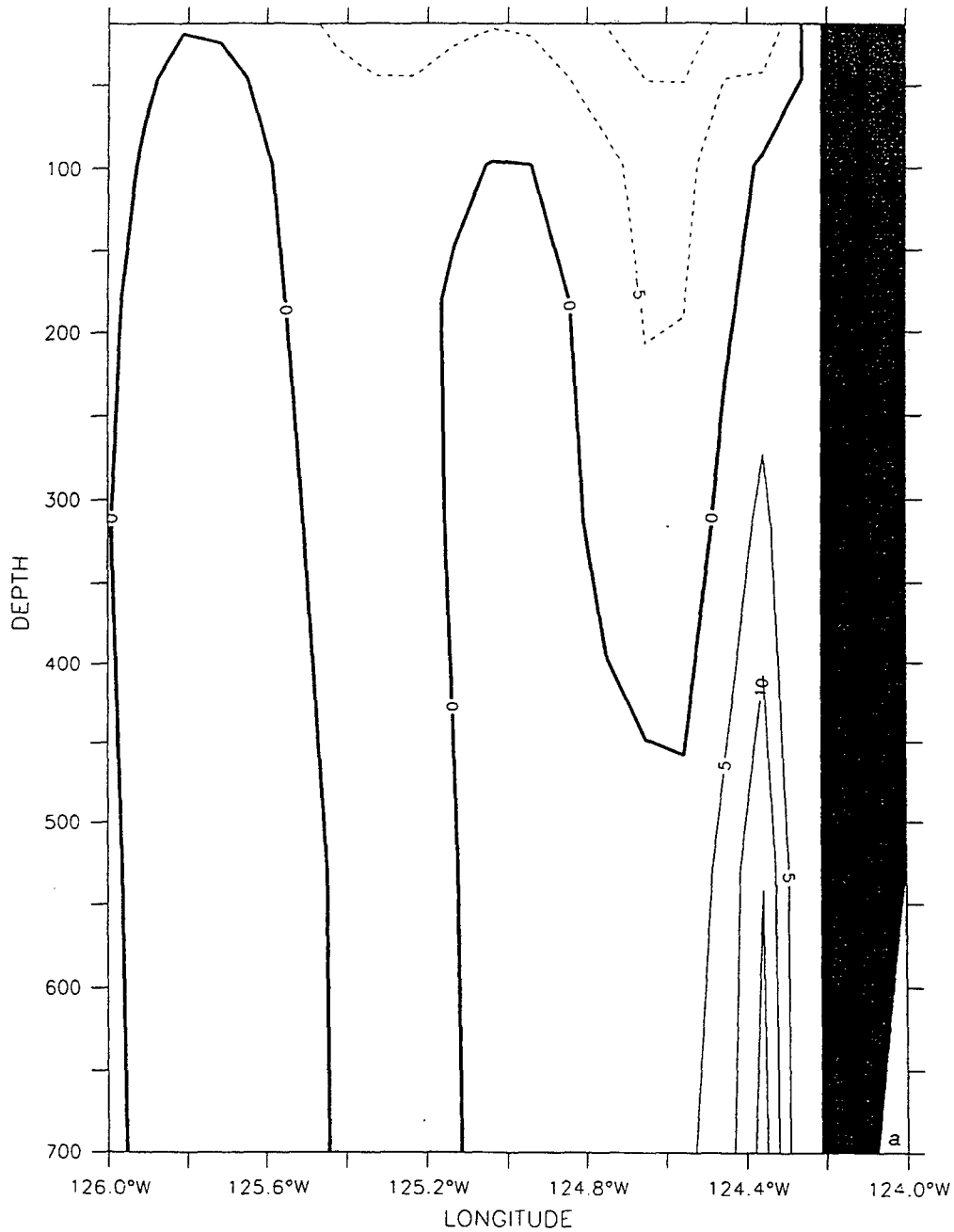
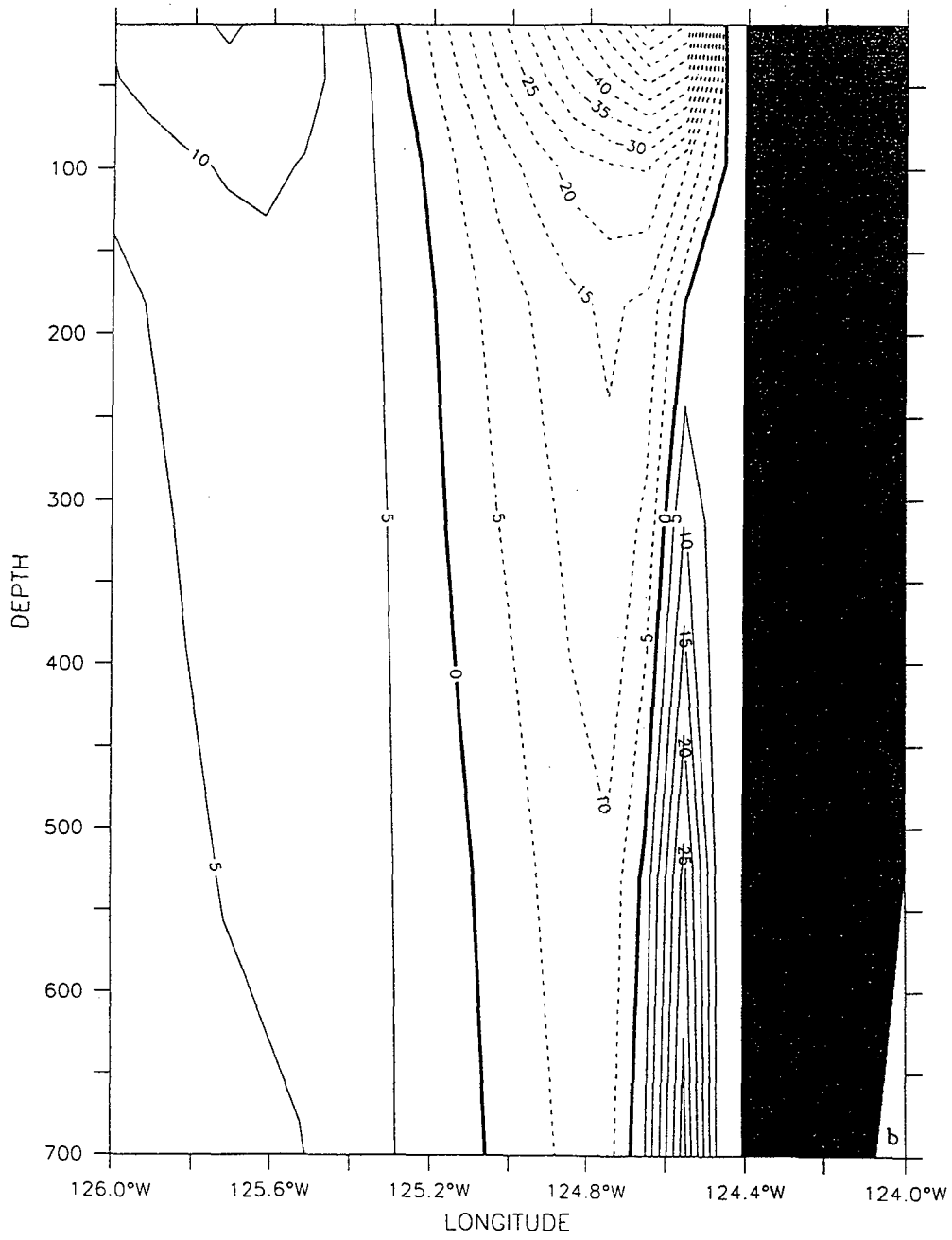


Figure 15. Cross-shore sections for Experiment 3 in the third year of model simulation, time-averaged for days 90-270 at (a) 41°N and (b) 40.2°N. Contour interval is 5°C.

LATITUDE : 40.2N



DEPTH : 13m

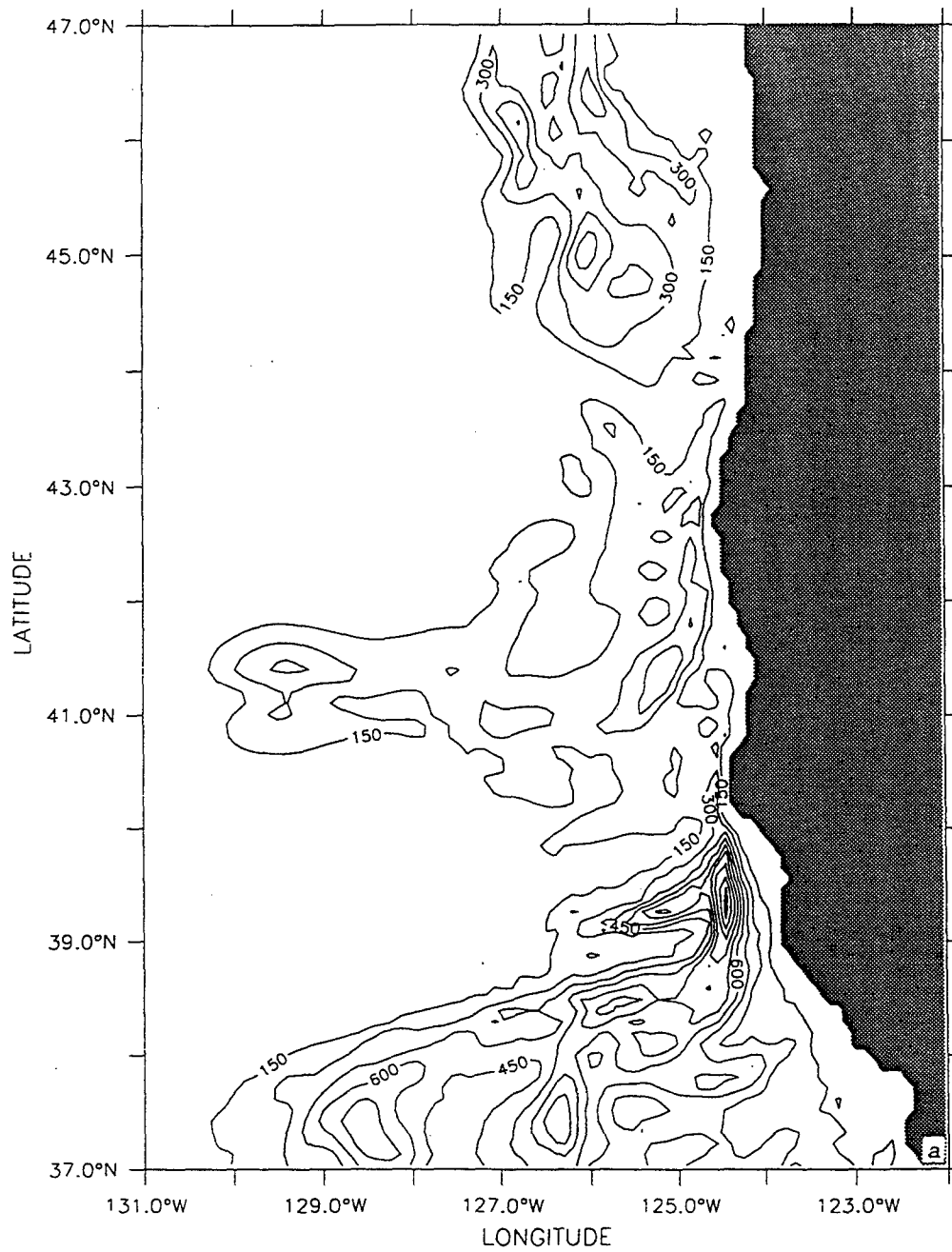
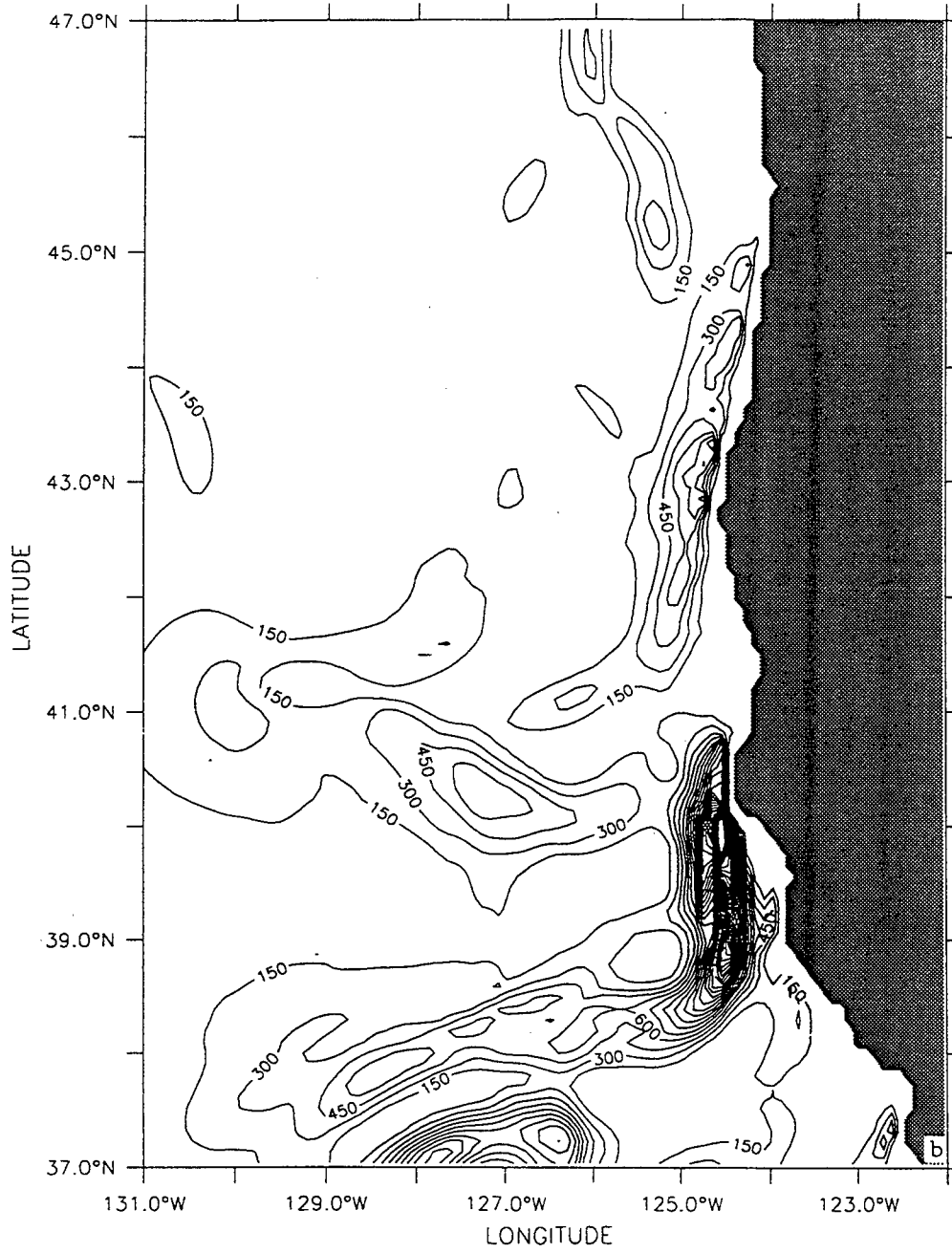


Figure 16. Horizontal maps at 13 m depth of (a) mean kinetic energy (MKE), and (b) eddy kinetic energy (EKE) for Experiment 3 in the third year of model simulation, time-averaged for days 90-270.

DEPTH : 13m



LATITUDE : 37N

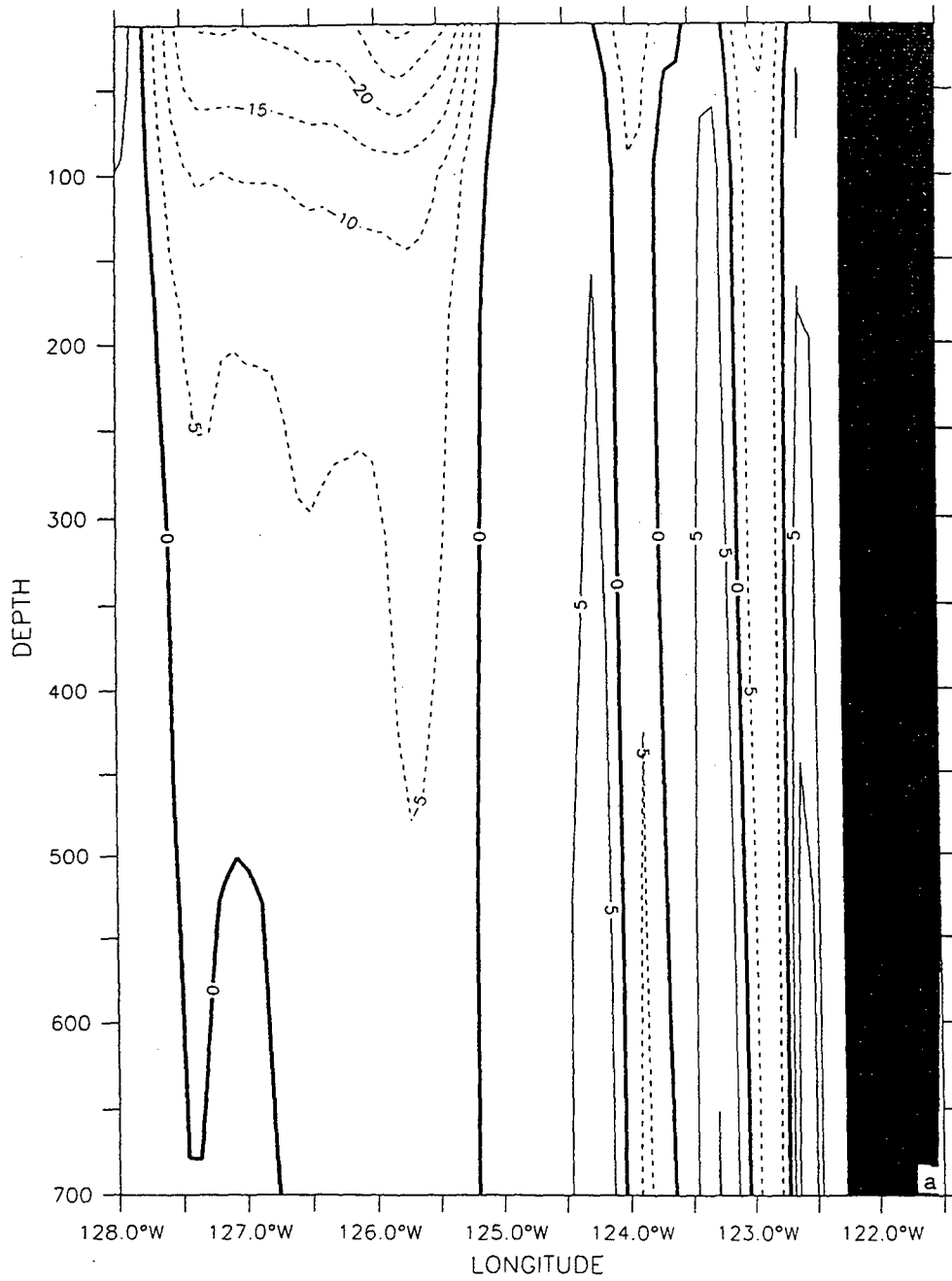
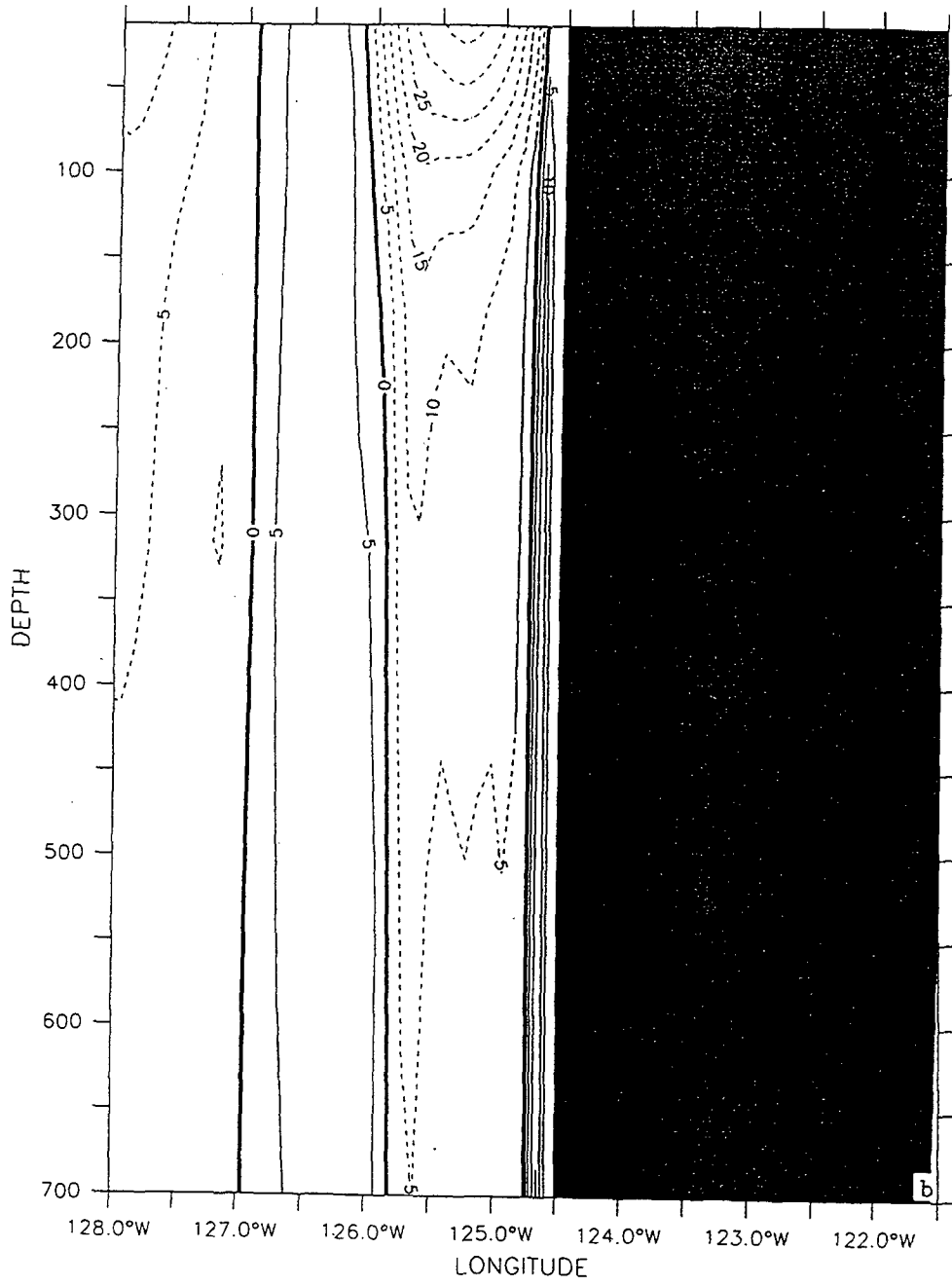


Figure 17. Cross-shore sections for Experiment 3 in the third year of model simulation, time-averaged for days 270-363 at (a) 37°N, (b) 43°N, and (c) 46°N. Contour interval is 5 cm/s.

LATITUDE : 43N



LATITUDE : 46N

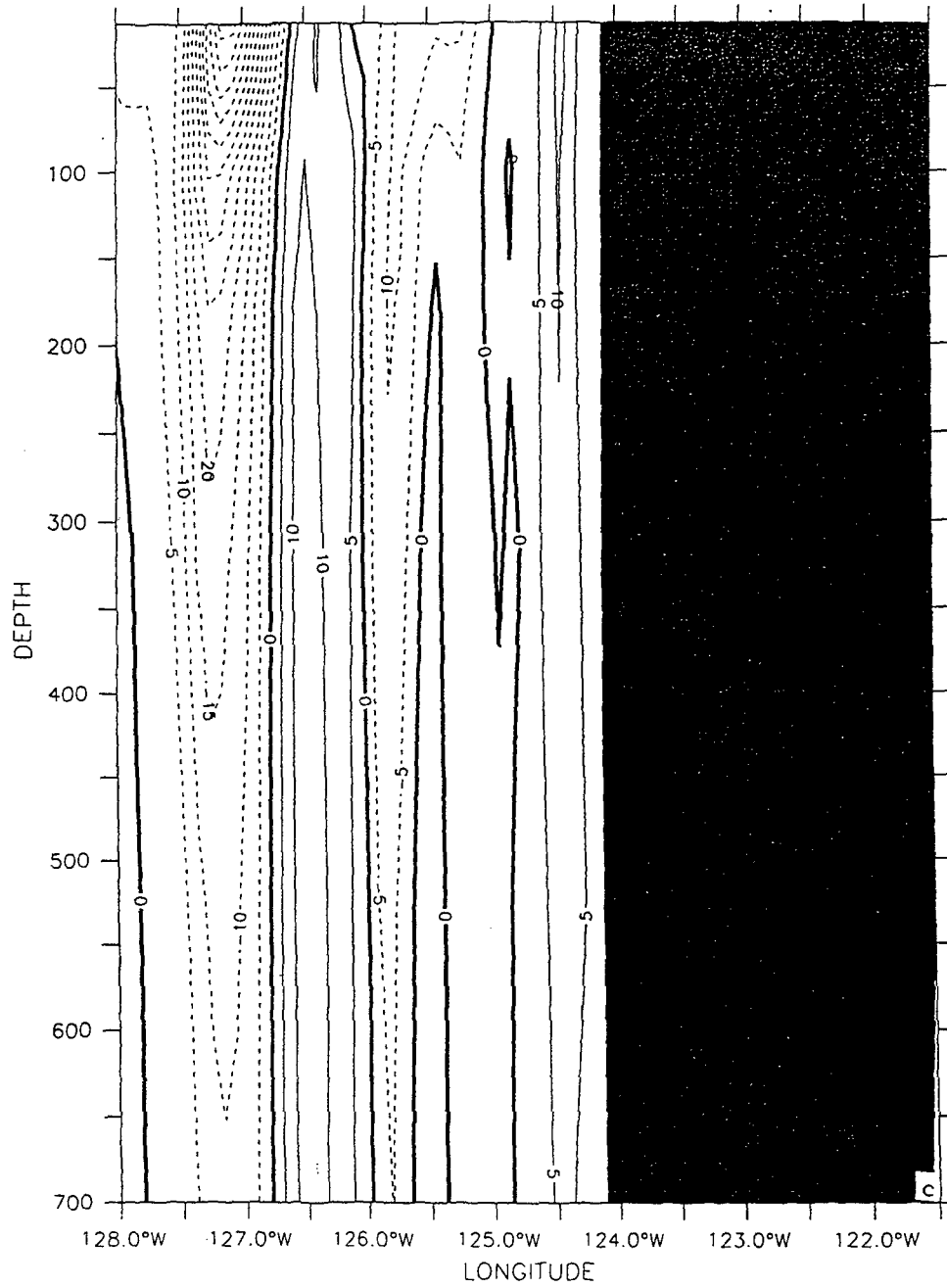


Table 1. Values of Constants Used in the Model

Constant	Value	Definition
T_0	278.2°K	Constant Reference Temperature
S_0	34.7	Constant Reference Salinity
ρ_0	1.0276 gm cm ³	Density of Sea Water At T_0 and S_0
α	$2.4 \times 10^{-4} (\text{°K})^{-1}$	Thermal Expansion Coefficient
β	7.5×10^{-4}	Saline Expansion Coefficient
K	10	Number of Levels In Vertical
Δx	8.0×10^5 cm	Cross-Shore Grid Spacing
Δy	1.1×10^6 cm	Alongshore Grid Spacing
H	4.5×10^5 cm	Total Ocean Depth
Δt	800 s	Time Step
f_0	$0.96 \times 10^4 \text{ s}^{-1}$	Mean Coriolis Parameter
g	980 cm s ²	Acceleration of Gravity
A_M	$2 \times 10^{17} \text{ cm}^4 \text{ s}^{-1}$	Biharmonic Momentum Diffusion Coefficient
A_H	$2 \times 10^{17} \text{ cm}^4 \text{ s}^{-1}$	Biharmonic Heat Diffusion Coefficient
K_M	$0.5 \text{ cm}^2 \text{ s}^{-1}$	Vertical Eddy Viscosity
K_H	$0.5 \text{ cm}^2 \text{ s}^{-1}$	Vertical Eddy Conductivity

LIST OF REFERENCES

- Arakawa, A., and V.R. Lamb, Computational design of the basic dynamical processes of the UCLA general circulation model. In, *Methods in Computational Physics*, J. Chang, ed., Academic Press, 17, 173-265, 1977.
- Batteen, M. L., Model simulations of a coastal jet and undercurrent in the presence of eddies and jets in the California Current System, in *Poleward Flows Along Eastern Ocean Boundaries*, edited by S.J. Neshyba, C.N.K. Mooers, R.L. Smith, and R.T. Barber, pp. 263-279, Springer-Verlag, New York, 1989.
- Batteen, M. L., Wind-forced modeling studies of currents, meanders, and eddies in the California Current System, *J. Geophys. Res.*, 102, 985-1009, 1997.
- Batteen, M. L., C. A. Collins, C. R. Gunderson, and C. S. Nelson, The effects of salinity on density in the California Current System, *J. Geophys. Res.*, 100, 8733-8749, 1995.
- Batteen, M. L., C. L. Butler, and M.-J. Huang, Modeling studies of the Leeuwin Current off Western and Southern Australia, *J. Geophys. Res.*, submitted, 1996.
- Batteen, M.L., and Y.-J. Han, On the Computational noise of finite-difference schemes used in ocean models, *Tellus*, 33, 387-396, 1981.
- Batteen, M.L., R.L. Haney, T.A. Tielking, and P.G. Renaud, A numerical study of wind forcing of eddies and jets in the California Current System, *J. Mar. Res.*, 47, 493-523, 1989.
- Bernstein, R.L., L.C. Breaker, and R. Whitner, California Current eddy formation: Ship, air, and satellite results, *Science*, 195, 353-359, 1977.
- Blumberg, A. F., and G. L. Mellor, A description of a three-dimensional coastal ocean circulation model, in *Three-Dimensional Ocean Models*, 4, Coastal Estuarine Stud., vol. 4, edited by N. Heaps, pp. 1-16, AGU, Washington, D. C., 1987.
- Camerlengo, A.L. and J.J. O'Brien, Open boundary conditions in rotating fluids, *J. Comput. Physics*, 35, 12-35, 1980.
- Chelton, D. B., Seasonal Variability of Alongshore Geostrophic Velocity off Central California, *J. Geophys. Res.*, 89, 3473-3486, 1984.
- Haney, R.L., A numerical study of the response of an idealized ocean to large-scale surface heat and momentum flux, *J. Phys. Oceanogr.*, 4, 145-167, 1974.

- Hickey, B.M., The California Current System-Hypotheses and facts, *Prog. Oceanogr.*, 8, 191-279, 1979.
- Hickey, B.M., Western North America, Tip of Baja California to Vancouver Island, in *The Sea*, John Wiley, New York, 1997.
- Holland, W.R., The role of mesoscale eddies in the general circulation of the ocean - numerical experiments using a wind-driven quasigeostrophic model, *J. Phys. Oceanogr.*, 8, 363-392, 1978.
- Holland, W.R., and M.L. Batteen, The parameterization of subgrid scale heat diffusion in eddy-resolved ocean circulation models, *J. Phys. Oceanogr.*, 16, 200-206, 1986.
- Holland, W.R., D.E. Harrison, and A.J. Semtner Jr., Eddy-resolving numerical models of large-scale ocean circulation, in *Eddies in Marine Science*, edited by A.R. Robinson, pp. 379-403, Springer-Verlag, New York, 1983.
- Huyer, A., Coastal upwelling in the California Current system, *Prog. Oceanogr.*, 12, 259-284, 1983.
- Huyer, A., P. M. Kosro, J. Fleischbein, S. R. Ramp, T. Stanton, L. Washburn, F. P. Chavez, T. J. Cowles, S. D. Pierce, and R. L. Smith, Currents and water masses of the coastal transition zone off northern California, June to August 1988, *J. Geophys. Res.*, 96, 14,809-14,831, 1991.
- Kelly, K.A., R.C. Beardsley, R. Lineburner, K.H. Brink, J.D. Paduan, and T.K. Chereskin, Variability of Near-Surface Eddy Kinetic Energy in the California Current Based on Altimetric Drifter and Moored Current Data, *J. Geophys. Res.*, submitted 1997.
- Levitus, S., R. Burgett, and T. P. Boyer, World ocean atlas 1994, Vol. 3: Salinity, *NOAA Atlas NESDI 3*, 99 pp., U. S. Dept. of Commerce, Washington, D. C., 1994.
- Levitus, S. , and T. P. Boyer, World ocean atlas 1994, Vol. 4: Temperature, *NOAA Atlas NESDI 4*, 117 pp., U. S. Dept. of Commerce, Washington, D. C., 1994.
- Lynn, R.S. and J.J. Simpson, The California Current system: The seasonal variability of its physical characteristics, *J. Geophys. Res.*, 92, 12947-12,966, 1987.
- Strub, P.T. and C. James., The Large-Scale Summer Circulation of the California Current., *Geophys. Res. Ltrs*, 22, 207-210, 1995.
- Strub, P.T., P.M. Kosro, A. Huyer, and CTZ Collaborators, The nature of the cold filaments in the California Current system, *J. Geophys. Res.*, 96, 14,743-14,768, 1991.

Trenberth, K.E., W.G. Large, and J.G. Olson, The mean annual cycle in global ocean wind stress, *J. Phys. Oceanogr.*, 20, 1742-1760, 1990.

Weatherly, G.L., A study of the bottom boundary layer of the Florida Current, *J. Phys. Oceanogr.*, 2, 54-72, 1972.

INITIAL DISTRIBUTION LIST

		No. Copies
1.	Defense Technical Information Center 8725 John J. Kingman Rd., STE 0944 Ft. Belvoir, VA 22060-6218	2
2.	Dudley Knox Library..... Naval Postgraduate School 411 Dyer Rd. Monterey, California 93943-5101	2
3.	Chairman (Code OC/Bf) Department of Oceanography Naval Postgraduate School Monterey, California 93943-5122	1
4.	Chairman (Code MR/Wx)..... Department of Meteorology Naval Postgraduate School Monterey, California 93943-5114	1
5.	Dr. Mary L. Batteen, (Code OC/Bv) Department of Oceanography Naval Postgraduate School Monterey, CA 93943-5122	3
6.	Dr. Richard Lambert..... National Science Foundation 4201 Wilson Boulevard Arlington, VA. 22230	1
7.	Dr. T. Kinder Physical Oceanography Division Office of Naval Research 800 N. Quiney Street Arlington, VA. 22217	1
8.	LCDR Philip W Vance..... Cruiser-Destroyer Group Three Unit 25065 FPO, AP 96601-4702	3